




Universitetet
i Stavanger

Faculty of Science and Technology

MASTER'S THESIS

Study Program/ Specialization: Marine and Offshore Technology	Spring semester, 2020 Open / Restricted access
Writer: Vinicius Serta Fraga	 (Writer's signature)
Faculty supervisor: Prof. Muk Chen Ong Dr. Guang Yin	
Thesis title: Numerical Simulations of Flow Over Bottom-Mounted Structures at High Reynolds Number	
Credits (ECTS): 30	
Key words: turbulent flow, bottom-mounted structures tandem cylinders, partially buried, CFD, RANS, SADDES, OpenFOAM, Proper Orthogonal Decomposition	Pages: 101 + Enclosure: none Stavanger, June 14, 2020 Date/year

Abstract

A common challenge in on-bottom stability design is to select accurate hydrodynamic quantities, such as drag and lift coefficients, to compute the forces on structures subject to fluid flow. The objective of the present study is to perform series of numerical simulations of flow over different bottom-mounted structures at high Reynolds numbers. The effects of the geometries and configurations of the structures on the hydrodynamic quantities and the surrounding flow fields are investigated.

The thesis is divided into six chapters. The first chapter consists of an introduction of the topics to be investigated. In the second chapter, a brief review of theory of flow around bluff bodies, turbulence and boundary layer flow is given. The third chapter contains the main theory of Computational Fluid Dynamics (CFD). Also, a description of the Proper Orthogonal Decomposition (POD) technique, which is used to perform post-processing of the simulation results, is presented. The following two chapters consist of two submitted draft journal papers.

In the study of the first paper, flows over single and two tandem partially buried cylinders at Reynolds number of 1.31×10^4 are investigated using two-dimensional (2D) Reynolds-averaged Navier-Stokes (RANS) simulations. The cylinders are subjected to a boundary layer flow. The effects of different burial ratios of the cylinders into the bottom wall and the spacings between the two tandem cylinders are studied. The RANS simulations are combined with the $k - \omega$ Shear Stress Transport (SST) turbulence model. Due to the bottom-wall, the large-scale vortex shedding behind the cylinders is suppressed, hence, steady simulations are performed. Grid resolution studies are conducted, and the validation studies show that the present results are in agreement with previous published data. It is found that the drag and lift coefficients decrease with the increasing burial ratio of the cylinders. For the two tandem cylinders cases, the hydrodynamic forces of the downstream cylinder are significantly lower compared with those of the upstream cylinder. Also, for each burial ratio considered in the present study, a critical distance between the cylinders is found where the drag forces on the downstream cylinder are zero. It is observed that this critical distance is close to the recirculation length behind a single cylinder with the same burial ratio.

In the study of the second paper, flows over bottom-mounted ribs with square, trapezoidal and rectangular cross-sections are studied. Three-dimensional (3D) Spalart-Allmaras Delayed Detached-Eddy Simulations (SADDES) are performed at the Reynolds number of 1×10^6 . The

structures are exposed to a boundary layer flow. A grid convergence study is conducted, and the results are validated against the published experimental data. It is observed that the hydrodynamic quantities of the trapezoidal rib are lower compared with those of the square and rectangular ribs. The coherent structures of the turbulent flow are studied using POD analysis of the pressure and velocity components obtained on one streamwise plane and two spanwise planes in the wake region behind the ribs. A convergence study based on the number of snapshots and the time step between them is performed. It is found that the energy is highly concentrated in a few low order modes, which can be useful for building reduced order models of the flow. Many of the POD modes appear in pairs, which indicates the convection of the flow structures. The most energetic flow structures of the POD modes tend to appear around the shear layer of the wake flow and the vortical structures shown in the POD modes indicate a strong 3D behaviour of the flow behind the ribs.

At the end, the main conclusions are given together with the recommendations for future works.

Acknowledgements

I would like to express my deepest gratitude to Prof. Muk Chen Ong for the unique supervision and his capacity of managing such brilliant team in the University of Stavanger. The guidance provided by my co-supervisor, Dr. Guang Yin, is memorable and enriched my work in a notorious way. He definitively made this long journey much simpler by uncomplicating all the elements involved in this project.

I would like to thank Per R. Nystrøm, from IKM Ocean Design AS, who proposed the exciting investigation of the flow over tandem cylinders laid on a flat seabed.

As part of Prof. Ong's CFD team, my sincere thanks to the assistance provided by the PhD. Student, Marek Jan Janocha, whose contributions for this work are undeniable.

I wish to acknowledge the resources provided by the Department of Mechanical and Structural Engineering and Materials Science of the University of Stavanger, which were fundamental for the ongoing of this project.

To my beloved wife, Clarissa, who has also been my best colleague in the master's programme and never refused to help or support even in the most challenging moments. Doubtless, this work would never have been accomplished without her company.

I will be always grateful to my family members for leading me to the engineering path. A special mention to my parents and my brother, who gave me an indescribable support during those tough years. Their intangible attitudes are the main reason for such achievement.

Table of Contents

Abstract	i
Acknowledgements	iii
Table of Contents	iv
List of Figures	vi
List of Tables	vi
1. Introduction	1
1.1 Background and Motivation	1
1.2 Problem Definition and Objectives	2
1.3 Structure of the Thesis	2
References	4
2. Theory	5
2.1 Flow Characteristics	5
2.2 Turbulence	6
2.3 Boundary Layer and Flow Separation	7
2.3.1 Boundary Layer	7
2.3.2 Flow Separation	10
2.4 Hydrodynamic Forces	11
References	13
3. Computational Method	14
3.1 Introduction to CFD	14
3.2 OpenFOAM	14
3.3 Governing Equations	15
3.4 Finite Volume Method	16
3.4.1 Spatial Discretization	16
3.4.2 Temporal Discretization	18
3.4.3 SIMPLE and PISO algorithms	18

3.5 Turbulence Models	19
3.5.1 $k - \omega$ SST Turbulence Model	21
3.5.2 Detached-Eddy Simulation	22
3.5.2.1 Spalart-Allmaras Turbulence Model	22
3.5.2.2 Delayed Detached-Eddy Simulation	23
3.6 Proper Orthogonal Decomposition	23
References	25
4. Paper I: Numerical Simulations of Flow Over Single and Two Tandem Cylinders with Different Burial Ratios and Spacings	27
5. Paper II: Three-dimensional Numerical Simulations and Proper Orthogonal Decomposition Analysis of Flow Over Different Bottom-mounted Ribs	53
6. Concluding Remarks	100
6.1 Conclusions	100
6.2 Recommendations for Future Work	101

List of Figures

2.1	Flow regimes	5
2.2	Energy cascade of turbulence	7
2.3	Boundary layer in different flow regimes	8
2.4	Velocity distribution in different sublayers near the wall	9
2.5	Numerical modelling (a) without wall function and (b) with wall function	10
2.6	Velocity profiles around a separation point	11
2.7	Hydrodynamic forces on a bottom-mounted cylinder	12
3.1	Directory structure in OpenFOAM	15
3.2	Control volume	16
3.3	Example of (a) structured and (b) unstructured meshes	17
3.4	Flowchart of (a) SIMPLE and (b) PISO algorithms	19
3.5	Turbulent fluctuation of a quantity ϕ along time	20

List of Tables

3.1	Corresponding constants in SST model	22
-----	--	----

Chapter 1

1. Introduction

1.1 Background and Motivation

Bottom-mounted structures are vastly used for engineering purposes, such as subsea pipelines, subsea covers, heat exchangers and gas turbines. With the depletion of most oil and gas reserves located onshore and close to shore, significant amount of subsea structures and equipment is designed to be installed in offshore locations. A similar trend is observed for the installation and use of devices to generate renewable energy, such as wind turbines and wave energy converters. According to Ong et al. (2010), the structures located on offshore environments can be exposed to high Reynolds number flow of up to $O(10^7)$.

Billions of dollars are spent to install and maintain thousands of kilometres of pipelines every year (Rui et al. 2011). The design of such structures requires good understanding of the forces acting on them and the surrounding flow pattern influenced by the geometry of the structures. For example, subsea pipelines can be found completely or partially buried in the seabed due to their weight, the seabed permeability, installation motion, trenching and burying methods. At different burial depths, pipelines are subjected to different forces due to changes in the exposed geometry to the flow. Hence, to correctly estimate the hydrodynamic coefficients of them, it is necessary to analyze the flow over these structures under different configurations. Moreover, to ensure the safe installation of the subsea structures on the seabed, the prediction of the hydrodynamic quantities is also important.

With the advance of numerical methods and computational power in last decades, the use of Computational Fluid Dynamics (CFD) has significantly increased for research and engineering purposes. Problems that are expensive or unfeasible to be solved using experiments have been performed with the aid of numerical tools, and they also require a good understanding of the physical phenomena. In the present thesis, CFD simulations are used to investigate the flow over different wall-mounted structures. For numerical simulations that generate significant amount of data, advanced post-processing techniques can be used to treat them. Proper Orthogonal Decomposition (POD) is employed in the current work. In fluid mechanics, it was originally proposed by Lumley (1967) and it is a valuable tool to identify the dominant turbulent structures in the flow. Such post-processing technique is also proved to be useful to build reduced order models (Tairal et al. 2017) as the main characteristics of the flow can be extracted from the huge amount of simulation data.

1.2 Problem Definition and Objectives

Numerical simulations are carried out to study the flow over different bottom-mounted structures. The well-known finite volume method (FVM) numerical toolbox Open-source Field Operation And Manipulation (OpenFOAM) is used to resolve the CFD simulations. Two main studies are performed in the present thesis:

- (i) Two-dimensional (2D) Reynolds-averaged Navier-Stokes (RANS) simulations are employed to study the flow over a single and two tandem pipelines laid on a flat seabed with different burial ratios within the seabed and pitch ratios between the two pipelines. The main objective of this study is to analyze the effects of different configurations on the main hydrodynamic quantities, such as drag and lift coefficients and the surrounding flow field.
- (ii) Flows over different bottom-mounted ribs with square, trapezoidal and rectangular cross-sections, are studied using three-dimensional (3D) Spalart-Allmaras Delayed Detached-Eddy Simulations (SADDES). The main objectives are to investigate the hydrodynamic coefficients and the flow structures around the three different ribs. POD analysis is carried out to identify the main flow structures in the wake region.

1.3 Structure of the Thesis

The contents found in the thesis are structured as follows:

- Chapter 2: A concise review of turbulence in fluids, flow around bluff bodies, boundary layer and hydrodynamic forces are given.
- Chapter 3: A review of the theory of CFD is presented. An introduction to CFD is given along with the numerical method tool used in the simulations, (OpenFOAM). Also, the governing equations of the flow, FVM method, turbulence models and the POD technique are discussed.
- Chapter 4: A similar version of the paper that has been sent to Ocean Engineering journal is given. Flows over a single and two tandem pipelines laid on a flat wall with different burial ratios in the seabed and different pitch ratios between the two pipelines are investigated using 2D RANS equations combined with the $k - \omega$ SST turbulence model at a Reynolds number of 1.31×10^4 .
- Chapter 5: It contains a similar version of the paper that has been submitted to Ships and Offshore Structures journal. Flows over ribs with different geometries at a

Reynolds number of 1×10^6 is studied using 3D SADDLES, and POD analysis of the flow structures in the wake flow behind the ribs is performed.

- Chapter 6: Lastly, conclusion remarks of both studies and recommendations for future work are given.

References

Lumley, J. L. (1967). The Structure of Inhomogeneous Turbulent Flows. Atmospheric turbulence and radio wave propagation.

Ong, M. C., Utnes, T., Holmedal, L. E., Myrhaug, D., & Pettersen, B. (2010). Numerical simulation of flow around a circular cylinder close to a flat seabed at high Reynolds numbers using a k- ϵ model. *Coastal Engineering*, 57(10), 931-947.

Rui, Z., Metz, P., Reynolds, D., Chen, G., & Zhou, X. (2011). Historical pipeline construction cost analysis. *Int. J. of Oil*. 4. 244 - 263. 10.1504/IJOGCT.2011.040838.

Taira, K., Brunton, S. L., Dawson, S. T., Rowley, C. W., Colonius, T., McKeon, B. J., ... & Ukeiley, L. S. (2017). Modal analysis of fluid flows: An overview. *Aiaa Journal*, 4013-4041.

Chapter 2

2. Theory

2.1 Flow Characteristics

One major quantity of any flow is defined by the dimensionless ratio of inertial and viscous forces. It characterizes the flow pattern in different scales of regimes, here summarized as laminar, transitional and turbulent flows (Fig. 2.1). The Reynolds number can be defined as:

$$Re = \frac{U_{\infty}L}{\nu} \quad (2.1)$$

where U_{∞} denotes the free stream velocity, L is the characteristic length of the structure and the kinematic viscosity is given by ν .

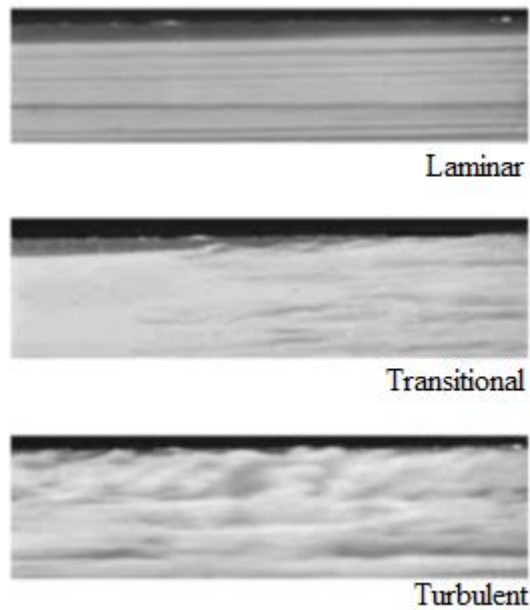


Figure 2.1: Flow regimes (Çengel and Cimbala, 2010, p. 11)

Flow over wall-mounted structures or obstacles very close to the bottom-wall does not experience periodic vortex shedding as observed by Sumer and Fredsøe (2006) and it has a large recirculation motion behind the structure. As a result, this type of flow is much less time dependent compared with the flow around structures far from the wall. According to Castro (1984) and Adams & Johnston (1988), besides the Reynolds number, the main parameters that

influence the flow without vortex shedding are the boundary layer thickness and profile, geometry of the obstacle and the turbulence intensity in the free stream.

2.2 Turbulence

An exact definition of turbulence in fluids is not obvious to formulate. According to Tennekes & Lumley (1972), Pope (2000), Versteeg & Malalasekera (2007) and Lesieur (2008), the main characteristics of turbulent flows can be listed as follows:

- There is an effective transport and mixing of quantities, which is caused by the diffusivity characteristic of turbulence. As a result, there is a high rate of mass, heat and momentum transfer in turbulent flows.
- The flow is characterized by high Reynolds numbers. As the Reynolds number increases, the laminar flow undergoes transitional to turbulent.
- The flow is irregular and unpredictable. Thus, the randomness and chaotic characteristics of turbulent flow demand statistical approaches to simulate it.
- The flow is significantly rotational. Turbulence is highly related to fluctuations of vorticity, which appear due to the no-slip condition on obstacles and boundaries.
- The turbulent flow is essentially 3D. This property is mainly due to the associated randomness of the turbulent fluctuations. 2D approximation of the turbulent flow is usually restricted to cases where 3D effects are low or negligible.
- Turbulent eddies have different length scales. Large eddies tend to be dictated by inertia effects obtained from the mean flow and have their energy transferred through a cascade process to smaller eddies, which tends to be increasingly influenced by viscous effects (Fig. 2.2). Thus, the turbulent flow is substantially dissipative. There is a fast decay in small-scale eddies due to kinetic energy consumption to compensate the viscous losses, resulting in increased energy losses.
- Turbulence is a property of the fluid flow and not of the fluid itself. The main properties of fluid flow are not restrained by the properties of the fluid. Also, turbulent flows can be characterized as a continuum phenomenon, where the smallest eddies are significantly larger compared with molecular scale.

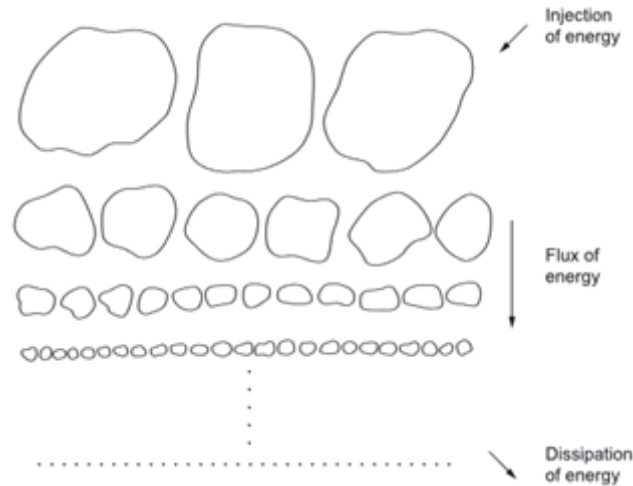


Figure 2.2: Energy cascade of turbulence (Ecke, 2005)

The problems studied in the present thesis assume that the fluid is Newtonian. Thus, the shear stress (τ) varies linearly with the dynamic viscosity (μ) and when the shear rate is zero, the resultant shear stress is also zero. This assumption can be made since the Mach number (M) is lower than 0.3. The shear stress and the Mach number can be expressed as:

$$\tau = \mu \frac{du}{dy} \quad (2.2)$$

$$M = \frac{U_{\infty}}{c} \quad (2.3)$$

where c represents the speed of sound in a given medium.

2.3 Boundary Layer and Flow Separation

2.3.1 Boundary Layer

The viscosity of a fluid implies that when it is in contact with a solid surface, the velocities on the wall are zero, which is termed as “no-slip condition”. The region of the flow directly affected by the surface can be defined as boundary layer and was first described by Prandtl (1904). Also, the boundary layer thickness (δ) corresponds to the region where the horizontal velocity is up to 99% of the free stream velocity. The boundary layer in different flow regimes is illustrated in Fig. 2.3.

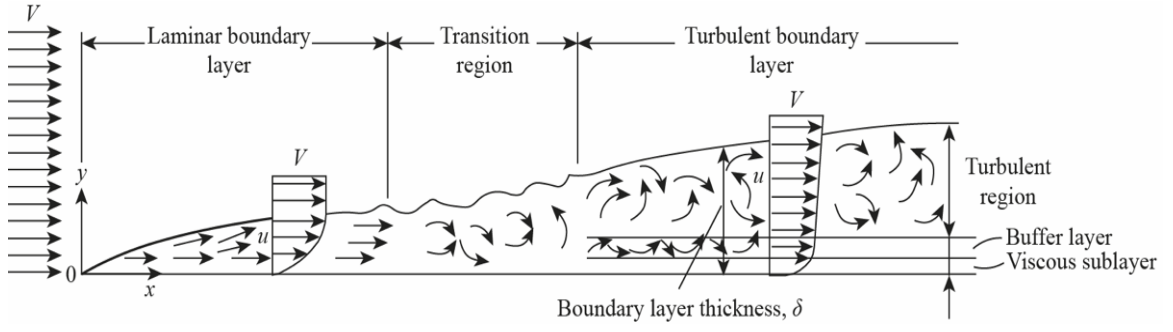


Figure 2.3: Boundary layer in different flow regimes (Çengel and Cimbala, 2006, p.579)

Many authors have developed the boundary layer theory, such as Tennekes & Lumley (1972), Pope (2000), White (2006), Çengel & Cimbala (2006), Versteeg & Malalasekera (2007), Lesieur (2008) and Kundu et al. (2012). The governing equations of a steady 2D laminar boundary layer can be expressed as:

$$\frac{\partial u}{\partial x} + \frac{\partial v}{\partial y} = 0 \quad (2.4)$$

$$u \frac{\partial u}{\partial x} + v \frac{\partial u}{\partial y} = U_{\infty} \frac{dU_{\infty}}{dx} + \nu \frac{\partial^2 u}{\partial y^2} \quad (2.5)$$

where u and v are the horizontal and vertical velocity components, respectively.

Far from the wall boundary, the velocity components tend to be much higher than near the wall, resulting in the dominance of inertia forces. On the other hand, in regions very close to the wall, characterized by very low velocities due to the no-slip condition, viscous forces are at least in the same magnitude of inertial forces and potential flow theory cannot be applied. The shear stress (Eq. 2.2) on the bottom wall is given by:

$$\tau_w = \rho \nu \left(\frac{\partial u}{\partial y} \right)_{y=0} \quad (2.6)$$

where ρ denotes the fluid density. The dimensionless wall distance (y^+) and the dimensionless velocity (U^+) can be defined as:

$$y^+ = \frac{u_{\tau} \Delta y}{\nu} \quad (2.7)$$

$$U^+ = \frac{U}{u_{\tau}} \quad (2.8)$$

where Δy is the distance of the first element perpendicular to the wall and the friction velocity (u_τ) is given by:

$$u_\tau = \sqrt{\frac{\tau_w}{\rho}} \quad (2.9)$$

The inner region of the wall layer is known as viscous sublayer, corresponding to the region of $y^+ \leq 5$, where the velocity profile can be expressed by only near-wall parameters. In turbulent flows over smooth surfaces, there is a linear velocity distribution, which can be expressed by:

$$U^+ = y^+ \quad (2.10)$$

For the outer region, of y^+ between 5 and 30, known as buffer layer, the main characteristics of the turbulent flow start to get similar to those in the free stream region, which is inviscid. Also, above the buffer layer, the velocity can be described by the logarithmic law given by:

$$U^+ = \frac{1}{\kappa} \ln(y^+) + C^+ \quad (2.11)$$

where κ represents the von Kármán constant, in general equal to 0.41, and the constant $C^+ = 5.1$. The velocity in the region of $y^+ = O(10^2)$ can be well described by Eq. 2.11. The velocity distribution of a turbulent flow near a flat wall is presented in Fig. 2.4.

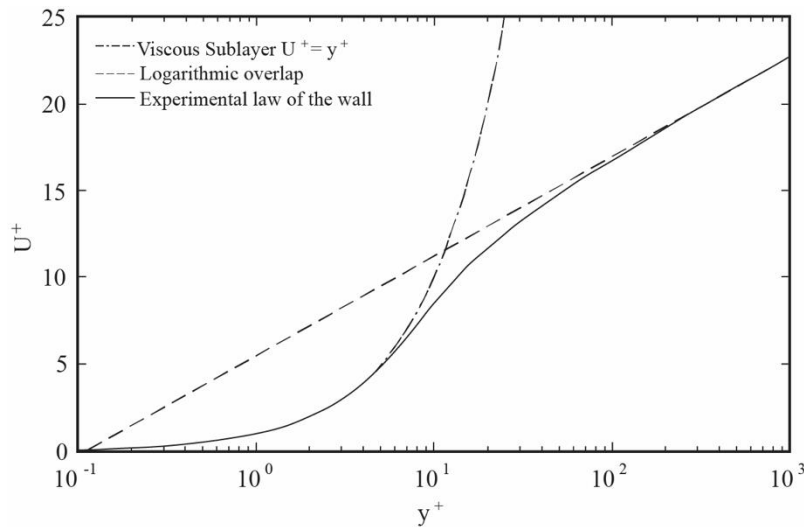


Figure 2.4: Velocity distribution in different sublayers near the wall

In the numerical modelling of high Reynolds flows, it is common to use wall functions to avoid resolving the flow in the viscous sublayer region. Some turbulence models, such as $k - \varepsilon$, do

not perform well close to the wall. Also, a y^+ of $O(1)$ for the first grid point off the wall is necessary, which can be computationally expensive. The use of wall functions is possible due to the low contribution of the viscous sublayer region to the entire flow compared with the rest of the boundary layer and it is also useful to avoid excessive refinement close to the walls. In this case, for a log-law layer, a minimum of $y^+ \approx 30$ has to be satisfied to ensure that the first nodes are in the region where the logarithmic wall function is accurate. An example of modelling without wall function and with wall function is presented in Fig. 2.5.

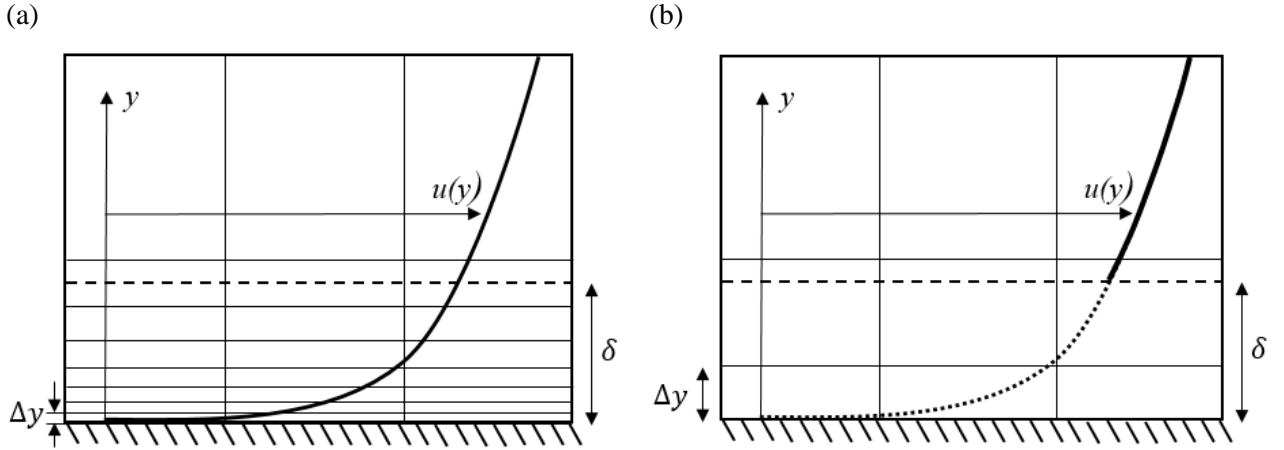


Figure 2.5: Numerical modelling (a) without wall function and (b) with wall function

2.3.2 Flow Separation

Due to a strong adverse pressure gradient, separation of the boundary layer from bluff bodies surfaces may occur. As a result, the velocities along the boundary layer start to decrease, the boundary layer thickness is increased, and the flow starts to reverse. Thus, the boundary layer can no longer continue attached to the wall and there is a local stagnation point, known as separation point, where:

$$u \frac{du}{dx} = -\frac{1}{\rho} \frac{dp}{dx} \quad (2.12)$$

$$\left(\frac{du}{dy}\right)_s = 0 \quad (2.13)$$

According to Eq. (2.12), when the pressure increases, there is an adverse pressure gradient. Also, in the separation point, the shear stress on the wall is zero (Eq. 2.13). In the region where separation occurs and downstream the separation point, it is not possible to apply the boundary layer approximation, as its properties are lost. An example of flow separation on a curved surface is given in Fig. 2.6. The flow separation is strongly dependent on the flow

characteristics and the geometry of the structure. Regarding the shape of a structure in the flow direction, the flow separation over blunt bodies tend to occur easier than over streamlined geometries.

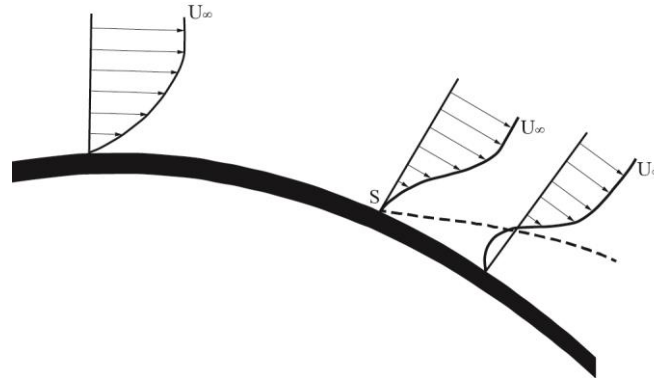


Figure 2.6: Velocity profiles around a separation point (Kundu, 2012, p.386)

2.4 Hydrodynamic Forces

When a body is immersed in fluid flow, there is a force exerted by the flow on it. This force is due to the pressure and friction components of the flow on the surfaces of the structure. The force acting along the flow direction is known as the drag force (F_D) and can be defined as:

$$F_D = \int_A (\bar{p} \cos(\theta_n) + \bar{\tau}_w \sin(\theta_n)) dA \quad (2.14)$$

where the differential area is given by dA and θ_n denotes the angle between the normal unity vector to the surface and the flow direction. The force acting perpendicular to the flow direction is known as the lift force (F_L) and is given by:

$$F_L = - \int_A (\bar{p} \sin(\theta_n) + \bar{\tau}_w \cos(\theta_n)) dA \quad (2.15)$$

Based on the expressions for the hydrodynamic forces (Eq. 2.14 and 2.15), the drag and lift coefficients can be defined as:

$$C_D = \frac{F_D}{\frac{1}{2} \rho U_\infty^2 A} \quad (2.16)$$

$$C_L = \frac{F_L}{\frac{1}{2} \rho U_\infty^2 A} \quad (2.17)$$

where the projected area normal to the flow is denoted by A . The use of coefficients is suitable to analyze flows under similar conditions, such as geometry and Reynolds number, and compute

the forces acting on the structure. The lift and drag forces on a wall-mounted cylinder are displayed in Fig. 2.7.

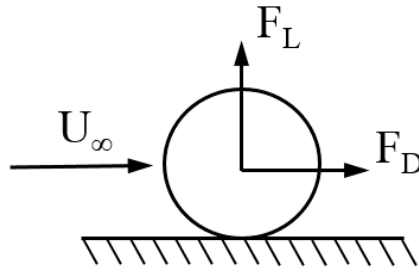


Figure 2.7: Hydrodynamic forces on a bottom-mounted cylinder

References

Çengel, Y. A. & Cimbala, J. M. (2010). *Fluid Mechanics: Fundamentals and Applications*. McGraw-Hill Higher Education.

Ecke, R. (2005). *The Turbulence Problem: An Experimentalist's Perspective*. Los Alamos Science.

Kundu, P. K., Cohen, I. M. & Dowling, D. R. (2012). *Fluid Mechanics*. Elsevier.

Lesieur, M. (2008). *Turbulence in Fluids*. Springer.

Pope, S. B. (2000). *Turbulent Flows*. Cambridge University Press.

Sumer, B. M. & Fredsøe, J. (2006). *Hydrodynamics around Cylindrical Structures*. World Scientific.

Tennekes, H. & Lumley, J. L. (1972). *A First Course in Turbulence*. The MIT Press

Versteeg, H. K. & Malalasekera, W. (2007). *An Introduction to Computational Fluid Dynamics: The Finite Volume Method*. Pearson Education.

Chapter 3

3. Computational Method

3.1 Introduction to CFD

In the past decades, the use of CFD tools has been increased due to decreasing required computational time of simulations. Hence, problems which cannot be solved through empirical or analytical approaches can be solved by using numerical simulations. Numerical investigations of fluid flow, heat transfer and many other phenomena can be carried out for research and industrial purposes with satisfactory results. In the present thesis, the OpenFOAM code is employed to perform the numerical simulations.

The codes employed for CFD simulations have in general three main steps (Versteeg & Malalasekera, 2007):

- Pre-processing: it involves all the necessary inputs for the simulations such as the computational domain and grid (or mesh) of cells (or elements), also known as control volumes. Physical phenomena, fluid properties and boundary conditions are also set.
- Solving: FVM is employed for the integration of the control volume and discretization of equations.
- Post-processing: it consists of the numerical and graphical analysis of the results.

3.2 OpenFOAM

The present simulations are carried out using the software OpenFOAM v2.4. It is an open source CFD code with a customized C++ engine. Different from commercial tools, it does not have a graphical user interface (GUI) and all the flow parameters are written in text files, while tasks are performed by commands in the terminal. A typical structure of the case directory is given in Fig. 3.1.

Where the case directory contains three major folders:

- *Constant*: it contains the physical properties of the flow. The value for the kinematic viscosity is given in the *transportProperties*, and in the *turbulenceProperties*, the turbulence model used in the simulation is defined. Also, the grid and its boundary conditions are located in the subdirectory *polyMesh*.

- *System*: it is used to specify the solution procedure and all its parameters. There are three main subdirectories: *controlDict*, used to set control parameters such as time step and simulation time. It also contains additional inputs to generate non-standard data; the employed discretization schemes are located in the subdirectory *fvSchemes*; and the numerical solvers are found in the *fvSolution* subdirectory as well as algorithm controls and residual tolerances.
- *Time directory*: it contains the initial and boundary conditions that define the problem. It can also contain the resolved flow at a specific simulation time.

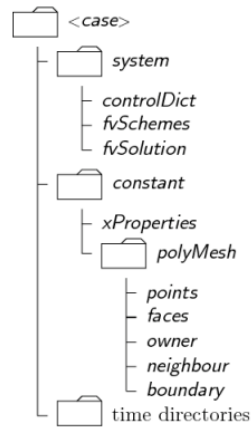


Figure 3.1: Directory structure in OpenFOAM (OpenFOAM-UserGuide, 2015 p. U-108)

3.3 Governing Equations

Based on the continuum hypothesis, a numerical description of the fluid flow is given by the Navier-Stokes equation. The continuity equation of an incompressible fluid can be written as:

$$\frac{\partial u_i}{\partial x_i} = 0 \quad (3.1)$$

When Newton's Second Law is applied to an infinitesimal volume, given by a fluid particle, the momentum equation of an incompressible fluid can be given by:

$$\frac{\partial u_i}{\partial t} + u_j \frac{\partial u_i}{\partial x_j} = -\frac{1}{\rho} \frac{\partial p}{\partial x_i} + \nu \frac{\partial^2 u_i}{\partial x_j^2} \quad (3.2)$$

where $i, j = 1, 2, 3$ denote the streamwise, cross-stream and spanwise directions, respectively. And $(u_1, u_2, u_3) = (u, v, w)$, which are their corresponding velocity components.

3.4 Finite Volume Method

There are many numerical methods that can be applied to solve Eq. (3.1) and Eq. (3.2) such as Finite Element Method (FEM), Finite Difference Method (FDM) and FVM. However, due to its conservative nature, FVM is considered more efficient for CFD simulations. The discretization of differential equations in a system of algebraic equations is the key of FMV. In a spatial discretization, the grid is subdivided in a collection of control volumes, given by the cells in the mesh topology. Moreover, in unsteady problems the time domain is divided in time steps based on the temporal discretization. The integral form of the conservation equation can be expressed as:

$$\frac{\partial}{\partial t} \iiint_V \phi dV + \iint_S \vec{f} d\vec{S} = \iiint_V V_V dV + \iint_S V_S dS \quad (3.3)$$

where an unknown quantity, such as mass or a velocity component, is given by ϕ . The control volume is denoted as V , the control surface is given by S , V_V and V_S are sources of ϕ in the control volume and on the control surface, respectively. Also, \vec{f} denotes the flux of the quantity ϕ .

3.4.1 Spatial Discretization

A spatial discretization is necessary to obtain the solution in each mesh element. An example of the control volume is illustrated in Fig. 3.2. It is a polyhedral element where the flow is solved. A general space discretization can be given as:

$$\int_{V_c} (x - x_c) dV = 0 \quad (3.4)$$

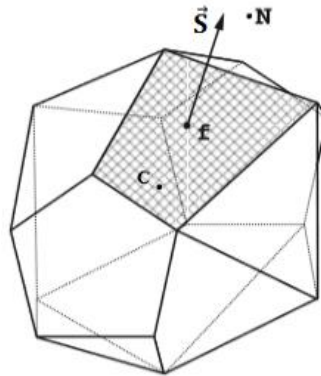


Figure 3.2: Control volume (Jasak, 1996)

where V_C is the volume of a specific element and the centroid of the volume is C , where the calculations are performed. Also, the centroid of a neighbouring element is denoted as N and \vec{S} represents the surface vector.

The type of grid and how it is built has a significant impact on the simulation time and results. Both are influenced by the type and skewness of the elements, cell progression, non-orthogonality, aspect ratio and density of the grid. The grids can have two types of elements, structured or unstructured (Fig. 3.3).

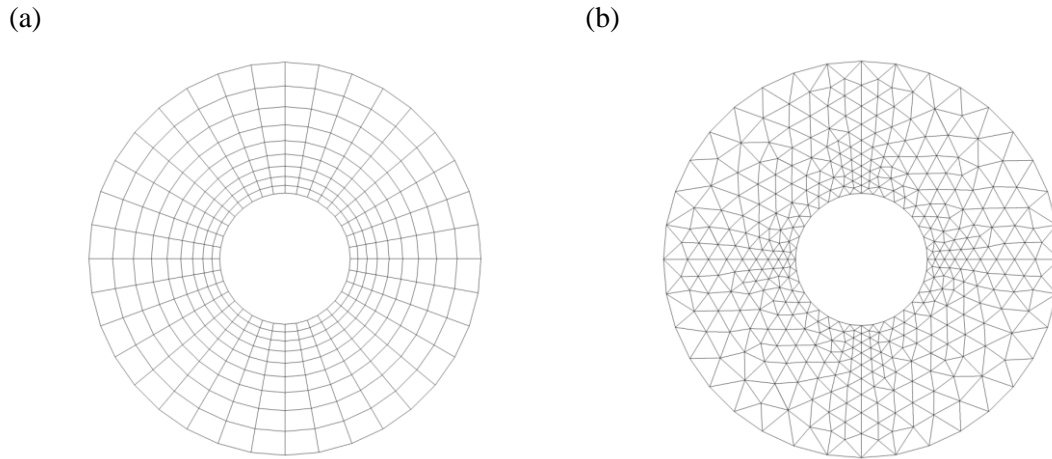


Figure 3.3: Example of (a) structured and (b) unstructured meshes

2D and 3D structured meshes consist of quadrilateral and hexahedra elements, respectively, which are orthogonal in space. In general, they give converged results with less elements. When the number of neighbouring nodes is not fixed in a control volume and the mesh has irregular connectivity, the grid elements are unstructured. They are used in geometries with high complexity and are typically given by triangles and tetrahedral elements in 2D and 3D grids, respectively.

In order to compute the flow quantities in each cell, interpolation methods are used. In the present simulations, the scheme applied for interpolation is linear. It can be written as:

$$\phi_f = f_x \phi_C + (1 - f_x) \phi_N \quad (3.5)$$

$$f_x = \frac{|x_f - x_N|}{|x_f - x_N| + |x_f - x_C|} \quad (3.6)$$

where f_x represents the linear interpolation factor.

3.4.2 Temporal Discretization

Similarly to spatial discretization, the time must also be discretized. There are many schemes for temporal discretization, such as backward, Euler implicit and Crank-Nicolson time schemes. In the present thesis, second order Crank-Nicolson method is employed to resolve the transient problem given in Chapter 5. This method implies that any quantity ϕ integrated in time is given by:

$$\phi^{n+1} = \phi^n + \frac{\Delta t}{2} [f(t^n, \phi^n) + f(t^{n+1}, \phi^{n+1})] \quad (3.7)$$

where the fixed time step is denoted as Δt .

In order to maintain stability during the simulations, the given scheme needs to satisfy Courant number (Co) lower than one. The dimensionless number measures the amount of information that is traversed through an element of the grid and it is expressed as:

$$Co = \frac{U\Delta t}{\Delta x} \quad (3.8)$$

where U and Δx represent the velocity at a specific element and the element size, respectively. If Co is higher than one in an element, it means that for a given time step, the information will not be properly computed in that cell, which may result in an unstable solution.

3.4.3 SIMPLE and PISO Algorithms

In the current thesis, steady state and transient problems are investigated. The equations for pressure and velocity are solved iteratively. The algorithm used to solve the steady state problem in Chapter 4 is the Semi-Implicit Method for Pressure-Linked Equations (SIMPLE). The transient analyses in Chapter 5 are solved with the Pressure-Implicit Split-Operator (PISO). SIMPLE algorithm employs only one correction of the initial solutions, while PISO algorithm generally correct them one to four times (OpenFOAM-UserGuide, 2015). In the present study, two corrections are carried out in the PISO algorithm. The flowcharts of both algorithms are given in Fig. 3.4.

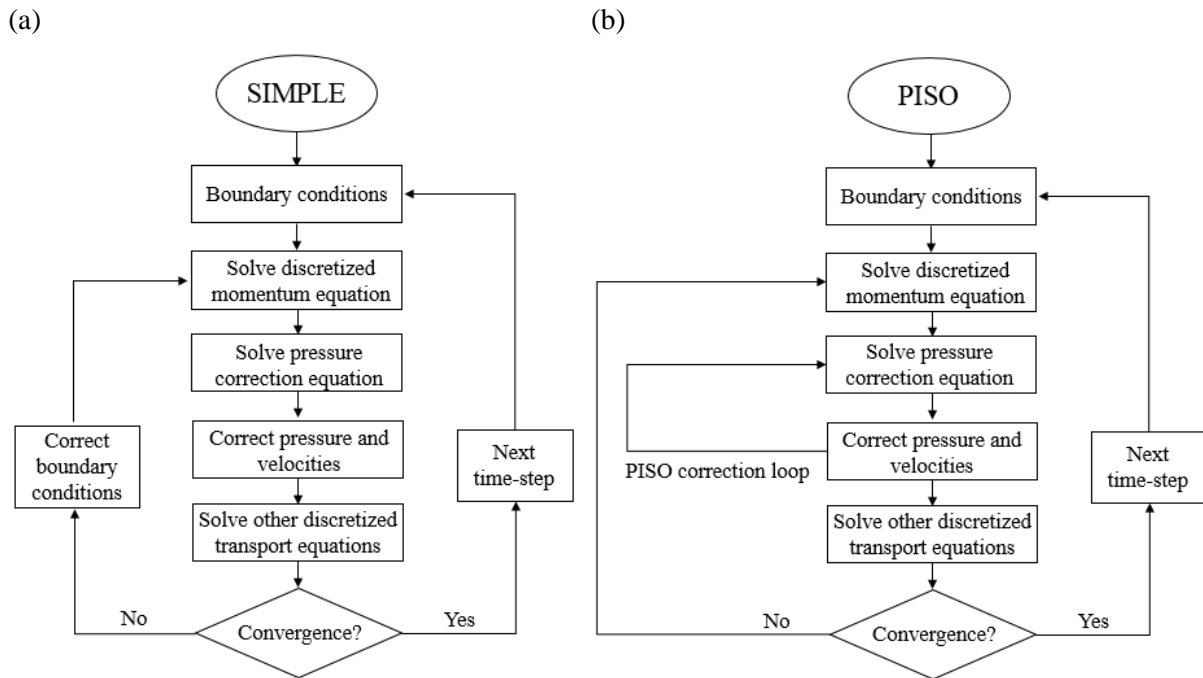


Figure 3.4: Flowchart of (a) SIMPLE and (b) PISO algorithms

where SIMPLE and PISO solvers are employed in OpenFOAM via terminal by the commands *simpleFOAM* and *pisoFOAM*, respectively.

3.5 Turbulence Models

There are mainly three methods to simulate turbulent flows. The first one is Direct Numerical Simulation (DNS) where the full Navier-Stokes equations are solved, and no turbulence model is used. In this case, even the smallest turbulent eddies are resolved, which demands a very fine grid and very small time steps, resulting in a very high computational cost. The second approach is Large Eddy Simulation (LES) where only the large-scale turbulent fluctuations of the flow are resolved. It still demands a fine grid and high computational cost, but it is considerably less demanding compared with DNS. The third is the Reynolds-Averaged Navier-Stokes (RANS) approach where only the time-averaged flow quantities, such as velocity and pressure, are resolved (Fig. 3.5). It demands considerably less computational time compared with DNS and LES. The instantaneous flow quantities ϕ in a specific time can be defined as:

$$\phi = \bar{\phi} + \phi' \quad (3.9)$$

where the mean value is given by $\bar{\phi}$ and the fluctuation part is denoted by ϕ' .

From integration of the continuity (Eq. 3.1) and the momentum (Eq. 3.2) equations, the mean of the fluctuations is $\overline{\phi'} = 0$. Thus, the RANS equations of conservation of mass and momentum can be expressed as:

$$\frac{\partial \bar{u}_i}{\partial x_i} = 0 \quad (3.10)$$

$$\frac{\partial \bar{u}_i}{\partial t} + \bar{u}_j \frac{\partial \bar{u}_i}{\partial x_j} = -\frac{1}{\rho} \left(\frac{\partial P}{\partial x_i} \right) + \nu \frac{\partial^2 \bar{u}_i}{\partial x_j^2} - \frac{\partial \overline{u'_i u'_j}}{\partial x_j} \quad (3.11)$$

where $i, j = 1, 2$ denote the streamwise and the cross-stream directions, respectively. u_1 and u_2 are their corresponding resolved velocity components, also denoted by u and v , respectively. The Reynolds stress component is given by $\overline{u'_i u'_j}$, where u'_i is the fluctuation part of the velocities. In steady RANS simulations, the term $\frac{\partial \bar{u}_i}{\partial t}$ is neglected.

According to the Boussinesq approximation, the Reynolds stress components can be expressed as:

$$-\overline{u'_i u'_j} = \nu_t \left(\frac{\partial \bar{u}_i}{\partial x_j} + \frac{\partial \bar{u}_j}{\partial x_i} \right) - \frac{2}{3} k \delta_{ij} \quad (3.12)$$

where ν_t is the turbulent viscosity, the turbulent kinetic energy is given by k and the Kronecker delta is denoted by δ_{ij} . In order to solve the given system of equations, the $k - \omega$ SST turbulence model is employed.

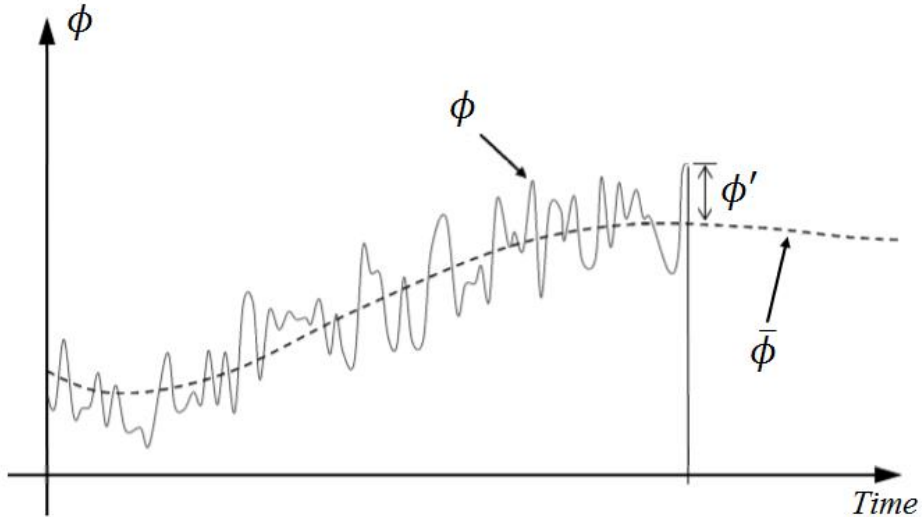


Figure 3.5: Turbulent fluctuation of a quantity ϕ along time

3.5.1 $k - \omega$ SST Turbulence Model

The $k - \omega$ SST turbulence model (Menter, 1994 and Menter et al. 2003) is a hybrid of the classic $k - \varepsilon$ (Jones & Launder, 1973) model and the original $k - \omega$ (Wilcox, 1998) model. The $k - \varepsilon$ model is applied in the region away from the wall, in the free-stream flow. On the other hand, the $k - \omega$ model is used in the near-wall region. The equations for k and ω are given as:

$$\frac{D(\rho k)}{Dt} = \widetilde{P}_k - \beta^* \rho k \omega + \frac{\partial}{\partial x_i} \left[(\mu + \sigma_k \mu_t) \frac{\partial k}{\partial x_i} \right] \quad (3.13)$$

$$\frac{D(\rho \omega)}{Dt} = \alpha \rho S^2 - \beta \rho \omega^2 + \frac{\partial}{\partial x_i} \left[(\mu + \sigma_\omega \mu_t) \frac{\partial \omega}{\partial x_i} \right] + 2(1 - F_1) \rho \sigma_{\omega 2} \frac{\partial k}{\partial x_i} \frac{\partial \omega}{\partial x_i} \quad (3.14)$$

$$\widetilde{P}_k = \min \left[\mu_t \frac{\partial u_i}{\partial x_j} \left(\frac{\partial u_i}{\partial x_j} + \frac{\partial u_j}{\partial x_i} \right), 10 \beta^* \rho k \omega \right] \quad (3.15)$$

The constant φ_i , where $i = 1, 2$, is applied for the $k - \omega$ model and the $k - \varepsilon$ model constants, respectively. The switch between the two models is given by the blending functions F_1 and F_2 . The constant φ in the SST model can be described as:

$$\varphi = F_1 \varphi_1 + (1 - F_1) \varphi_2 \quad (3.16)$$

$$F_1 = \tanh \left\{ \left(\min \left[\max \left(\frac{\sqrt{k}}{\beta^* \omega y}, \frac{500\nu}{y^2 \omega} \right), \frac{4\rho \sigma_{\omega 2} k}{CD_{k\omega} y^2} \right] \right)^4 \right\} \quad (3.17)$$

$$CD_{k\omega} = \max \left(2\rho \sigma_{\omega 2} \frac{1}{\omega} \frac{\partial k}{\partial x_i} \frac{\partial \omega}{\partial x_i}, 10^{-10} \right) \quad (3.18)$$

where the distance to the closest wall is given by y and the positive part of the cross-diffusion term in Eq. (3.13) is expressed by $CD_{k\omega}$. The turbulent viscosity (ν_t) can be written as:

$$\nu_t = \frac{a_1 k}{\max(a_1 \omega, S F_2)} \quad (3.19)$$

$$F_2 = \tanh \left[\left[\max \left(2 \frac{\sqrt{k}}{\beta^* \omega y}, \frac{500\nu}{y^2 \omega} \right) \right]^2 \right] \quad (3.20)$$

where the constant $a_1 = 0.31$, the invariant measure of the strain rate is denoted by S and the corresponding constants employed in the SST model are presented in Table 3.1.

Table 3.1: Corresponding constants in SST model

φ	β^*	β	σ_k	σ_ω	α
φ_1	0.09	0.075	0.85	0.5	0.555
φ_2	0.09	0.083	1	0.856	0.44

3.5.2 Detached-Eddy Simulation

Detached-Eddy Simulation (DES) method is a hybrid of RANS and LES approaches. RANS model is applied in boundary layers, while LES treatment is applied far from the walls. DES is a valuable method to avoid very high refinement in the near wall region at high Reynolds flows. Here, both RANS and LES are resolved with the Spalart-Allmaras turbulence model.

3.5.2.1 Spalart-Allmaras Turbulence Model

Originally developed by Spalart & Allmaras (1994), the Spalart-Allmaras turbulence model only uses one equation to solve the Reynolds stresses in RANS approach. Thus, the Reynolds stress component can be written as:

$$-\overline{u'_i u'_j} = \nu_t \left(\frac{\partial \bar{u}_i}{\partial x_j} + \frac{\partial \bar{u}_j}{\partial x_i} \right) \quad (3.21)$$

The one equation Spalart-Allmaras model solves the transport equation for the turbulent eddy viscosity (ν_t) and it is defined by:

$$\nu_t = \tilde{\nu} f_{v1} \quad f_{v1} = \frac{X^3}{X^3 + C_{v1}^3} \quad X = \frac{\tilde{\nu}}{\nu_t} \quad (3.22)$$

where the subscript v represents “viscous”, the modified turbulent viscosity is denoted by $\tilde{\nu}$ and the constant $C_{v1} = 7.1$.

In OpenFOAM, it is used the f_{v3} -implementation (Rumsey et al. 2001) of the Spalart-Allmaras model, which is indicated to solve fully turbulent flows. The variable \tilde{S} and the empirical function f_{v2} are given as:

$$\tilde{S} = f_{v3} S + \frac{\tilde{\nu} f_{v2}}{\kappa^2 d^2} \quad (3.23)$$

$$f_{v2} = \frac{1}{\left(1 + \frac{X}{C_{v2}}\right)^3} \quad (3.24)$$

where S is the measure of the deformation tensor, the minimum distance from the closest wall is given by d , $C_{v2} = 5$ and the additional term (f_{v3}) is:

$$f_{v3} = \frac{(1 + Xf_{v1})(1 - f_{v2})}{X} \quad (3.25)$$

To determine whether RANS or LES is applied, the length scale \tilde{d} is employed:

$$\tilde{d} = \min(d, C_{DES}\Delta) \quad (3.26)$$

where the calibration constant $C_{DES} = 0.65$ and the measure of grid spacing is denoted as Δ :

$$\Delta = \max(\Delta_x, \Delta_y, \Delta_z) \quad (3.27)$$

where $\Delta_x, \Delta_y, \Delta_z$ represent the measure of the grid cell in a 3D coordinate system.

3.5.2.2 Delayed Detached-Eddy Simulation

If there is any undesirable change of RANS to LES within the boundary layer, modelled-stress depletion (MSD) may occur, which can lead to grid-induced separation (Spalart et al. 2006). An updated version of DES, Delayed Detached-Eddy Simulation (DDES), uses a new length scale \tilde{d}_d to prevent MSD, avoiding RANS to switch to LES prematurely. In the present thesis, SADDES turbulence model is employed in Chapter 5 and \tilde{d}_d is given by:

$$\tilde{d}_d = d - f_d \max(0, d - C_{DES}\Delta) \quad (3.28)$$

$$f_d = 1 - \tanh([8r_d]^3) \quad (3.29)$$

$$r_d = \frac{(v_t + \nu)}{(\tilde{S}\kappa^2 d^2)} \quad (3.30)$$

where f_d and r_d are modified parameters in DDES formulation.

3.6 Proper Orthogonal Decomposition

Originally proposed by Lumley (1967) in fluid dynamics, POD is employed as a post-processing technique to analyze the dominant turbulent structures of the 3D flow in the problem investigated in Chapter 5. It is a strong statistical method of data driven to find interdependencies within the data. Hence, it is possible to describe large amount of data with a

lower order approximation and the technique can be also useful to control the flow, and for design purposes (Samani, 2014).

This statistical method can be applied to any scalar or vector quantities, such as pressure and velocities. A time-dependent flow variable $\mathbf{q}(\boldsymbol{\chi}, t)$ can be decomposed into a series of spatial modes $\boldsymbol{\phi}_j(\boldsymbol{\chi})$ and their corresponding temporal coefficients $a_j(t)$:

$$\mathbf{q}(\boldsymbol{\chi}, t) = \sum_j a_j(t) \boldsymbol{\phi}_j(\boldsymbol{\chi}) \quad (3.31)$$

where the POD modes $\boldsymbol{\phi}_j(\boldsymbol{\chi})$ are orthogonal, satisfying $\langle \boldsymbol{\phi}_i(\boldsymbol{\chi}), \boldsymbol{\phi}_j(\boldsymbol{\chi}) \rangle = \delta_{ij}$ and can be obtained by eigenvalue decomposition of the spatial or temporal correlation matrix of the flow quantities as described by Lumely (1967), Sirovich (1987) and Meyer et al. (2007). The flow quantity can be arranged in a matrix as follows:

$$\mathbf{M} = \mathbf{q}_1^n = [\mathbf{q}_1, \mathbf{q}_2, \dots, \mathbf{q}_n] \quad (3.32)$$

where \mathbf{q}_i ($i = 1, 2, 3 \dots n$) are column vectors containing the quantity components at each grid node at the time step of t_i ($i = 1, 2, 3 \dots n$). According to Taira et al. (2017), the POD modes can be obtained by employing Singular Value Decomposition (SVD) on the $m \times n$ matrix \mathbf{M} :

$$\mathbf{M} = \mathbf{U} \boldsymbol{\Sigma} \mathbf{V}^T \quad (3.33)$$

where the diagonal matrix $\boldsymbol{\Sigma} = \mathbf{diag}(\lambda_1, \lambda_2, \lambda_3 \dots \lambda_n)$ represents the singular values of the matrix \mathbf{M} and each diagonal value contains the energy carried by each POD mode. The left-singular vectors are denoted by \mathbf{U} and the right-singular vectors are given by \mathbf{V} . Both of them are orthogonal matrices and the column vectors of \mathbf{U} are the POD modes $\boldsymbol{\phi}_j$. The column vectors of \mathbf{V} represent the temporal coefficients $a_j(t)$.

The formulation presented above is used to perform POD with an economy-size SVD in MATLAB. It means that for a rectangular matrix $\mathbf{M}_{m \times n}$ with $m > n$, only the first n columns of the left singular vectors are calculated, resulting in $\boldsymbol{\Sigma}$ as a $n \times n$ matrix. This approach is possible due to the fast decay of the energy contained in the modes, resulting in a very small contribution of higher modes.

References

- Greenshields, C. J. (2015). OpenFOAM - The Open Source CFD Toolbox User Guide (2.4.0 ed.). OpenFOAM Foundation.
- Jasak, H. (1996). Error Analysis and Estimation for Finite Volume Method with Applications to Fluid Flow. Ph. D. thesis, Imperial College, University of London.
- Jones, W. P. & Launder, B. (1973). The calculation of low-Reynolds-number phenomena with a two-equation model of turbulence. *International Journal of Heat and Mass Transfer*, 16(6), 1119-1130.
- Lumley, J. L. (1967). The structure of inhomogeneous turbulent flows. *Atmospheric turbulence and radio wave propagation*.
- Menter, F. R. (1994). Two-equation eddy-viscosity turbulence models for engineering applications. *AIAA journal*, 32(8), 1598-1605.
- Menter, F. R., Kuntz, M. & Langtry, R. (2003). Ten years of industrial experience with the SST turbulence model. *Turbulence, heat and mass transfer*, 4(1), 625-632.
- Meyer, K. E., Pedersen, J. M. & Özcan, O. (2007). A turbulent jet in crossflow analysed with proper orthogonal decomposition. *Journal of Fluid Mechanics*, 583, 199-227.
- Rumsey, C. L., Allison, D. O., Biedron, R. T., Buning, P. G., Gainer, T. G., Morrison, J. H., Rivers, S. M., Mysko, S. J. & Witkowski, D. P. (2001). CFD Sensitivity Analysis of a Modern Civil Transport Near Buffet-Onset Conditions.
<https://ntrs.nasa.gov/archive/nasa/casi.ntrs.nasa.gov/20020015798.pdf>
- Samani, M. (2014). Study of Coherent Structures in Turbulent Flows Using Proper Orthogonal Decomposition. University of Saskatchewan.
- Sirovich, L. (1987). Turbulence and the dynamics of coherent structures. I. Coherent structures. *Quarterly of applied mathematics*, 45(3), 561-571.
- Spalart, P. R. & Allmaras, S. R. (1994). A One Equation Turbulence Model for Aerodynamic flows. *La Rech. Aéronautique* 1,5-21
- Spalart, P. R., Deck, S., Shur, M. L., Squires, K. D., Strelets, M. K. & Travin, A. (2006). A new version of detached-eddy simulation, resistant to ambiguous grid densities. *Theoretical and computational fluid dynamics*, 20(3), 181.

Taira, K., Brunton, S. L., Dawson, S. T., Rowley, C. W., Colonius, T., McKeon, B. J., Schmidt, O. T., Gordeyev, S., Theofilis, V. & Ukeiley, L. S. (2017). Modal analysis of fluid flows: An overview. *Aiaa Journal*, 4013-4041.

Wilcox, D. C. (1998). *Turbulence modeling for CFD* (Vol. 2, pp. 172-180). La Canada, CA: DCW industries.

Chapter 4

PAPER I: NUMERICAL SIMULATIONS OF FLOW OVER SINGLE AND TWO TANDEM CYLINDERS WITH DIFFERENT BURIAL RATIOS AND SPACINGS

A similar version of the draft of the paper that has been submitted to Ocean Engineering journal is presented in this chapter. The aim of this study is to investigate the flow over single and two tandem bottom-mounted cylinders under different configurations. The numerical simulations are carried out at a Reynolds number of 1.31×10^4 and the structures are subjected to a boundary layer flow with thickness of $\delta = 0.48D$. This analysis is potentially useful for on-bottom stability design of pipelines, risers and umbilicals. The results of the current study reveal the effects of different burial depths and different spacing between the cylinders on the drag and lift coefficients. They indicate that, for each burial configuration, there is a region of minimum hydrodynamic coefficients of both cylinders, which is found to be close to the recirculation length obtained from the single cylinder results.

Numerical Simulations of Flow Over Single and Two Tandem Cylinders with Different Burial Ratios and Spacings

Vinicius Serta Fraga^a, Guang Yin^{1a}, Muk Chen Ong^a, Per R. Nyström^b

^aDepartment of Mechanical and Structural Engineering and Materials Science, University of Stavanger, Stavanger, Norway

^bIKM Ocean Design AS, Norway

Abstract

High Reynolds number flow ($Re = U_\infty D/\nu$) at $Re = 1.31 \times 10^4$ over partially buried cylinders is investigated using two-dimensional (2D) Reynolds-averaged Navier-Stokes (RANS). The free stream velocity of the boundary layer flow is denoted as U_∞ . The diameter of the cylinders is denoted as D and the kinematic viscosity of the fluid is represented by ν . Single cylinder and two tandem cylinders with pitch ratios of $L/D = 2$ to 10 have been investigated as well as the effects of different burial ratios of $B/D = 0, 0.25$ and 0.5 . The cylinders are exposed to a boundary layer flow with a fixed thickness of $\delta = 0.48D$. To determine the grid resolution, mesh convergence studies are performed based on the hydrodynamic quantities such as drag and lift coefficients. The results obtained are compared with the results reported in the previous published experimental and numerical studies to validate the present numerical model. The variation of the hydrodynamic quantities, contours of the pressure and velocity as well as the streamlines for different configurations are analysed and discussed.

Keywords: tandem cylinders, partially buried, turbulent flow, RANS

1. Introduction

Significant amount of the oil and gas produced in the world is transported by pipelines placed on the seabed. For the on-bottom stability design, it is necessary to guarantee vertical and horizontal stability of the subsea pipelines under external loads induced by the waves and currents. In deep water conditions, waves have little effect on pipelines on the seabed and the main inline and crossflow forces on the pipelines are due to boundary layer flows caused by currents. Thus, the hydrodynamic quantities, such as drag and lift coefficients, are of extreme importance for a reliable subsea pipeline design.

¹ Corresponding author: guang.yin@uis.no

A few experimental investigations were conducted to investigate the flow over bottom-mounted cylinders or cylinders close to the seabed. Jensen et al. (1990) carried out experimental studies for the flow over a cylinder initially placed on the bottom wall with a temporal evolving scour hole beneath the cylinder at the Reynolds number range of 0.6×10^4 to 1×10^4 . It was found that vortex shedding appears at the beginning of the scour process with a sufficiently large gap between the cylinder and the bottom wall. Lei et al. (1999) also studied the flow over a cylinder at a subcritical Reynolds number for different gap ratios (G/D), where G is the gap between the cylinder and the bottom wall, and D is the diameter of the cylinder. They concluded that the incoming boundary layer flow and the gap ratio have great influence on the drag on the cylinder and the flow characteristics around the cylinder. Moreover, the vortex shedding was found to occur at a critical gap between $0.2D$ and $0.3D$ depending on the boundary layer thickness. Cokgor & Avci (2001) investigated the flow over single and two partially buried cylinders at the Reynolds number flows of 0.8×10^4 and 1.5×10^4 . It was concluded that both drag and lift coefficients decrease with the embedment of the cylinder and the variation of the drag coefficient with the buried ratio is nearly linear. It was also found that the addition of the second cylinder has significant impacts on the hydrodynamic quantities of the first cylinder. Lower values of the lift and drag coefficients were obtained on the downstream cylinder compared with those of the upstream one. Wang et al. (2015) conducted experimental investigations of the flow over single and tandem cylinders in proximity to a flat wall at the Reynolds number of 0.63×10^4 . The hydrodynamic forces and flow patterns showed strong dependency on the gap ratio between the cylinders and the wall as well as the distance between the two cylinders. Also, the vortex shedding started to be suppressed at a gap smaller than $0.3D$ between the cylinders and the wall.

Numerical investigations have also been carried out to analyze the flow over bottom-mounted cylinders or cylinders close to a wall. Akoz et al. (2019) performed numerical simulations to study the flow over cylinders with different burial ratios at subcritical Reynolds number. Different two-equation turbulence models were employed, and it was found that the $k - \omega$ Shear Stress Transport (SST) model provided similar results when compared with the experimental data. Zhao et al. (2007) used the $k - \omega$ turbulence model to simulate the boundary layer flow around a piggyback pipeline with different gap ratios between the pipeline and the wall. The simulations were validated against the flow over a single bottom-mounted cylinder under the Reynolds number of 1.8×10^4 . The results showed that the drag coefficient increases with the increasing gap ratio, while the mean lift coefficient decreases with the increasing gap ratio. Also, the vortex shedding is suppressed when the gap is below $0.3D$. Ong et al. (2010) investigated the boundary layer flow around a circular cylinder for different gap ratios and bottom wall roughness at high Reynolds number using the $k - \varepsilon$ turbulence model. It was

concluded that the variations of the drag coefficient with the gap ratio display similar behaviours at high and low Reynolds numbers, and the drag coefficient decreases when the surface roughness is increased. Moreover, the onset of the vortex shedding was at a gap ratio of $0.25D$. Simulations using the two-equation $k - \omega$ turbulence model were performed by An et al. (2011) to analyze the high Reynolds number flow over a partially buried cylinder on a permeable bottom wall. The values of the hydrodynamic quantities decrease linearly with the increase of the burial depth. Li et al. (2018) carried out Large Eddy Simulations (LES) of the flow around two tandem cylinders close to the bottom wall at a high Reynolds number. The effects of the gap ratio and the distance between the cylinders were investigated. It was concluded that the drag coefficient decreases when the cylinders are placed closer to the wall and with the increasing distance between the two cylinders. In addition, the hydrodynamic coefficients of the downstream cylinder are significant lower compared with those of the upstream cylinder.

Two-dimensional (2D) flow over single and two tandem cylinders with different burial ratios (B/D), where B is the burial depth, and different pitch ratios (L/D), where L is the distance between the centers of the cylinders, is investigated in the current study. This is a common configuration that appears in ocean engineering. The turbulent flow is resolved by employing the 2D Reynolds-averaged Navier-Stokes (RANS) equations combined with $k - \omega$ SST turbulence model. The Reynolds number is 1.31×10^4 based on the diameter of the cylinder and the free-stream velocity, and the boundary layer thickness is $\delta = 0.48D$. The paper is organized as follows: the governing equations and numerical methods are presented in Section 2. Section 3 gives the computational overview, the convergence studies and the validation studies. Section 4 presents the results and discussions. Finally, the conclusion is presented in Section 5.

2. Governing Equations and Numerical Methods

2.1 Mathematical formulation

Since the cylinders are placed on the flat wall with buried ratio, there is no vortex shedding behind the cylinders. Therefore, the 2D steady RANS equations of the conservation of mass and momentum are solved in the present study, which are given as:

$$\frac{\partial u_i}{\partial x_i} = 0 \quad (1)$$

$$u_j \frac{\partial u_i}{\partial x_j} = -\frac{1}{\rho} \frac{\partial P}{\partial x_i} + \nu \frac{\partial^2 u_i}{\partial x_j \partial x_j} - \frac{\overline{u'_i u'_j}}{\partial x_j}, \quad (2)$$

where $i, j = 1, 2$ denote the streamwise and the cross-stream directions, respectively. u_1 and u_2 (also represented as u and v) are the corresponding time-averaged velocity components. ρ is the fluid density, the time-averaged pressure is denoted as P and the Reynolds stress components is given by $\overline{u'_i u'_j}$, where u'_i is the fluctuation part of the velocities.

According to the Boussinesq approximation, the Reynolds stress components can be expressed as:

$$\overline{u'_i u'_j} = \nu_t \left(\frac{\partial u_i}{\partial x_j} + \frac{\partial u_j}{\partial x_i} \right) - \frac{2}{3} k \delta_{ij} \quad (3)$$

where the turbulent kinetic energy is denoted as k and δ_{ij} is the Kronecker delta.

The $k - \omega$ SST turbulence model (Menter, 1994 and Menter et al. 2003) is a hybrid model of the $k - \varepsilon$ (Jones & Launder, 1973) and the $k - \omega$ (Wilcox, 1998) models. The $k - \varepsilon$ model is applied away from the wall in the free-stream flow and the $k - \omega$ model is used within the near-wall region. The equations for k and ω are written as:

$$\frac{D(\rho k)}{Dt} = \widetilde{P}_k - \beta^* \rho k \omega + \frac{\partial}{\partial x_i} \left[(\mu + \sigma_k \mu_t) \frac{\partial k}{\partial x_i} \right] \quad (4)$$

$$\frac{D(\rho \omega)}{Dt} = \alpha \rho S^2 - \beta \rho \omega^2 + \frac{\partial}{\partial x_i} \left[(\mu + \sigma_\omega \mu_t) \frac{\partial \omega}{\partial x_i} \right] + 2(1 - F_1) \rho \sigma_{\omega 2} \frac{\partial k}{\partial x_i} \frac{\partial \omega}{\partial x_i} \quad (5)$$

$$\widetilde{P}_k = \min \left[\mu_t \frac{\partial u_i}{\partial x_j} \left(\frac{\partial u_i}{\partial x_j} + \frac{\partial u_j}{\partial x_i} \right), 10 \beta^* \rho k \omega \right] \quad (6)$$

The constant ϕ_i , where $i = 1, 2$, represents the $k - \omega$ model and the $k - \varepsilon$ model constants, respectively. The constant ϕ in the SST model can be described as:

$$\phi = F_1 \phi_1 + (1 - F_1) \phi_2 \quad (7)$$

$$F_1 = \tanh \left\{ \left\{ \min \left[\max \left(\frac{\sqrt{k}}{\beta^* \omega y}, \frac{500 \nu}{y^2 \omega}, \frac{4 \rho \sigma_{\omega 2} k}{CD_{k\omega} y^2} \right) \right] \right\}^4 \right\} \quad (8)$$

$$CD_{k\omega} = \max \left(2 \rho \sigma_{\omega 2} \frac{1}{\omega} \frac{\partial k}{\partial x_i} \frac{\partial \omega}{\partial x_i}, 10^{-10} \right) \quad (9)$$

where the distance to the closest wall is given by y and the positive part of the cross-diffusion

term in (4) is expressed by $CD_{k\omega}$. The turbulent viscosity is given by:

$$v_t = \frac{a_1 k}{\max(a_1 \omega, SF_2)} \quad (10)$$

$$F_2 = \tanh \left[\left[\max \left(2 \frac{\sqrt{k}}{\beta^* \omega y}, \frac{500\nu}{y^2 \omega} \right) \right]^2 \right] \quad (11)$$

where the invariant measure of the strain rate is denoted by S and the constants employed in the SST model are: $\beta^* = 0.09$, $a_1 = 0.31$, $\beta_1 = 0.075$, $\beta_2 = 0.083$, $\sigma_{k1} = 0.85$, $\sigma_{k2} = 1$, $\sigma_{\omega1} = 0.5$, $\sigma_{\omega2} = 0.856$, $\alpha_1 = 0.555$ and $\alpha_2 = 0.44$.

2.2 Numerical methods

The code OpenFOAM is used in the present simulations. It is an open source Computational Fluid Dynamics (CFD) tool with a customized C++ library for numerical simulations which has been vastly applied for scientific and engineering research. The solver based on the algorithm of Semi-Implicit Method for Pressure-Linked Equations (SIMPLE), simpleFoam, is used in the present study. Gauss linear is employed for gradient and divergence; Gauss linear corrected is applied for Laplacian.

3. Computational Overview, Convergence and Validation Studies

3.1 Computational overview

Figure 1 displays the computational domain used in the present study. Single and two tandem cylinders are considered. The burial ratios B/D are 0, 0.25 and 0.5. In the cases with tandem cylinders, different distances L/D between the centers of the cylinders are studied: 2, 4, 6, 8 and 10. The height of the computational domain is given by $L_H = 20D$, the length between the inlet and the center of the upstream cylinder is $L_U = 11.5D$ and the distance from the center of the downstream cylinder to the outlet is $L_D = 35D$. Ong et al. (2010) found that a domain with $L_H = 10D$, $L_U = 10D$ and $L_D = 20D$ is large enough to avoid far-field effects, which indicates that the present computational domain is sufficiently large. The boundary conditions shown in Figure 1 are the following:

- (i) At the inlet, the streamwise velocity has a logarithmic profile obtained experimentally by Arie et al. (1975). A fixed boundary layer thickness of $\delta = 0.48D$ is applied. The cross-stream velocity is set to zero and the pressure is prescribed as zero gradient.

$$u_1(y) = \min\left\{\frac{u_*}{\kappa} \ln\left(\frac{y}{z_w}\right), U_\infty\right\} \quad (12)$$

$$u_2(y) = 0 \quad (13)$$

$$k(y) = \max\left\{C_\mu^{-0.5} \left(1 - \frac{y}{\delta}\right)^2 u_*^2, 0.0001U_\infty^2\right\} \quad (14)$$

$$\omega = \frac{\kappa^{0.5}}{C_\mu^{0.5} l} \quad (15)$$

$$l = \min\left\{\kappa y \left(1 + 3.5 \frac{y}{\delta}\right)^{-1}, C_\mu \delta\right\} \quad (16)$$

where the friction velocity is given by $u_* = \kappa U_\infty / \ln(\delta/z_w)$, the roughness parameter is set as $z_w = 1 \times 10^{-6}$, the constant $C_\mu = 0.09$, the Von Kármán constant is $\kappa = 0.41$ and l is the turbulent length scale. This boundary layer flow profile has been used in Ong et al. (2010), Prsic et al. (2016) and Li et al. (2018).

- (ii) At the outlet boundary, the velocities are set as zero gradient and the pressure is prescribed as zero.
- (iii) On the cylinders surfaces and at the bottom wall, no-slip condition is applied, giving $u_1 = u_2 = 0$. The pressure is prescribed as zero gradient. On the walls, a $y^+ < 1$ is satisfied, in which y^+ is given as:

$$y^+ = \frac{u_* \Delta y}{\nu} \quad (17)$$

where Δy is the normal distance between the wall and the center of the first grid layer.

- (iv) At the top, the velocities and the pressure are set as zero normal gradient.

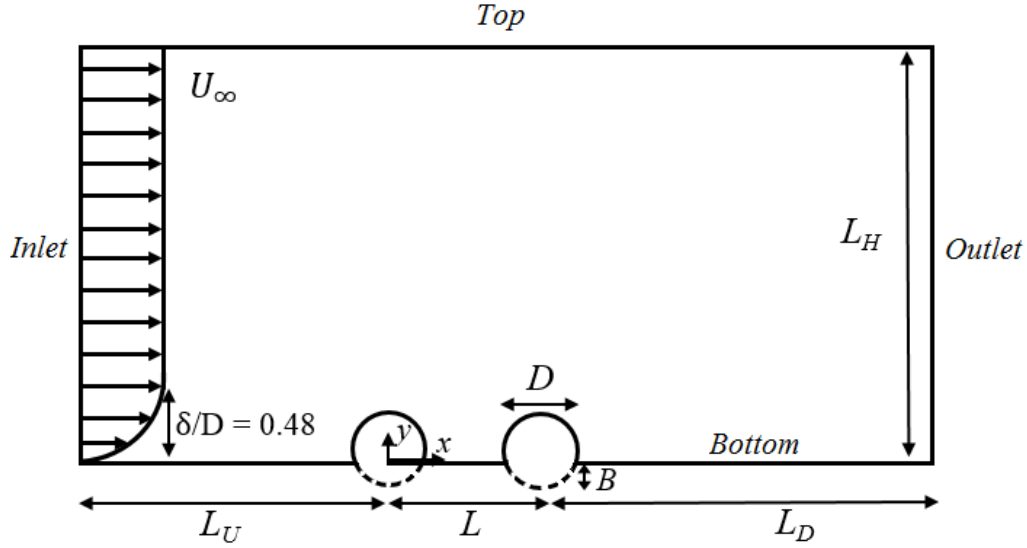


Figure 1: Computational domain and boundary conditions

3.2 Convergence studies

Mesh convergence studies are carried out for the single cylinder and all the configurations with the two tandem cylinders. The drag coefficient C_D and the lift coefficient C_L are computed by the expressions:

$$C_D = \frac{F_x}{\frac{1}{2}\rho U_\infty^2 D} \quad (18)$$

$$C_L = \frac{F_y}{\frac{1}{2}\rho U_\infty^2 D} \quad (19)$$

where the force in the streamwise direction is denoted as F_x and the force in the cross-stream direction is denoted as F_y .

For each configuration, three meshes with an increment of at least 30% in the total number of cells are analysed. The results of the hydrodynamic quantities and the recirculation length (L_W) from the back face of the downstream cylinder for the cases with $B/D = 0$ are presented in Table 1. The setup with a single cylinder, represented by Cases 1 to 3, show good convergence for C_D and C_L with the relative differences lower than 1% between cases. Cases 4 to 6 show the results for the two cylinders cases with $L/D = 2$, and differences lower than 1% between cases are achieved. The results for the cylinders with $L/D = 4$ (Cases 7 to 9) display good convergence, with changes in the hydrodynamic quantities lower than 1%. Cases 10 to 12 with $L/D = 6$, also give good convergence with relative differences around 1% between the cases. In

addition, with $L/D = 8$ (Cases 13 to 15), a good convergence is obtained with differences in C_D and C_L around 1%. Lastly, for $L/D = 10$ between the two cylinders (Cases 15 to 18), the hydrodynamic quantities of the upstream cylinder give good convergence with relative differences lower than 1%. The differences of hydrodynamic quantities of the downstream cylinder is large, however due to their small values close to zero, the results can still be reasonable.

Table 1: Results for the cases with $B/D = 0$ based on different numbers of grids

Case	No. of cells	C_{D1}	C_{L1}	C_{D2}	C_{L2}	L_W	
$B/D = 0$ Single cylinder	1	35096	0.752	0.459	-	-	10.560
	2	45868	0.751	0.461	-	-	10.153
	3	61118	0.754	0.459	-	-	9.724
$B/D = 0$ $L/D = 2$	4	39322	0.976	0.582	-0.544	-0.104	5.847
	5	54024	0.980	0.581	-0.546	-0.104	5.985
	6	68786	0.981	0.583	-0.549	-0.105	5.917
$B/D = 0$ $L/D = 4$	7	42447	0.871	0.533	-0.418	-0.137	4.516
	8	55584	0.871	0.532	-0.419	-0.137	4.173
	9	71524	0.873	0.531	-0.422	-0.139	4.428
$B/D = 0$ $L/D = 6$	10	41424	0.809	0.501	-0.266	-0.097	3.816
	11	55038	0.812	0.499	-0.272	-0.098	3.524
	12	71125	0.813	0.499	-0.274	-0.099	3.832
$B/D = 0$ $L/D = 8$	13	41966	0.774	0.481	-0.114	-0.053	3.522
	14	55258	0.777	0.479	-0.119	-0.057	3.539
	15	71098	0.778	0.479	-0.122	-0.057	3.749
$B/D = 0$ $L/D = 10$	16	42015	0.754	0.468	0.015	-0.002	3.630
	17	55420	0.756	0.467	0.010	-0.005	3.407
	18	73153	0.758	0.466	0.008	-0.007	3.631

The results for the cases with $B/D = 0.25$ are given in Table 2. In the cases with single cylinder (Cases 19 to 21), the relative differences of the hydrodynamic quantities between cases are lower than 1%. The configurations with two cylinders and L/D of 2 and 4 (Cases 22 to 27) give relative differences around 1% in C_{D1} , C_{L1} and C_{D2} , C_{L2} . With a distance of $6D$ between the centers of the cylinders (Cases 28 to 30), the upstream cylinder has a good convergence with differences lower than 1% based on the hydrodynamic quantities and the relative differences of the hydrodynamic quantities of the downstream cylinder between cases are lower than 4%.

Cases 31 to 36 also have good convergence, with relative differences around 1% for the drag and lift coefficients for both cylinders.

Table 2: Results for the cases with $B/D = 0.25$ based on different numbers of grids

Case	No. of cells	C_{D1}	C_{L1}	C_{D2}	C_{L2}	L_W	
$B/D = 0.25$ Single cylinder	19	34016	0.493	0.407	-	-	7.455
	20	43866	0.491	0.412	-	-	7.175
	21	55684	0.490	0.412	-	-	6.818
$B/D = 0.25$ $L/D = 2$	22	40708	0.622	0.639	-0.361	0.286	3.915
	23	50820	0.620	0.642	-0.360	0.285	3.881
	24	66288	0.612	0.632	-0.354	0.282	3.897
$B/D = 0.25$ $L/D = 4$	25	40774	0.528	0.483	-0.183	0.188	3.050
	26	51720	0.527	0.484	-0.182	0.188	3.076
	27	65829	0.521	0.476	-0.180	0.187	2.909
$B/D = 0.25$ $L/D = 6$	28	40133	0.493	0.417	-0.050	0.149	2.826
	29	51436	0.493	0.418	-0.051	0.149	2.649
	30	67748	0.494	0.416	-0.052	0.147	2.760
$B/D = 0.25$ $L/D = 8$	31	41618	0.478	0.382	0.060	0.150	2.936
	32	52524	0.477	0.383	0.058	0.150	2.854
	33	68640	0.478	0.381	0.057	0.148	2.674
$B/D = 0.25$ $L/D = 10$	34	42004	0.472	0.366	0.147	0.175	3.540
	35	53274	0.471	0.367	0.145	0.176	3.300
	36	70530	0.472	0.365	0.145	0.173	3.283

Table 3 gives the results for the configurations with $B/D = 0.5$. In the first two configurations (Cases 37 to 42), relative differences lower than 1% are found for the hydrodynamic quantities. The upstream cylinder of Cases 43 to 45 also has good convergence with differences lower than 1% for the drag and lift coefficients. The relative differences of C_{L2} between cases are lower than 1% and due to the small value of C_{D2} , their relative differences between cases can be large. A good convergence is also achieved for the following three configurations (Cases 46 to 54) and the relative differences between cases are lower than 1% for both hydrodynamic quantities.

Table 3: Results for the cases with $B/D = 0.5$ based on different numbers of grids

Case	No. of cells	C_{D1}	C_{L1}	C_{D2}	C_{L2}	L_W	
Single cylinder $B/D = 0.5$	37	25097	0.268	0.329	-	-	4.705
	38	33294	0.266	0.331	-	-	4.720
	39	44063	0.265	0.333	-	-	4.511
$B/D = 0.5$ $L/D = 2$	40	31967	0.305	0.419	-0.128	0.263	2.506
	41	41920	0.302	0.421	-0.126	0.262	2.421
	42	55508	0.301	0.422	-0.124	0.262	2.381
$B/D = 0.5$ $L/D = 4$	43	34492	0.265	0.316	-0.010	0.170	2.072
	44	45168	0.264	0.318	-0.008	0.171	1.987
	45	60368	0.263	0.320	-0.008	0.171	1.914
$B/D = 0.5$ $L/D = 6$	46	35502	0.256	0.282	0.075	0.158	2.242
	47	46908	0.254	0.285	0.076	0.160	2.284
	48	62393	0.253	0.286	0.076	0.161	2.315
$B/D = 0.5$ $L/D = 8$	49	37017	0.256	0.277	0.130	0.183	2.710
	50	48648	0.254	0.280	0.130	0.186	3.074
	51	64418	0.253	0.281	0.130	0.187	2.857
$B/D = 0.5$ $L/D = 10$	52	38532	0.259	0.283	0.163	0.215	3.248
	53	50388	0.257	0.287	0.161	0.218	3.381
	54	65768	0.256	0.289	0.161	0.219	3.375

Moreover, the streamwise velocity profiles along the streamwise direction at $y/D = 0.5$ and the pressure on the bottom wall for the single cylinder configurations with $B/D = 0$ (Cases 1 to 3), $B/D = 0.25$ (Cases 19 to 21) and $B/D = 0.5$ (Cases 37 to 39) are presented in Figure 2, and a good agreement between the cases is displayed. Thus, it can be concluded that sufficient grid convergence has been achieved for all the finest meshes of each configuration. Therefore, they are used for discussion in the following sections. An example of the mesh used in the present study is given in Figure 3 for the configuration with two cylinders and $L/D = 2$ (Case 6).

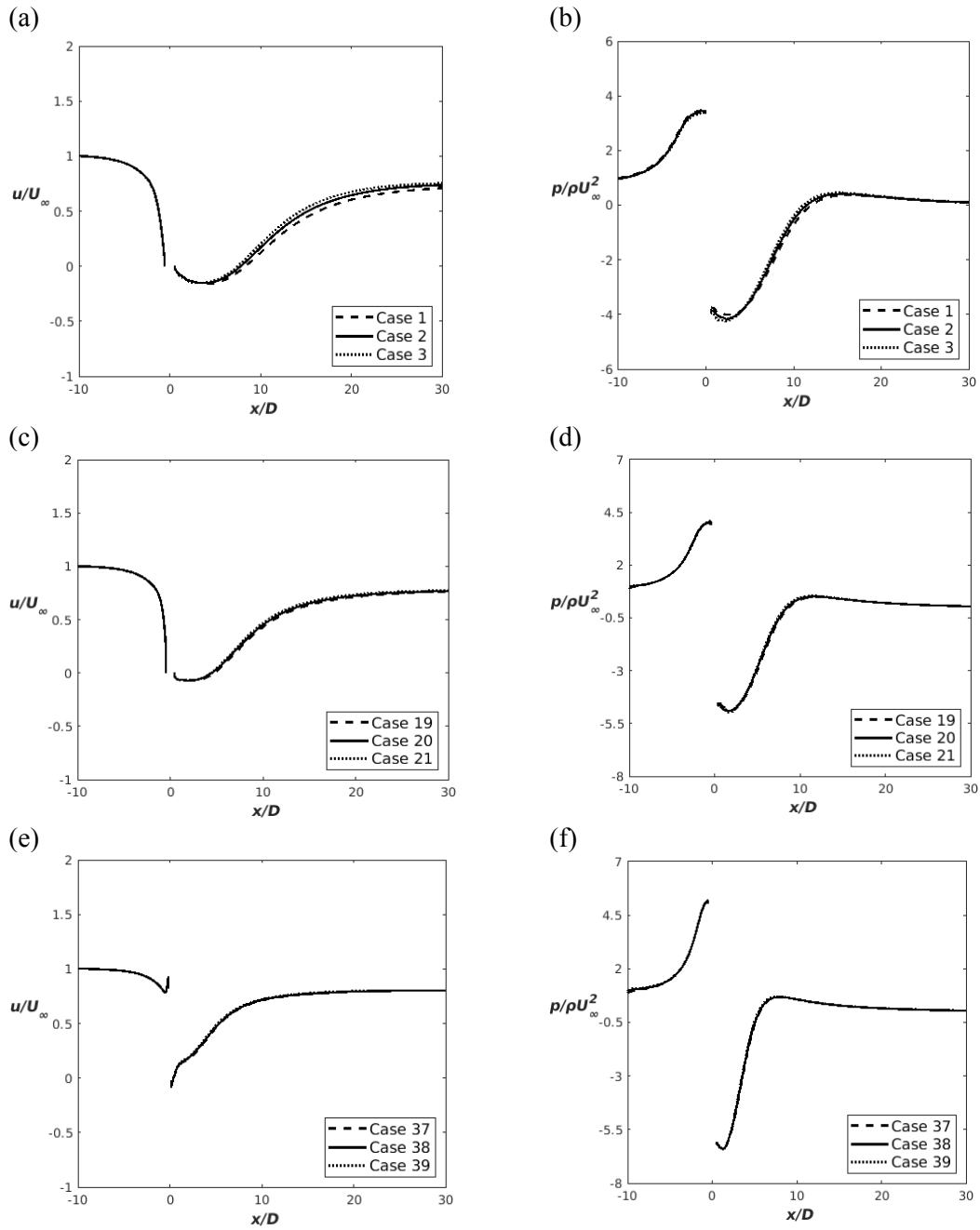


Figure 2: Profiles of the streamwise velocity (a, c, e) at $y/D = 0.5$ and the pressure on the bottom wall (b, d, f) for the single cylinder cases with different B/D s.

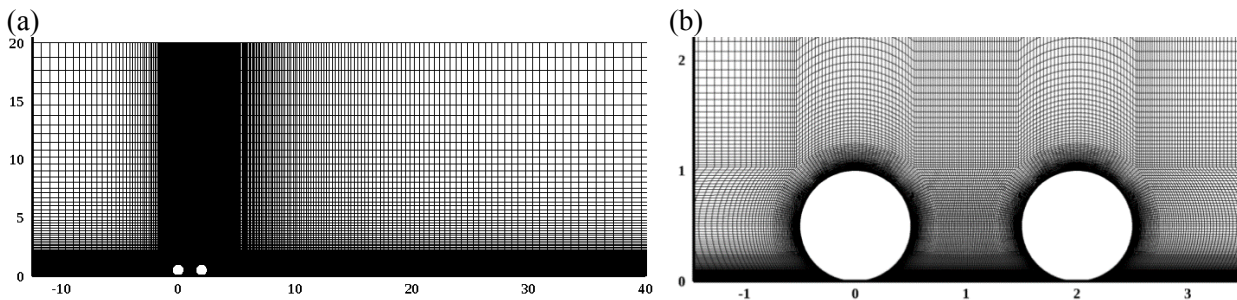


Figure 3: The computational mesh of two cylinders (Case 6): (a) full domain and (b) zoom-in view close to the cylinders

3.3 Validation studies

The results obtained for the hydrodynamic quantities are validated against the previous experimental data and numerical results. Table 4 shows the results obtained by the present study with one cylinder and two cylinders with $L/D = 2$ and 4. The cases are also validated against two cylinders cases with a small gap ratio between the cylinders and the bottom wall in the previous studies. For these cases, only the drag coefficient for the upstream cylinder is considered due to the significant reduction in the lift coefficient when there is flow beneath the cylinder as found by Lei et al. (1999) and Zhao et al. (2007). Also, the flow that comes out of the gap between the upstream cylinder and the bottom wall can influence the drag force on the downstream cylinder as reported in Li et al. (2017). It can be observed that the hydrodynamic quantities for the single cylinder case is in satisfactory agreement with the literature. In addition, the value of C_{D1} of the two tandem cylinders cases give a good agreement with relative differences lower than 6% compared with the drag coefficients reported by Li et al. (2017).

Table 4: Hydrodynamic quantities of Cases 3, 6 and 9 compared with the experimental and numerical data

Configuration	Author	Flow conditions	C_{D1}	C_{L1}
Single cylinder	Present	$Re = 1.31 \times 10^4, B/D = 0, \delta/D=0.48$	0.754	0.459
	Zhao et al. (2007)	$Re = 1.8 \times 10^4, B/D = 0$	0.710	0.400
	Lei et al. (1999)	$Re = 1.31 \times 10^4, B/D = 0, \delta/D=0.48$	0.825	0.530
	Ong et al. (2010)	$Re = 1.31 \times 10^4, G/D = 0.1, \delta/D=0.48$	0.750	-
Two cylinders	Present	$Re = 1.31 \times 10^4, B/D = 0, L/D=2, \delta/D=0.48$	0.981	-
	Present	$Re = 1.31 \times 10^4, B/D = 0, L/D=4, \delta/D=0.48$	0.873	-
	Li et al. (2017)	$Re = 1.31 \times 10^4, G/D = 0.1, L/D=2, \delta/D=0.48$	0.930	-
	Li et al. (2017)	$Re = 1.31 \times 10^4, G/D = 0.1, L/D=5, \delta/D=0.48$	0.860	-

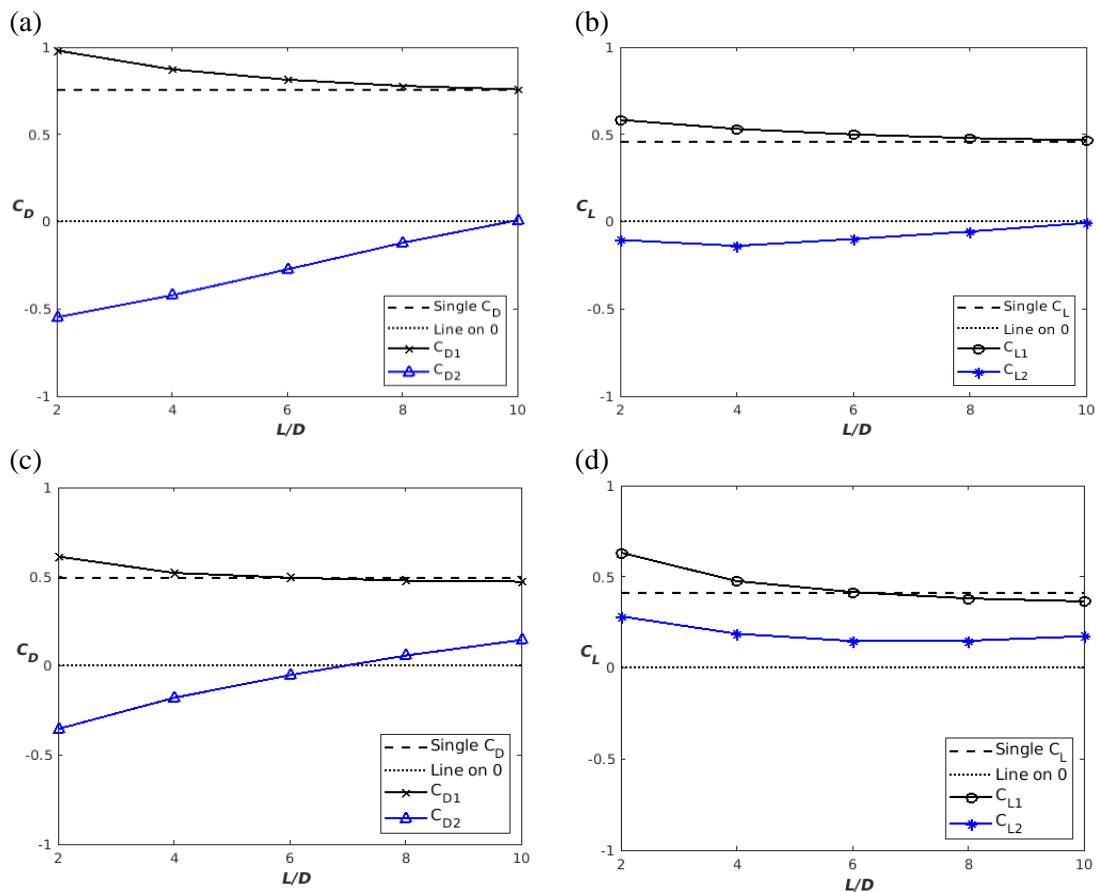
4. Results and Discussion

4.1 Hydrodynamic quantities

The variations of the hydrodynamic quantities of the two cylinders with L/D for different B/D compared with those of a single cylinder is given in Figure 4. For all B/D s, the drag and lift coefficients of the upstream cylinder decrease with the increasing L/D . For the case with $B/D = 0$, the drag and lift of the downstream cylinder are negative. When $L/D = 10$, which is close to the recirculation length behind a single cylinder as shown in Case 3, the value of C_{D2}

is almost 0. With $B/D = 0.25$, both values of C_{D1} and C_{L1} for the upstream cylinder decrease when compared with those of $B/D = 0$. The zero crossing of C_{D2} is found when $L/D \approx 7$, which is also close to the recirculation length behind the single cylinder with $B/D = 0.25$ given by Case 21 in Table 2. Then, for $L/D > 7$, the value of C_{D2} of the downstream cylinder increases with the increasing L/D . With this L/D , it is also found that the value of C_{L2} of the downstream cylinder starts to increase with the increasing L/D . In addition, for $B/D = 0.5$, the critical value of L/D for zero C_{D2} decreases to 4. This is also close to the length of the recirculation motion behind the single cylinder case (Case 39). These results indicate that a minimal value of C_{D2} of the downstream cylinder is achieved when the downstream cylinder is placed at the edge of the recirculation region behind the upstream cylinder.

Furthermore, it can be seen that with the increasing B/D , the values of C_D of both the upstream and the downstream cylinders decrease compared with those of $B/D = 0$ and this is because the cylinders are subjected to a decreasing averaged flow velocity, which is consistent with what has been found in Akoz et al. (2019) and Zhao et al. (2019). In addition, due to effects of the upstream cylinder, the value of C_D for the downstream cylinder is lower than that of the upstream cylinder, which was also reported in Cokgor & Avci (2001), Wang et al. (2015) and Li et al. (2017).



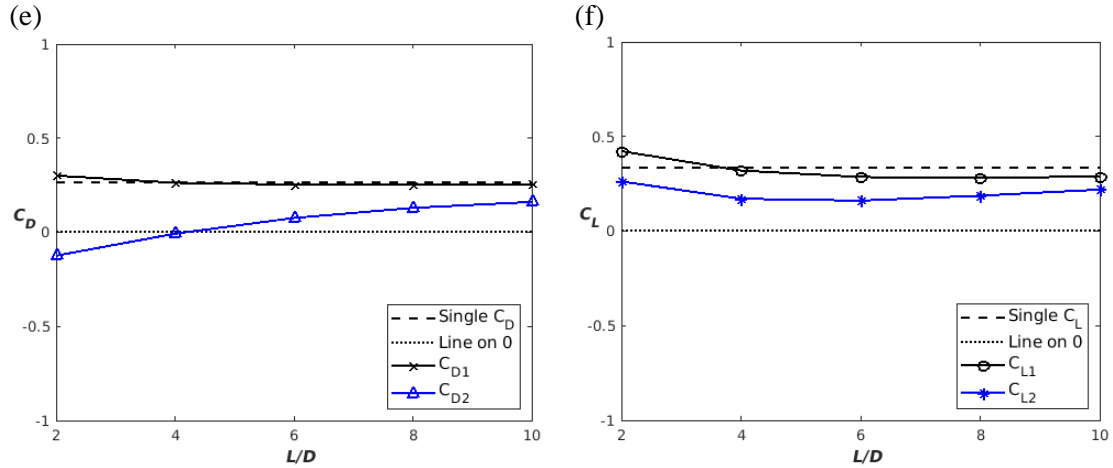


Figure 4: Evolution of C_D (a, c, e) and C_L (b, d, f) with the increase of L/D for different burial ratios: (a, b) $B/D = 0$, (c, d) $B/D = 0.25$, and (e, f) $B/D = 0.5$

4.2 Pressure and horizontal velocity contours

In order to understand the behaviour of the variation of the hydrodynamic quantities with different configurations, the contours of the pressure and the streamwise velocity for different cases are analysed in this section. For all B/D s, the contours for a single cylinder are presented for comparison in Figures 5 to 7 (a) and (b). For the single cylinder case, when the flow hits the cylinder, it is slow down, which creates a high-pressure region in front of the cylinder. When the flow separates from the cylinder surface, a large recirculation motion is formed behind the cylinder where a low-pressure region is formed. For the two cylinders in tandem cases, the downstream cylinder causes a further blockage effect to the flow separated from the upstream cylinder and then a stronger recirculation motion is formed between the two cylinders compared with the one behind the single cylinder. The amplitude of the negative-pressure region between the two cylinders becomes stronger than that behind the single cylinder and the downstream cylinder, which explains the strong negative value of C_{D2} in Figure 4 (a) and the higher value of C_{D1} compared with that of the single cylinder.

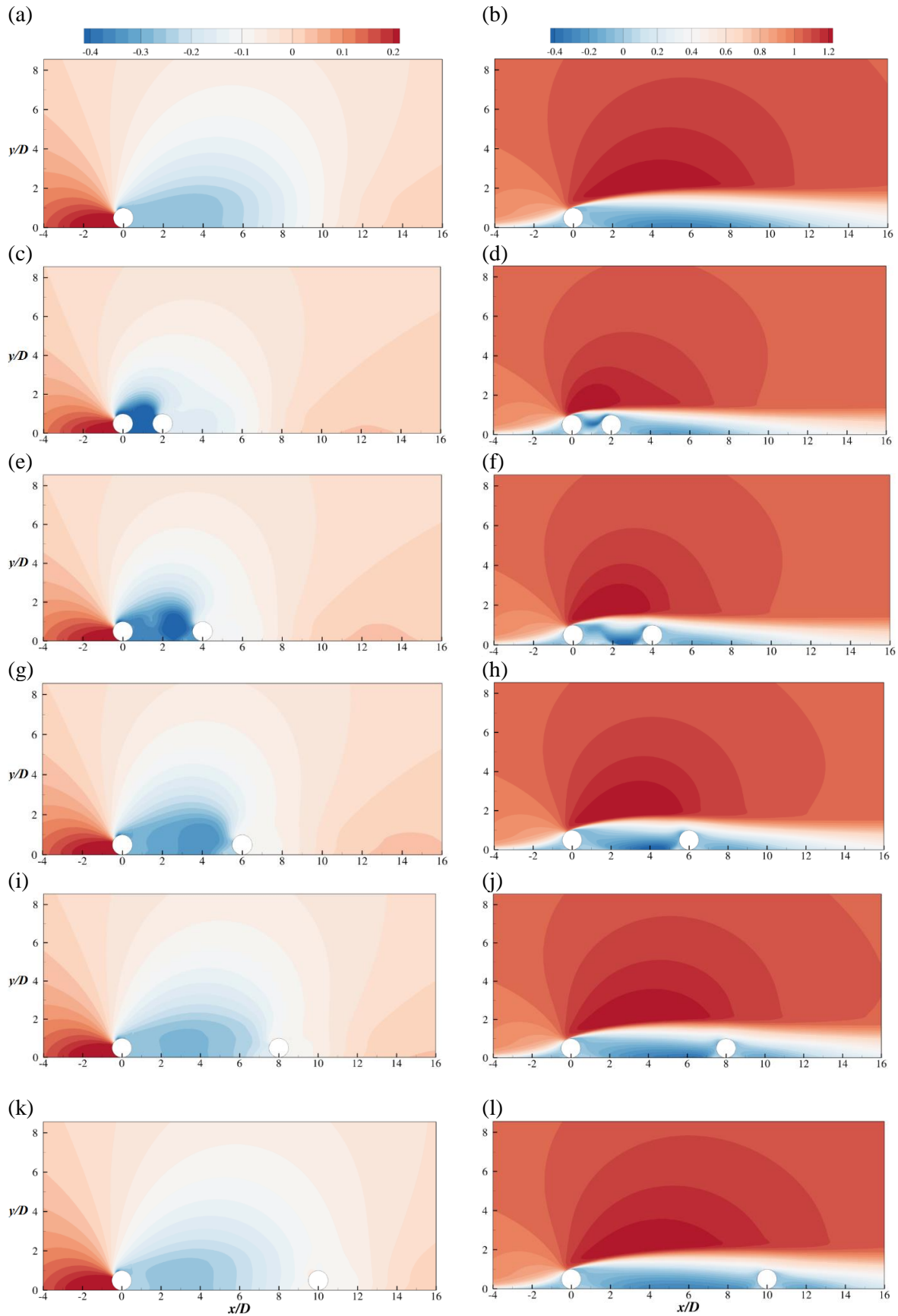


Figure 5: The contours of the pressure (a, c, e, g, i, k) and the streamwise velocity (b, d, f, h, j, l) with $B/D = 0$ for different L/D s

Furthermore, with the increasing L/D , the blockage effect of the downstream cylinder to the flow is reduced and the amplitude of the negative pressure region between the two cylinders is decreased, which results in the decreasing value of C_{D1} and the absolute value of C_{D2} with the increasing L/D . With $L/D = 10$, the pressure behind and in front of downstream cylinder are almost the same, resulting in a zero value of C_{D2} . With this L/D , the value of C_{D1} is almost the same as that of the single cylinder. Moreover, when the flow separates from the upstream cylinder surface, the flow is accelerated as shown in the streamwise velocity contours in Figures 5 to 7 and a negative-pressure region is formed above the cylinders, which creates a lift for these cylinders. Also, these figures show that the streamwise velocity above the upstream cylinder decreases with the increasing L/D , which results in a higher-pressure region above the upstream cylinder, and as a consequence, lower lift coefficients. It can be seen from the pressure contour around the downstream cylinder that the amplitude of the negative pressure above the cylinder is lower than that below the cylinder, resulting a negative lift force on the cylinder as shown in Figure 4 (b). Furthermore, with the increasing L/D , the amplitude of the negative pressure below the cylinder is reduced and thus resulting in a decreasing absolute value of C_{L2} as shown in Figure 4 (b).

Figure 6 displays the pressure and the streamwise velocity contours of the cases with $B/D = 0.25$. With the reducing blockage effect of the buried cylinder to the flow, the pressure difference between the back and front face of the cylinder is reduced. Similar behaviour of the pressure region between the two cylinders are shown for $B/D = 0.25$ with $L/D < 6$ compared with the cases with $B/D = 0$. The critical value of L/D for C_{D2} is around 7 as shown in Figures 6 (g) and (i). It can be seen that with $L/D > 6$, the pressure in front of the downstream cylinder becomes positive which results in positive value of C_{D2} for this cylinder.

The pressure and the streamwise velocity contours of the cases with $B/D = 0.5$ are shown in Figure 7. The critical value of L/D for C_{D2} is around 4, where the pressure between the front and back faces of the downstream cylinders is almost zero. Also, due to the reduced pressure difference and velocity around the two cylinders, their hydrodynamic quantities are lowest compared with $B/D = 0$ and 0.25. Also, the velocity and pressure contours around the upstream cylinders shown in Figures 7 (g) to (l) tend to be close to the contours observed in the single cylinder case as shown in Figures 7 (a) and (b), indicating that the influence of the downstream cylinder to the flow around the upstream cylinder is small at large L/D s.

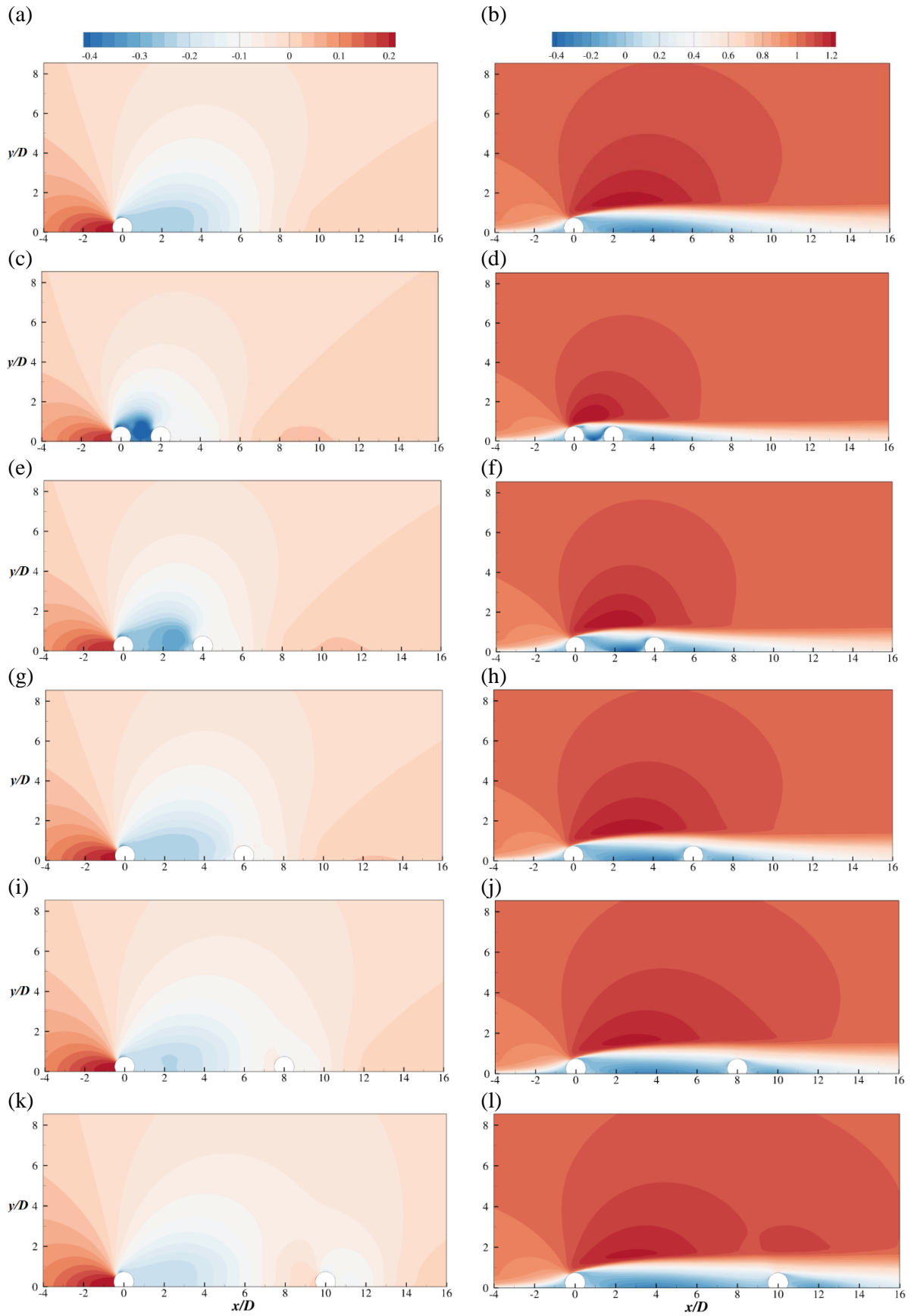


Figure 6: The contours of the pressure (a, c, e, g, i, k) and the streamwise velocity (b, d, f, h, j, l) with $B/D = 0.25$ for different L/D s

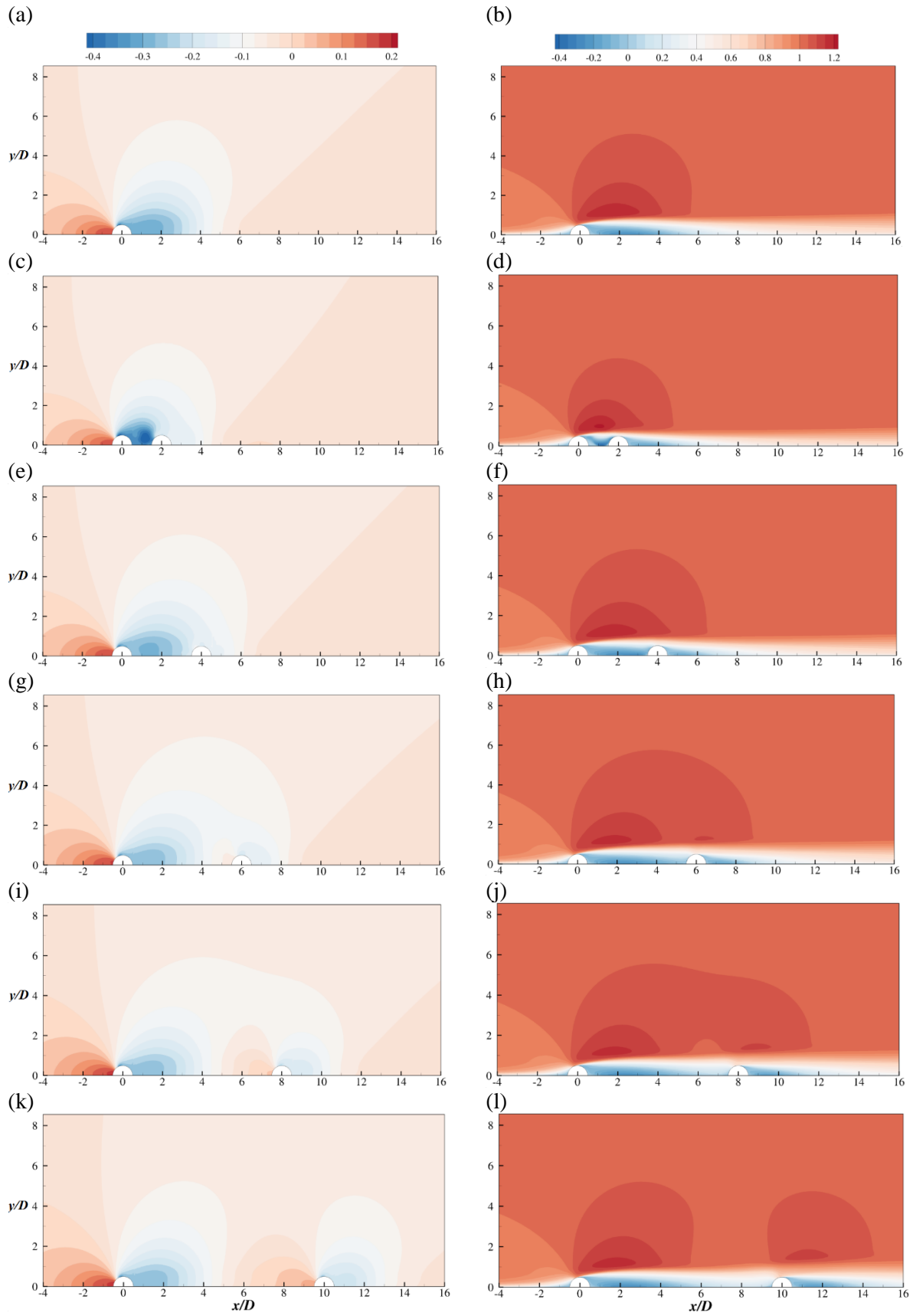


Figure 7: The contours of the pressure (a, c, e, g, i, k) and the streamwise velocity (b, d, f, h, j, l) with $B/D = 0.5$ for different L/D s

4.3 Streamlines

Figure 8 displays the streamlines of the flow for the single cylinder and two cylinders in tandem with different L/D s and $B/D = 0$. The streamlines shown in Figure 8 (a) display three recirculation vortices, in which the main vortex is located downstream the cylinder. It is resulted from the flow separation and the length of the vortex is found to be around $10D$. For all cases, as shown in Figures 8 (a) to (f), there are two small vortices located around the bottom of the two cylinders. The small recirculation motion around the front corner of the upstream cylinder is formed due to the downward flow caused by the blockage effect of the cylinder to the flow. The small vortices around the back corner of the upstream cylinder and the two corners of the downstream cylinder are induced by the two large recirculation motions behind the two cylinders. Figure 8 (b) shows three strong vortices between the two cylinders with $L/D = 2$, which indicates that the energy is highly concentrated in that region, with the strong vorticity contributing to the strong negative pressure. The recirculation length behind the downstream cylinder tends to decrease with the increasing L/D because the recirculation motion behind the upstream cylinder becomes larger due to the increasing L/D and less flow is separated from the downstream cylinder.

The streamlines for the cases with $B/D = 0.25$ are displayed in Figure 9. There are still three main vortices around the single cylinder as shown in Figure 9 (a), which is similar to those in Figure 8 (a). However, the sizes of the large recirculation motions are smaller compared with that in Figure 8 (a) due to the lower velocity of the incoming flow with the increasing B/D . The sizes of the large vortex located behind the downstream cylinder shown in Figures 9 (b) to (e) decrease, which shows a similar behaviour of the recirculation length with the increasing L/D to that in Figure 8 (b) to (e). However, the recirculation length may also reach the minimum value when the second cylinder is placed with the critical L/D around 7. Moreover, the large vortex located between the cylinders starts to detach from the front face of the downstream cylinder with $L/D = 10$, as displayed in Figure 9 (f).

Figure 10 shows the streamlines for the cases with $B/D = 0.5$ and all the small vortices located around the corners of the cylinders are almost suppressed and the streamlines are attached to the cylinders surfaces, which was also found in Tauqeer et al. (2017) and Gao & Mi (2009). Also, the sizes of the recirculation motion behind the downstream cylinder are reduced compared with other B/D s, which is also shown in Tables 1, 2 and 3. The recirculation length behind the downstream cylinder decreases with the increasing L/D and it reaches a minimum length with $L/D = 4$ and then starts to increase with the further increasing L/D . As shown in Figures 10 (e) and (f), the main vortex between the cylinders are detached from the downstream

cylinder, which indicates that the flows over both cylinders are becoming similar to the flow over the single cylinder.

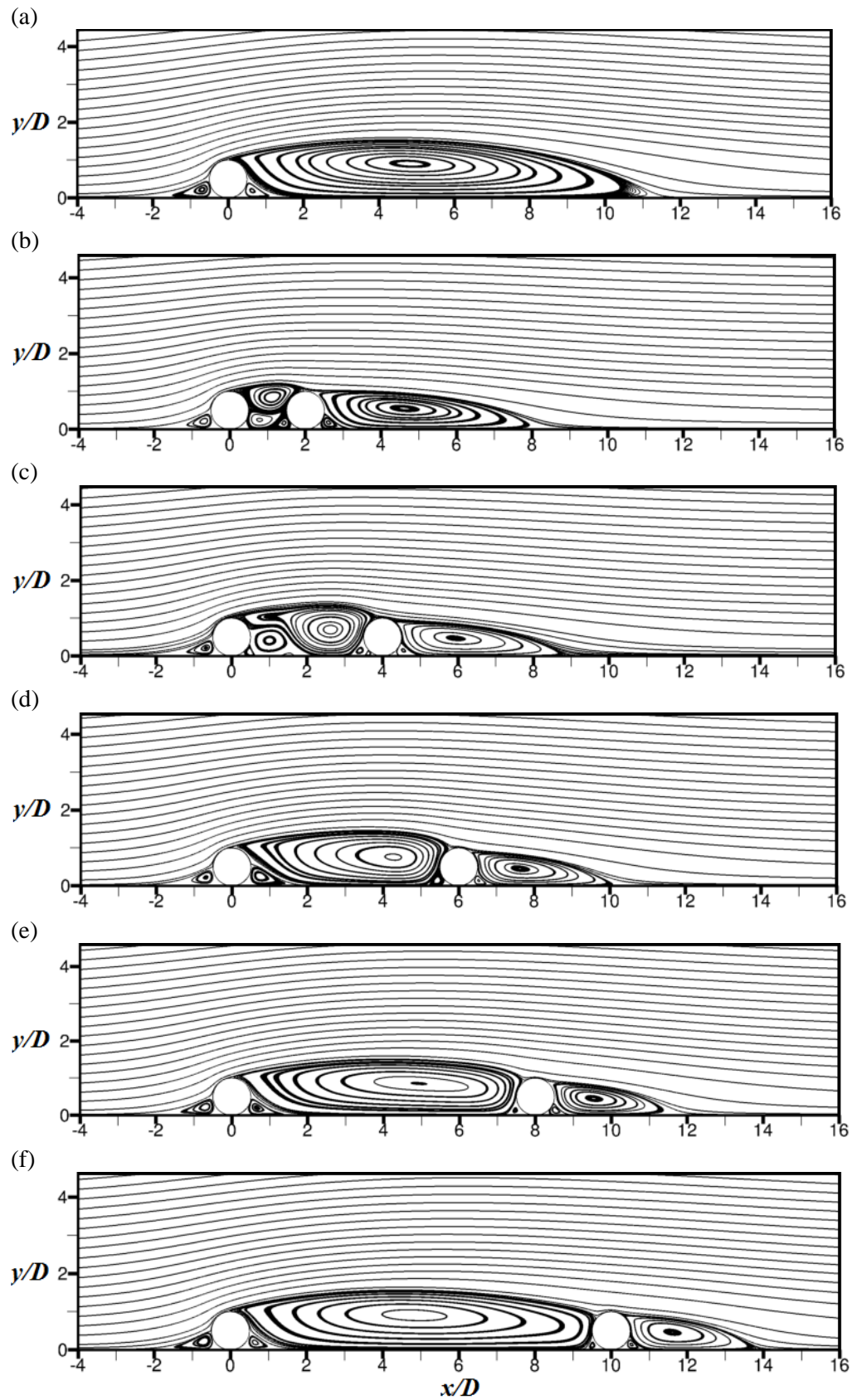


Figure 8: The streamlines of the flows: (a) to (f) Cases 3, 6, 9, 12, 15 and 18, respectively

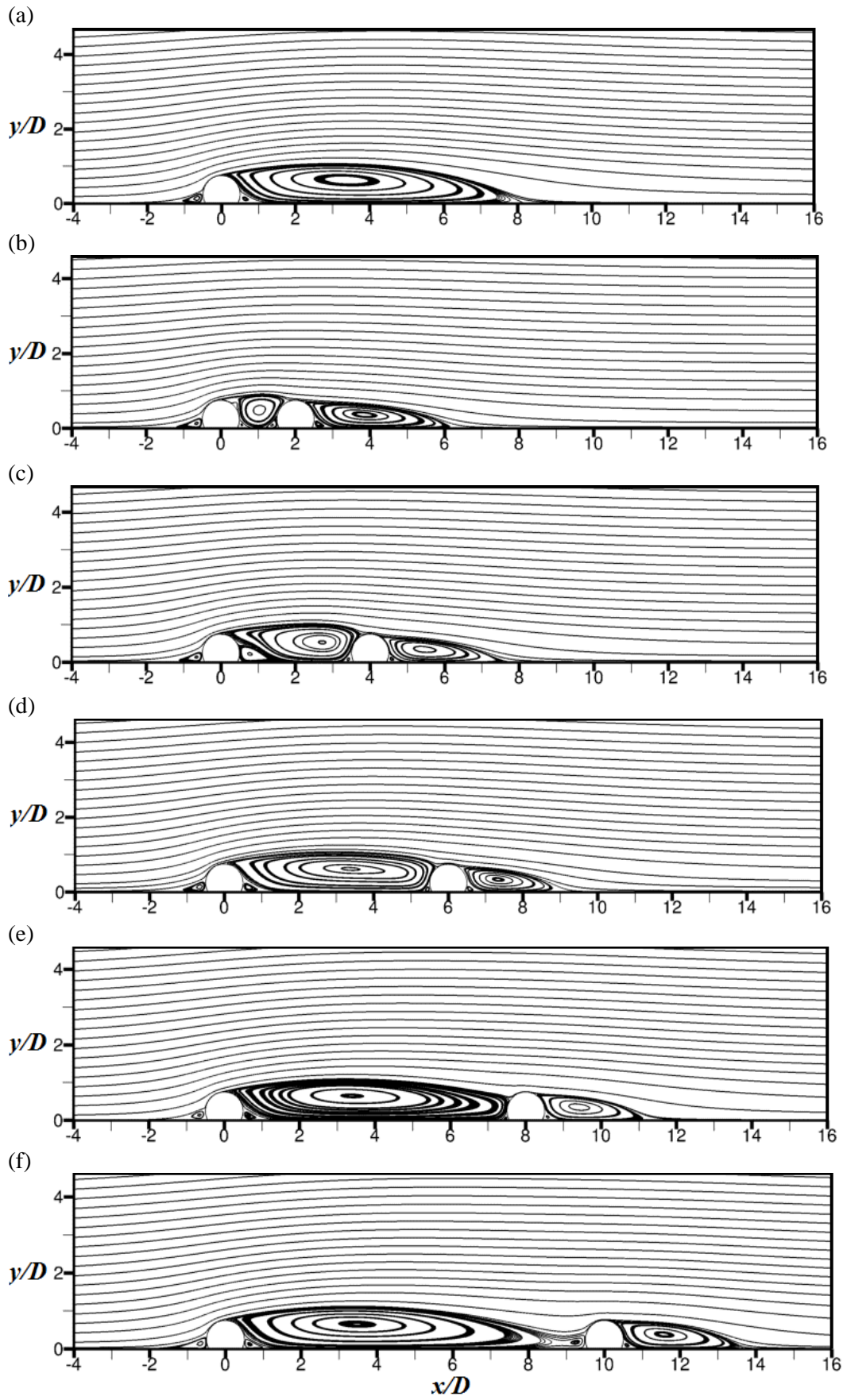


Figure 9: The streamlines of the flows: (a) to (f) Cases 21, 24, 27, 30, 33 and 36, respectively

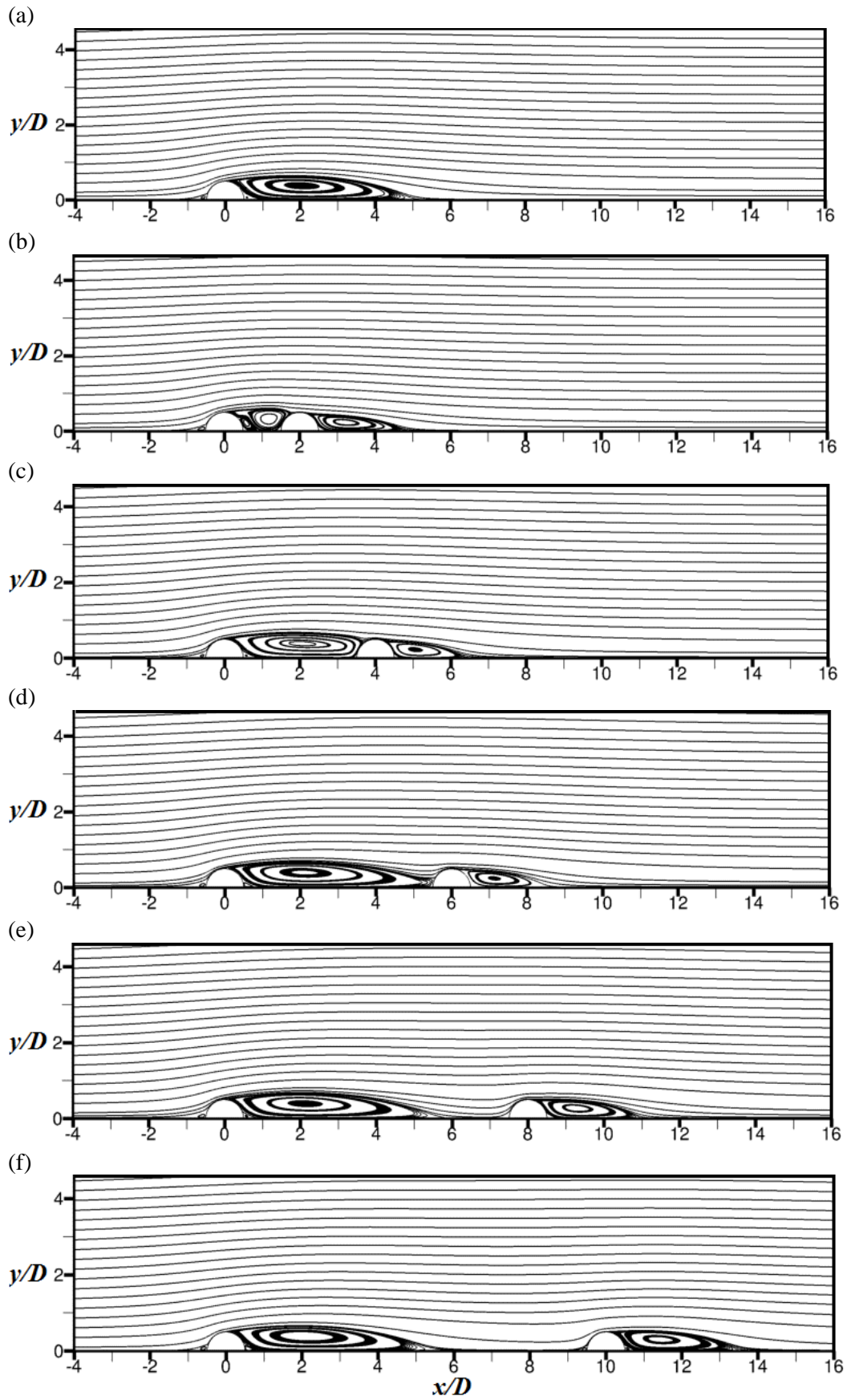


Figure 10: The streamlines of the flows: (a) to (f) Cases 39, 42, 45, 48, 51 and 54, respectively

5. Conclusion

In the present study, 2D Reynolds-Averaged Navier-Stokes with $k - \omega$ SST turbulence model flow over a single and two tandem cylinders with different burial and pitch ratios are investigated. The cylinders are subjected to a boundary layer flow with a fixed thickness of $\delta = 0.48D$ at $Re = 1.31 \times 10^4$. The convergence studies are carried out based on the hydrodynamic quantities C_D and C_L . The validation studies show that the coefficients are in good agreement with the previous published experimental and numerical results. The hydrodynamic quantities of the two cylinders in tandem with different L/D s and B/D s, as well as the pressure and the streamwise velocity contours, and the streamlines around them are discussed. The main conclusions are summarized as follows:

1. Regarding the single cylinder cases, the hydrodynamic coefficients C_D and C_L and the recirculation length behind the cylinder are all reduced with the increasing B/D .
2. With $L/D = 2$ for all B/D s, the vorticity between the cylinders is the strongest compared with that for other L/D s and the absolute value of the negative pressure region between the two cylinders are the highest, which results in the largest value of C_{D1} and the largest absolute value of the negative C_{D2} .
3. For all B/D s and L/D s, the downstream cylinder has lower absolute values of drag and lift coefficients compared to the upstream cylinder.
4. For all B/D s, there is a critical value of L/D that leads to the zero value of C_{D2} of the downstream cylinder. They are found to be: $L/D = 10$ for $B/D = 0$; $L/D \approx 7$ for $B/D = 0.25$; and $L/D = 4$ for $B/D = 0.5$. These critical values of L/D are close to the recirculation length behind the corresponding single cylinder cases. Also, the recirculation length behind the downstream cylinder is found to be minimum in these critical locations.
5. For L/D higher than the critical value, the flow over both cylinders starts to get similar to the flow over the single cylinder with the increasing L/D , and the hydrodynamic quantities of the upstream cylinder, the pressure, velocity contours and the streamlines around the two cylinders are also similar to those around the corresponding single cylinder.

References

- Aköz, M. S., Şimşek, O. & Soydan, N. G. (2019). Numerical Modeling of Interaction of Turbulent Flow with a Buried Circular Cylinder on a Plane Surface. *Teknik Dergi*, 30(6), 1-25.
- An, H., Cheng, L. & Zhao, M. (2011). Numerical simulation of a partially buried pipeline in a permeable seabed subject to combined oscillatory flow and steady current. *Ocean engineering*, 38(10), 1225-1236.
- Arie, M., Kiya, M., Tamura, H. & Kanayama, Y. (1975). Flow over rectangular cylinders immersed in a turbulent boundary layer: part 1, correlation between pressure drag and boundary-layer characteristics. *Bulletin of JSME*, 18(125), 1260-1268.
- Cokgor, S. & Avci, I. (2001). Hydrodynamic forces on partly buried tandem, twin pipelines in current. *Ocean Engineering*, 28(10), 1349-1360.
- Gao, Y. & Mi, H. R. (2009). Numerical simulations of flowfield and pressure distribution around various roofs. 5th European and African Conference on Wind Engineering, EACWE 5, Proceedings.
- Jensen, B. L., Sumer, B. M., Jensen, H. R. & Fredsoe, J. (1990). Flow around and forces on a pipeline near a scoured bed in steady current. *Journal of Offshore Mechanics and Arctic Engineering*. 112. 206-213.
- Jones, W. P. & Launder, B. (1973). The calculation of low-Reynolds-number phenomena with a two-equation model of turbulence. *International Journal of Heat and Mass Transfer*, 16(6), 1119-1130.
- Lei, C., Cheng, L. & Kavanagh, K. (1999). Re-examination of the effect of a plane boundary on force and vortex shedding of a circular cylinder. *Journal of Wind Engineering and Industrial Aerodynamics*, 80(3),263-286.
- Li, Z., Prsic, M. A., Ong, M. C. & Khoo, B. C. (2018). Large Eddy Simulations of flow around two circular cylinders in tandem in the vicinity of a plane wall at small gap ratios. *Journal of Fluids and Structures*, 76, 251-271.
- Menter, F. R. (1994). Two-equation eddy-viscosity turbulence models for engineering applications. *AIAA journal*, 32(8), 1598-1605.
- Menter, F. R., Kuntz, M. & Langtry, R. (2003). Ten years of industrial experience with the SST turbulence model. *Turbulence, heat and mass transfer*, 4(1), 625-632.
- Ong, M. C., Utnes, T., Holmedal, L. E., Myrhaug, D. & Pettersen, B. (2010). Numerical

simulation of flow around a circular cylinder close to a flat seabed at high Reynolds numbers using a $k-\epsilon$ model. *Coastal Engineering*, 57(10), 931-947.

Prsic, M. A., Ong, M. C., Pettersen, B. & Myrhaug, D. (2016). Large Eddy Simulations of flow around a circular cylinder close to a flat seabed. *Marine Structures*, 46, 127-148.

Tauqeer, M. A., Li, Z. & Ong, M. C. (2017). Numerical simulation of flow around different wall-mounted structures. *Ships and Offshore Structures*, 12(8), 1109-1116.

Wang, X. K., Zhang, J. X., Hao, Z., Zhou, B. & Tan, S. K. (2015). Influence of wall proximity on flow around two tandem circular cylinders. *Ocean Engineering*, 94, 36-50.

Wilcox, D. C. (1998). *Turbulence modeling for CFD* (Vol. 2, pp. 172-180). La Canada, CA: DCW industries.

Zhao, M., Cheng, L. & Teng, B. (2007). Numerical modeling of flow and hydrodynamic forces around a piggyback pipeline near the seabed. *Journal of waterway, port, coastal, and ocean engineering*, 133(4), 286-295.

Chapter 5

PAPER II: THREE-DIMENSIONAL NUMERICAL SIMULATIONS AND PROPER ORTHOGONAL DECOMPOSITION ANALYSIS OF FLOW OVER DIFFERENT BOTTOM-MOUNTED RIBS

A corresponding version of the draft of the paper that has been submitted to Ships and Offshore Structures journal is given in the present chapter. 3D flow over bottom-mounted square, trapezoidal and rectangular ribs using SADDLES at a Reynolds number of 1×10^6 is studied. The ribs are subjected to a boundary layer flow with thickness of $\delta = 0.73H$. Such configuration can be found in subsea covers and equipment, as well as in several other industrial equipment. It is shown that the flow over the trapezoidal rib can be considered smoother compared with the other geometries investigated, resulting in lower hydrodynamic coefficients. POD analysis of the flow behind the ribs is employed to investigate the dominant turbulent structures. This technique is performed on different planes in the streamwise and spanwise directions and it is found that the fluctuation modes tend to appear in pairs. Also, the energy is highly concentrated in the lower modes and the turbulent structures appear mainly around the shear layer of the wake flow.

Three-dimensional Numerical Simulations and Proper Orthogonal Decomposition Analysis of Flow over Different Bottom-mounted Ribs

Vinicius Serta Fraga^a, Guang Yin^{a2}, Muk Chen Ong^a

^aDepartment of Mechanical and Structural Engineering and Materials Science, University of Stavanger, Stavanger, Norway

Abstract

Turbulent flow over bottom-mounted ribs is investigated using three-dimensional (3D) Spalart-Allmaras Delayed Detached-Eddy Simulations (SADDES). The wall-mounted ribs are subjected to a boundary layer flow with a thickness of $\delta/H = 0.73$ at a Reynolds number ($Re = U_\infty H/\nu$) of 1×10^6 , where U_∞ is the free stream velocity of the boundary layer flow, H is the height of the rib and ν is the kinematic viscosity of the fluid. Mesh and time step convergence studies are conducted to determine the grid and time step resolution based on the time-averaged hydrodynamic quantities. The numerical model is validated against the experimental data reported by Liu et al. (2008). The effects of different ribs geometries (square, trapezoidal and rectangular) on the hydrodynamic quantities, such as drag and lift coefficients, and the wake flow structures are discussed. Dominant features of the flow are investigated by carrying out Proper Orthogonal Decomposition (POD) analysis of the flow velocities and pressure in the wake behind the ribs.

Keywords: bottom-mounted ribs, 3D turbulent flow, SADDES, Proper Orthogonal Decomposition

1. Introduction

Bottom-mounted rib structures are widely used in many industries, such as subsea covers to protect pipelines, heat exchangers and gas turbines. These structures are often exposed to a high Reynolds number flow. It is of great significance to investigate the hydrodynamic forces on the structures. For example, subsea structures are commonly subjected to strong current and wave, and should be kept on their installation positions. For design and optimization with safe operation, it is necessary to obtain the drag and lift coefficients on them.

² Corresponding author: guang.yin@uis.no

There are many experimental studies carried out to analyze the high Reynolds flow over surface-mounted structures over decades. Arie et al. (1975) studied the flow over wall-mounted rectangular cylinders subjected to turbulent boundary layer flow and concluded that the pressure coefficient on the structure surface is correlated with the thickness of the boundary layer. Fully developed turbulent channel flow around prismatic obstacles was investigated by Martinuzzi & Tropea (1993) and it was found that there is a nominally two-dimensional (2D) middle region in the wake about the plane of symmetry behind the structures with an aspect ratio larger than 6. Liu et al. (2008) studied the unsteady characteristics of the flow over a 2D square rib and the flapping behaviour of the separation bubble behind the rib was analysed.

Numerical simulations have also been used to study the flow over wall-mounted structures. Utnes & Ren (1995) analysed the turbulent flow around a wall-mounted cube by using Reynolds-averaged Navier-Stokes (RANS) equations with the two-equation $k - \varepsilon$ turbulence model. The results were in good agreement with the experimental data reported by Castro & Robins (1997). Hwang et al. (1999) carried out 2D simulations of turbulent flow around ribs with varying length using RANS combined with the $k - \varepsilon$ model. It was found that the length of the recirculation region behind the rib is dependent on the rib width. The recirculation length decreases linearly with the increasing height-to-width ratio of the rib cross-section. Orellano & Wengle (2000) compared Large Eddy Simulation (LES) with Direct Numerical Simulation (DNS) for turbulent flow over a wall-mounted fence. LES was able to provide satisfying results compared with the reference data of DNS while using less than 5% of the computational requirement of DNS. Schmidt & Thiele (2002) conducted Detached Eddy Simulation (DES) of high Reynolds number flow over wall-mounted cubes and compared the results with those obtained by LES and RANS simulations. It was shown that DES was capable of capturing the unsteadiness of the wake flow behind the cubes. Frederic et al. (2008) compared DES and LES by carrying out numerical simulations of flow around a wall-mounted cylinder. DES and zonal DES of high Reynolds number flow around a bottom-mounted cube were performed by Haupt et al. (2011). It was found that DES can obtain better results than RANS compared with the experimental data reported by Hoxey et al. (2002). Tauqeer et al. (2017) carried out 2D RANS simulations of flow over wall-mounted square, triangular and semi-circular structures using $k - \varepsilon$ model. The results were in good agreement with the experimental data obtained by Liu et al. (2008). Also, the highest values of drag coefficient were obtained from the square structure and the highest lift coefficient was obtained from the semi-circular structure.

After performing the numerical simulations of the flow over the ribs, it is necessary to analyze the coherent structures behind the ribs in order to understand the dominant flow structures which will benefit the engineering design of the rib geometries. In the present study, a data-

driven postprocessing technique known as Proper Orthogonal Decomposition (POD) is used to study the wake flow behind the ribs. It has been widely used to capture the temporal-spatial characteristics of large-scale coherent structures and build a low-dimensional representation of the turbulent flow fields using only a finite number of modes according to Podvin (2009) and Lehnasch et al. (2011). For flow around wall-mounted structures, Muld et al. (2012) carried out POD analysis of the turbulent flow around a high-speed train and the method showed good capacity in extracting key coherent structures of the flow. The flow over a wall-mounted square cylinder was studied using experiments by Leite et al. (2018) and POD analysis was carried out to identify coherent structures in the wake region. It was concluded that the symmetrical and anti-symmetrical vortices in the cylinder wake flow can be captured by the first four POD modes. Amor et al. (2019) employed different decomposition techniques to analyze the flow over a bottom-mounted square cylinder and the relationship between the flow scales and different modes was discussed.

The three-dimensional (3D) Spalart-Allmaras Delayed Detached-Eddy Simulations (SADDES) are carried out to investigate the flow over different bottom-mounted ribs at a high Reynolds number of 1×10^6 in the present study. The effects of different bottom-mounted ribs (square, trapezoidal and rectangular) on the flow are studied. In addition, 2D POD is employed to identify dominant coherent structures of the wake flow behind the ribs. The paper is organized as follows: the mathematical formulation and numerical methods are given in Section 2. The computational overview, the convergence studies and the validation studies are presented in Section 3. The results and discussion are presented in Section 4. Lastly, the conclusion is given in Section 5.

2. Mathematical Formulation and Numerical Methods

2.1 Mathematical formulation

The filtered Navier-Stokes equations of incompressible and viscous fluid applied in DDES simulations can be written as:

$$\frac{\partial u_i}{\partial x_i} = 0 \quad (1)$$

$$\frac{\partial u_i}{\partial t} + \frac{\partial u_i u_j}{\partial x_j} = -\frac{\partial p}{\partial x_i} + \nu \frac{\partial^2 u_i}{\partial x_j \partial x_j} - \frac{\partial \langle u'_i u'_j \rangle}{\partial x_j} \quad (2)$$

where $i, j = 1, 2, 3$ represent the streamwise, cross-stream and spanwise directions, respectively.

u_1 , u_2 , and u_3 (also denoted as u , v and w) are their corresponding resolved velocity components. The unresolved stresses $-\langle u'_i u'_j \rangle$ can be defined as:

$$-\langle u'_i u'_j \rangle = \nu_t \left(\frac{\partial u_i}{\partial x_j} + \frac{\partial u_j}{\partial x_i} \right) \quad (3)$$

The one equation Spalart-Allmaras model solves the transport equation for the turbulent eddy viscosity (ν_t) which is described as:

$$\nu_t = \tilde{\nu} f_{\nu 1} \quad f_{\nu 1} = \frac{X^3}{X^3 + C_{\nu 1}^3} \quad X = \frac{\tilde{\nu}}{\nu_t} \quad (4)$$

where $\tilde{\nu}$ is the modified turbulence viscosity and the constant $C_{\nu 1} = 7.1$. DES is a hybrid approach where RANS method is applied in the near-wall region and LES is used far away from the wall. The distance to the wall (\tilde{d}) is given as:

$$\tilde{d} = \min(d, C_{DES} \Delta) \quad (5)$$

where the minimum distance from the nearest wall is represented as d and the constant $C_{DES} = 0.65$. The length scale associated with the local grid spacing is given as Δ :

$$\Delta = \max(\Delta_x, \Delta_y, \Delta_z) \quad (6)$$

where $\Delta_x, \Delta_y, \Delta_z$ denote the dimension of the grid cell in the streamwise, cross-stream and spanwise directions, respectively.

An improved version of DES, SADDES, is used in the present study. It employs a modified DES limiter \tilde{d} given in (5) in order to prevent grid-induced separation (Spalart et al. 2006):

$$\tilde{d} = d - f_d \max(0, d - C_{DES} \Delta) \quad (7)$$

2.2 Numerical methods

The open source Computational Fluid Dynamics (CFD) code OpenFOAM v2.4 is used in the present study. The code is a customized C++ engine with noticeable application in CFD. Pressure-Implicit with Splitting of Operators (PISO) algorithm is used. The second order schemes for gradient and divergence are Gauss linear; for Laplacian and interpolation, Gauss linear corrected and linear schemes are employed, respectively. The time integration is conducted by using the second order Crank–Nicolson method.

3. Computational Overview, Convergence and Validation Studies

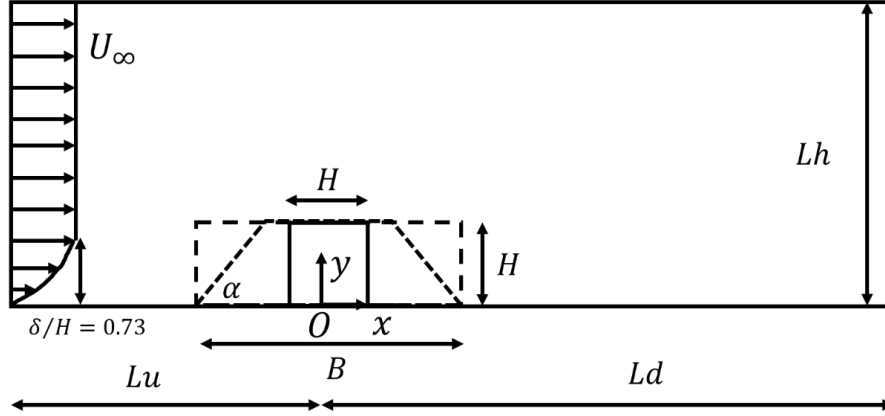
3.1 Computational overview

The computational domain used in this study is presented in Figure 1 (a) and (b) and the height of the rib is denoted as H . Three different cross-section geometries are studied: square (with a bottom edge length of $B = H$), trapezoidal and rectangular. A bottom edge length of $B = 4H$ is used for the trapezoidal and the rectangular ribs. The slope angle of the two sides of the trapezoidal rib is $\alpha = 45^\circ$. The distance between the inlet and the center of the rib bottom is $Lu = 11.5H$ and the distance between the center of the rib and the outlet is $Ld = 40.5H$. The height of the computational domain is $Lh = 20H$. According to Ong et al. (2010), a domain with $Lu = 10H$, $Ld = 20H$ and $Lh = 10H$ is able to suppress the far-field effects on the structures. Therefore, the sizes of the XY domain in the present study can be considered sufficiently large. The spanwise length is $Lz = 6H$, which is larger than that of $4H$ used in Prsic et al. (2019) and Tian et al. (2014).

The boundary conditions are shown in Figure 1. The following boundary conditions are applied for all cases in this study:

- At the inlet, a log profile for the fully developed boundary layer flow is used for the streamwise velocity, which is obtained by curve fitting of the experimental boundary layer profile reported by Arie et al. (1975). The vertical and spanwise velocities are set to zero. A boundary layer thickness of $\delta/H = 0.73$ is employed, which is the same as that in the experiments carried out by Arie et al. (1975). A zero normal gradient is applied for the pressure at the inlet.
- At the top boundary, the pressure and velocities are prescribed as zero normal gradient.
- At the outlet, the velocities are prescribed as zero normal gradient and the pressure is set to be zero.
- At the front and back boundary, periodic boundary conditions are used for all the quantities.
- On the bottom wall and the surfaces of the structures, no-slip conditions are applied for the velocities and the pressure is set as zero normal gradient. The flow over the surfaces of the structures can be considered as fully developed turbulent. Therefore, a wall function based on the Spalding's law of the wall (Spalding 1961) is used in the near-wall region.

(a)



(b)

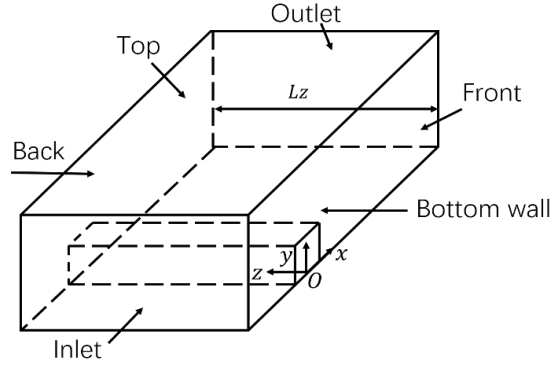


Figure 1: Computational domain and boundary conditions: (a) 2D XY-plane and (b) 3D view

3.2 Convergence studies

The mesh and time step convergence studies have been carried out. The results for each bottom-mounted rib are presented in Table 1. Two hydrodynamic quantities are analysed in this study: the time-averaged drag coefficient ($\overline{C_D}$) in the streamwise direction and the time-averaged lift coefficient ($\overline{C_L}$) in the cross-stream direction, which are given by:

$$\overline{C_D} = \frac{\overline{F_X}}{\frac{1}{2}\rho U_\infty^2 A_H} \quad \text{and} \quad \overline{C_L} = \frac{\overline{F_Y}}{\frac{1}{2}\rho U_\infty^2 A_V} \quad (8)$$

where $\overline{F_X}$ is the time-averaged force acting on the rib surface in the streamwise direction while $\overline{F_Y}$ is the time-averaged force acting on the rib surface in the cross-stream direction, ρ is the density of the fluid, A_V is the vertical projected area and A_H is the horizontal projected area of the ribs.

Table 1: Results for the bottom-mounted ribs based on the mesh elements and the time step

Case	No. of cells	Grids in Z direction	Δt	$\overline{C_D}$	$\overline{C_L}$	L_w	
Square rib	1	1275219	33	0.002	1.116	0.567	14.168
	2	1652970	33	0.002	1.121	0.572	13.626
	3	2140512	33	0.002	1.133	0.581	12.907
	4	2140512	33	0.001	1.132	0.580	12.907
	5	2140512	33	0.003	1.131	0.579	12.907
	6	3113472	48	0.002	1.133	0.581	13.172
Trapezoidal rib	7	1275219	33	0.002	0.806	0.261	13.702
	8	1652970	33	0.002	0.825	0.272	12.400
	9	2140512	33	0.002	0.844	0.287	10.195
Rectangular rib	10	1275219	33	0.002	0.961	0.490	18.213
	11	1652970	33	0.002	0.985	0.499	15.812
	12	2140512	33	0.002	1.006	0.527	11.755

For the XY-plane grid resolution study, three meshes with the same grid in the spanwise direction are used with an increment of 30% in the total number of elements between different cases for each rib: the square rib (Cases 1 to 3), the trapezoidal rib (Cases 7 to 9) and the rectangular rib (Cases 10 to 12). The results for $\overline{C_D}$ and $\overline{C_L}$ show good convergence for the square rib with relative differences around 1% between cases. Also, convergence for both trapezoidal and rectangular ribs has also been achieved, with the maximum relative differences of $\overline{C_D}$ being less than 3% and the maximum relative difference around 5% of $\overline{C_L}$ between cases. In addition, Cases 4 and 5 are simulated to show the dependence of the results on the time step resolution for the square cases with the same grid number as Case 3, which indicates that the relative differences of $\overline{C_D}$ and $\overline{C_L}$ are around 1% between cases. Finally, Case 6 is simulated with an increasing grid number in the spanwise direction and the relative differences against Case 3 are lower than 0.1% for $\overline{C_D}$ and $\overline{C_L}$, which shows that the grid number of 33 in the spanwise direction is enough. Furthermore, the time- and spanwise-averaged streamwise velocity and pressure at $y/H = 0.004$, which is close to the first layer above the bottom along the streamwise direction for the square rib (Cases 1 to 6), are shown in Figure 2. Both of the two profiles show good convergence between the different cases with similar recirculation lengths (L_w) as shown in Figure 2 (a). Likewise, a good agreement between Cases 1 to 6 for the pressure distribution is also displayed in Figure 2 (b).

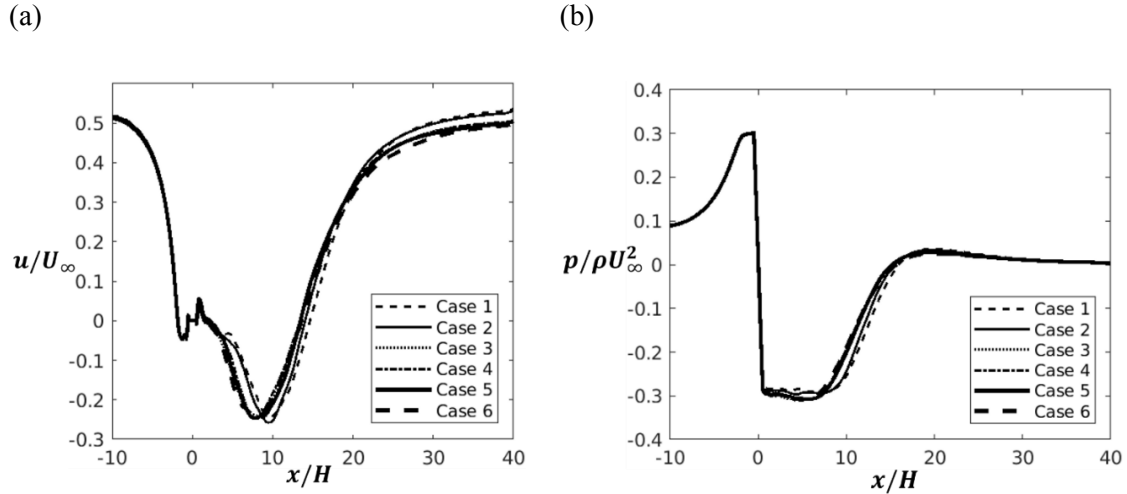


Figure 2: Profiles of the time- and spanwise-averaged (a) streamwise velocity and (b) pressure at $y/H = 0.004$ for Cases 1 to 6

Therefore, based on these results, it can be concluded that a satisfactory grid and time step resolution have been achieved in Cases 3, 9 and 12 for the square rib, the trapezoidal rib and the rectangular rib, respectively, and the results for the grid and the time step of these cases are analysed in the following sections. An example of the mesh is displayed in Figure 3 which shows the XY-plane of the converged Case 3

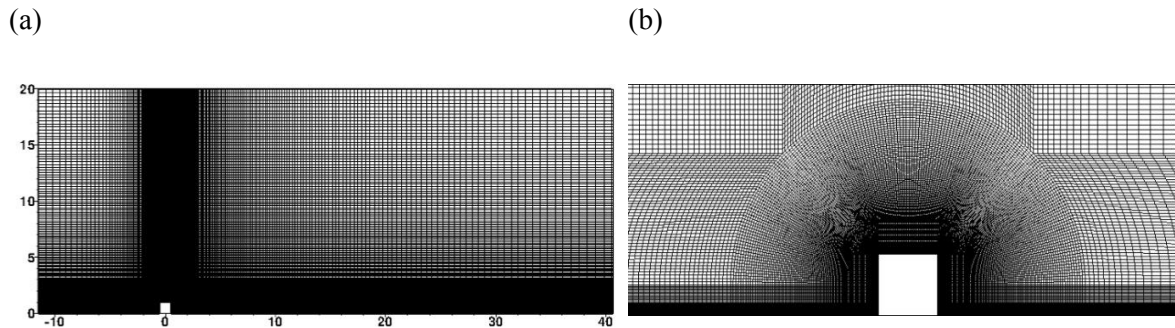


Figure 3: Computational mesh of the square rib (Case 3): (a) full XY-plane domain and (b) closer view around the rib

3.3 Validation studies

In order to validate the present SADDLES numerical model at a high Reynolds number, the converged results of the flow over the square rib (Case 3) are compared with the experimental data reported by Liu et al. (2008). The time- and spanwise-averaged streamwise velocity profiles at different locations of the present results are compared with those of the experiments in Figure 4. It can be seen that the velocity profiles are overall in good agreement with the

experimental data. The streamwise velocity profiles of the present numerical simulation display great similarity with the experimental data upstream and on the top of the square rib, while in the wake region behind the rib there are slight discrepancies between the present results and the experimental data. However, the negative parts of the velocity profiles are well captured. The minor differences may be due to the difference of the Reynolds number between the experiment done by Liu et al. (2008) and the present numerical simulation.

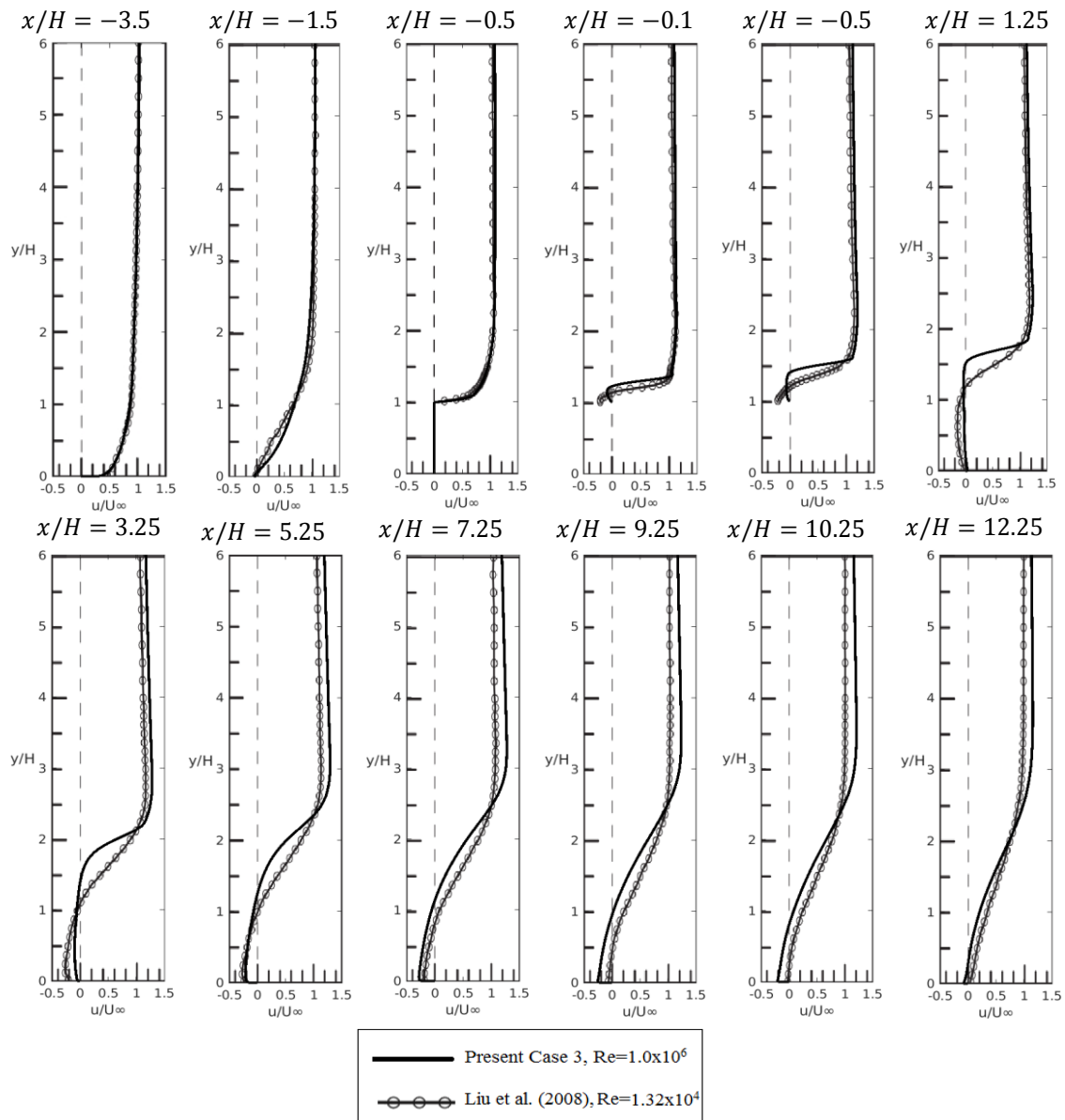


Figure 4: Time-averaged streamwise velocities of Case 3 compared with the experimental data reported by Liu et al. (2008)

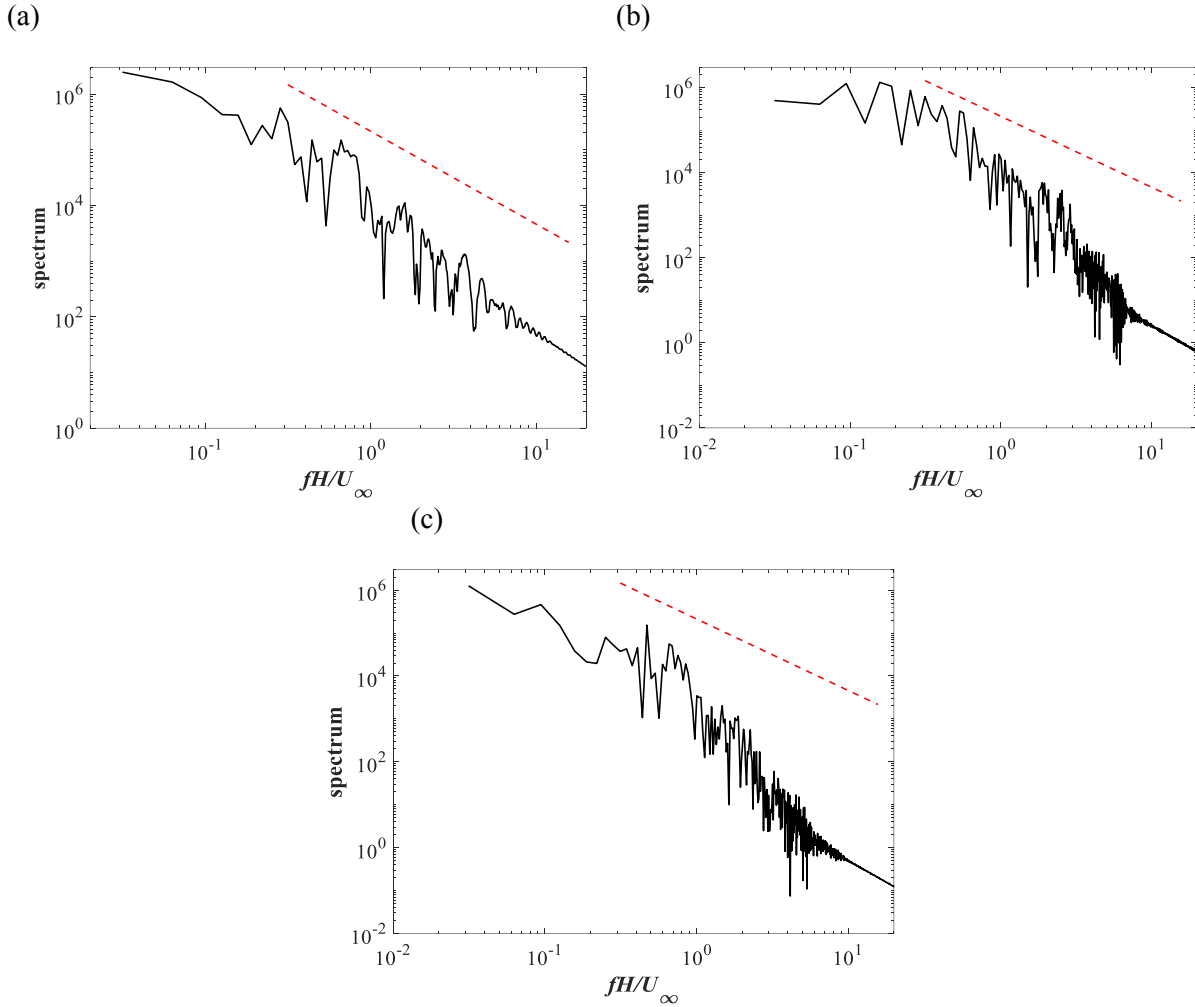


Figure 5: Power spectra of the velocity fluctuations at $y/H = 0.5$ with a distance of $0.5H$ to the back face of the ribs for (a) square, (b) trapezoidal and (d) rectangular ribs. The red lines represent the $-5/3$ law

In addition, the spectra of the resolved streamwise velocity fluctuations obtained at $y/H = 0.5$ with a distance of $0.5H$ to the back face of the three different ribs are displayed in Figure 5. It is shown that the three spectra are observed to be close to the $-5/3$ slope in the inertial range, which indicates that the turbulence spectrum can be properly captured by the current simulations.

4. Results and Discussion

4.1 Hydrodynamic forces and flow field

The time histories of the hydrodynamic quantities C_D and C_L of the converged cases (Cases 3, 9 and 12) of the three ribs are shown in Figure 6 together with the phase-space plots of the two

force coefficients. It can be seen that there exists unsteadiness in the time histories of the force coefficients which has also been reported in Tian et al. (2016) and Wu et al. (2019). The force coefficients of the trapezoidal rib show the weakest unsteadiness and the rectangular rib displays the strongest unsteadiness. Approximate linear correlations between the envelopes of C_D and C_L are observed.

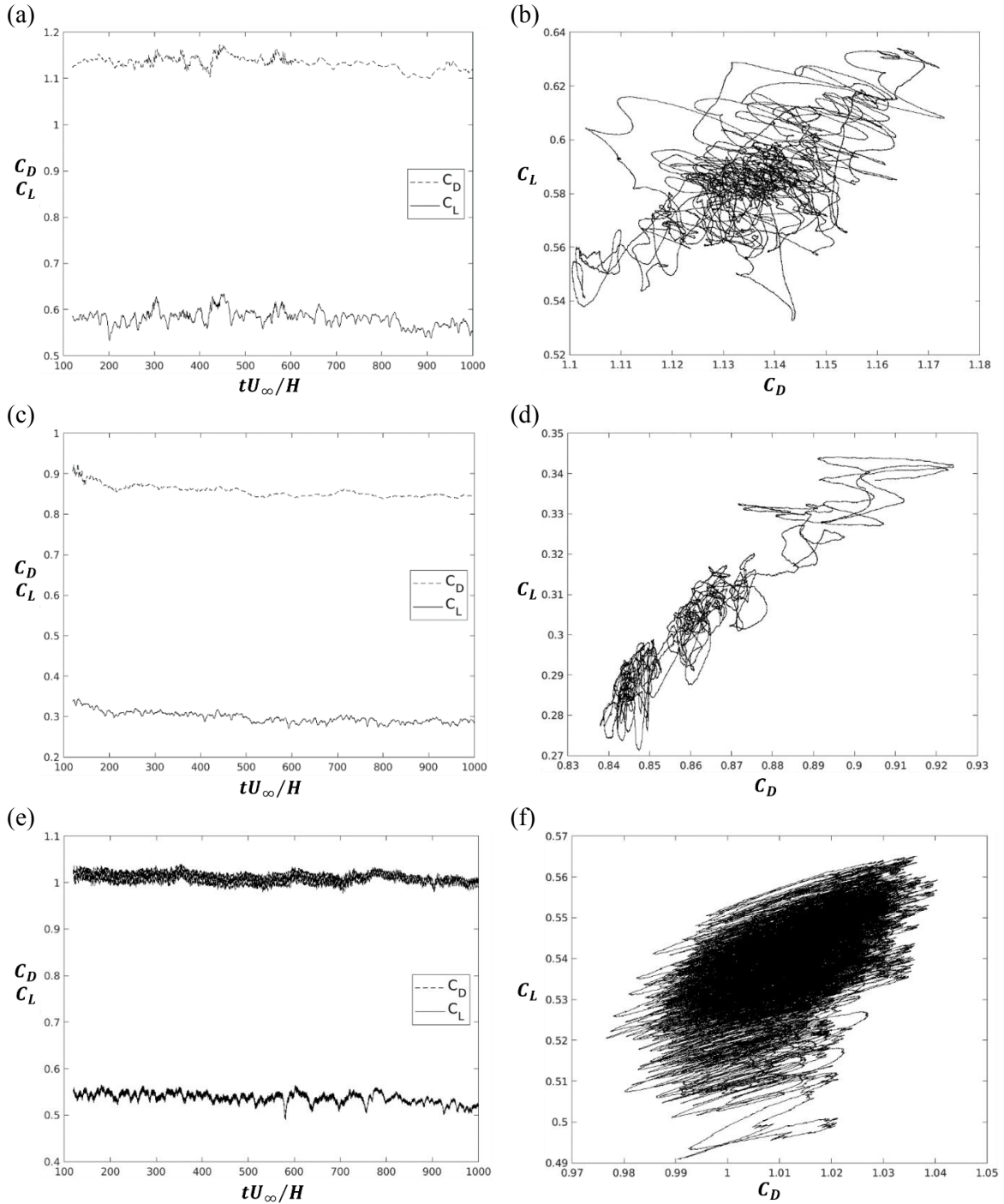


Figure 6: Time histories of C_D , C_L for (a) the square rib of Case 3; (c) the trapezoidal rib of Case 9 and (e) the rectangular rib of Case 12 and phase-space plots of C_D , C_L for (b) the square rib; (d) the trapezoidal rib and (f) the rectangular rib

The streamlines of the time- and spanwise-averaged flows are shown in Figure 7. For the three ribs, a large recirculation motion is observed behind the ribs. The recirculation motion is the longest for the square rib among the three ribs. For the square and rectangular ribs, there also exist two small recirculation motions in front of the ribs and in the corner of the back face of the ribs. The first one is caused by the downward flow to the bottom wall when the flow hits the front face of the rib, while the second one has similar behaviour when the flow hits the back face of the rib. Due to the inclination, the flow is more attached to the trapezoidal rib and the two small recirculation motions disappear.

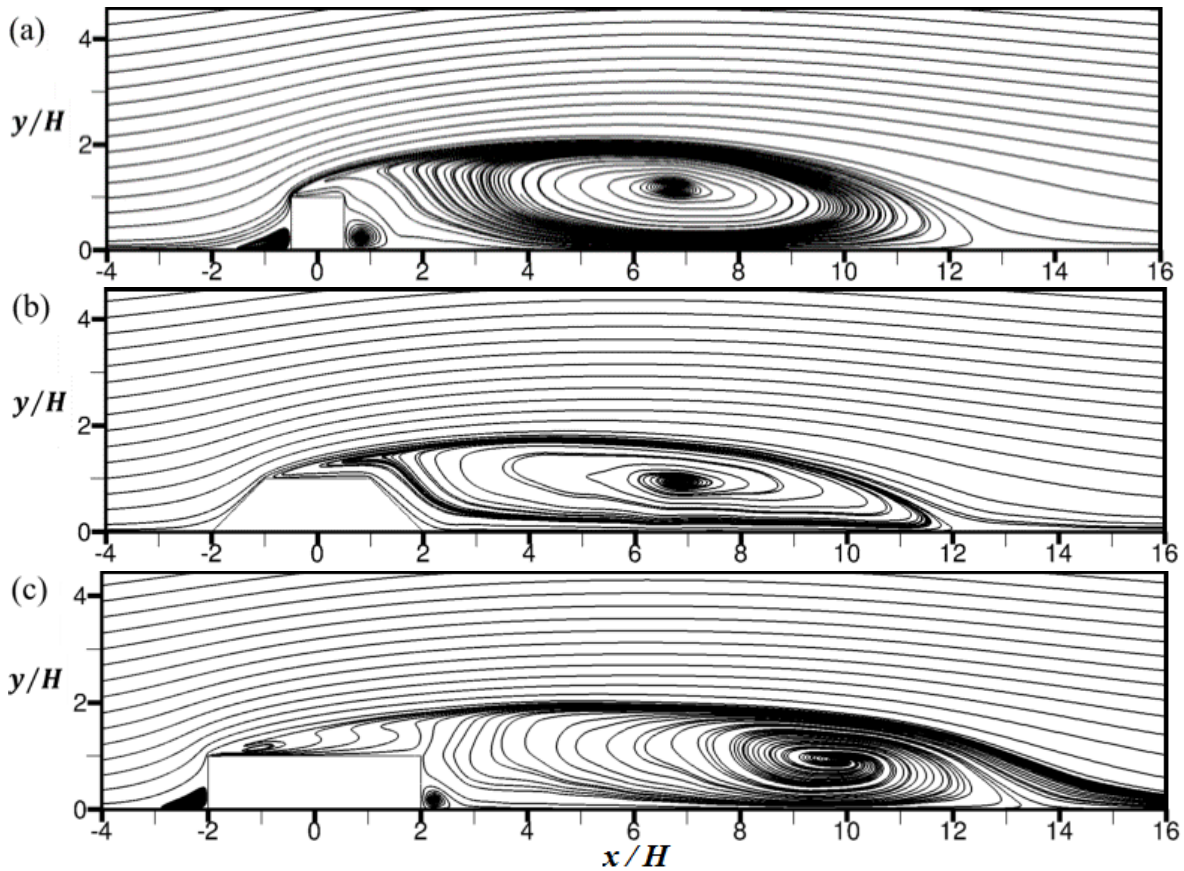


Figure 7: The streamlines of the time- and spanwise-averaged flows for (a) the square rib of Case 3; (b) the trapezoidal rib of Case 9; (c) the rectangular rib of Case 12

The three-dimensional instantaneous vortex structures identified by the Q criterion proposed by Hunt et al. (1988) for the three ribs are shown at $tU_\infty/H = 1000$ in Figure 8. The Q is given by:

$$Q = \frac{1}{2}(\|\boldsymbol{\Omega}\|^2 - \|\boldsymbol{S}\|^2) \quad (9)$$

where $\boldsymbol{\Omega}$ is the vorticity tensor and \boldsymbol{S} is the rate of strain tensor. It can be seen that shear layers stem from the leading edges of the ribs where the flows separate and roll up in to small-scale streamwise vortices further downstream. It is observed that the complexity of the vortex

structures is reduced for the rectangular and the trapezoidal ribs compared with the square rib. The vorticities behind the rectangular and the trapezoidal ribs are lower than that behind the square rib, which results in a reduced pressure difference between the front and back faces of the ribs and thus leads to lower drag coefficients for the two ribs than that of the square rib as shown in Figure 6. For the trapezoidal rib, as the flow is more attached to the rib surfaces, the small-scale vortex structures move further from the back face of the rib compared with the other ribs. For the rectangular rib, the shear layer on the top of the rib undergoes instability which may result in the strong unsteadiness of the hydrodynamic quantities as shown in Figure 6 (e, f).

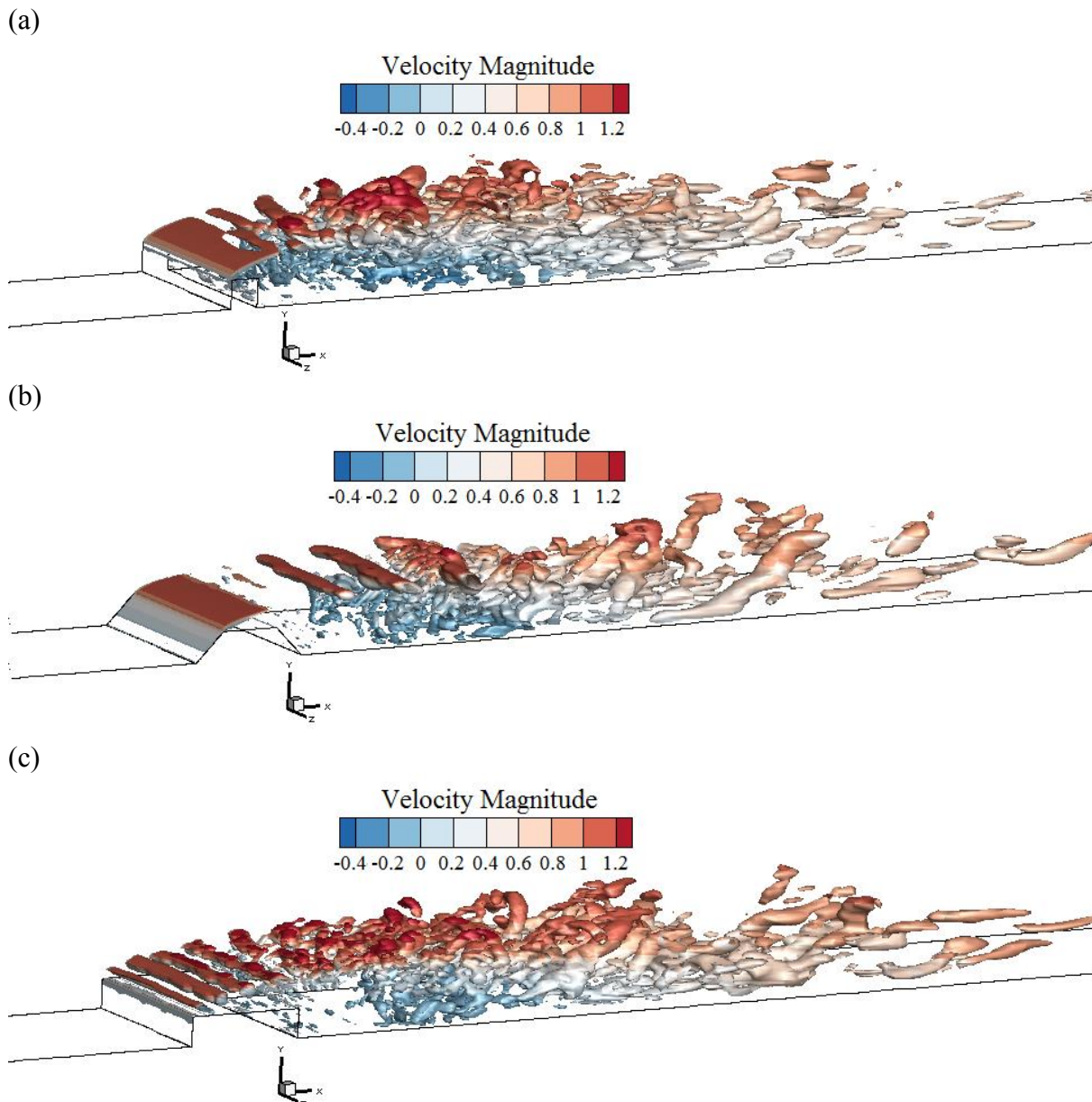


Figure 8: Instantaneous iso-surface of $Q = 0.25$ at $tU_{\infty}/H = 1000$ for (a) the square rib of Case 3; (b) the trapezoidal rib of Case 9; (c) the rectangular rib of Case 12

4.2 Proper orthogonal decomposition analysis

In order to analyze the complex flow structures behind the ribs, Proper Orthogonal Decomposition is used to extract the energy containing structures in the wake region. This technique was proposed by Lumley (1967) to analyze the turbulent coherent structures. This method can also be applied to any scalar or vector quantities. In fluid mechanics, POD attempts to decompose a time-dependent flow variable $\mathbf{q}(\boldsymbol{\chi}, t)$ (where $\boldsymbol{\chi}$ denote the spatial coordinates and t denotes the time, respectively) into a series of spatial modes $\boldsymbol{\phi}_j(\boldsymbol{\chi})$ and their corresponding temporal coefficients $a_j(t)$ as:

$$\mathbf{q}(\boldsymbol{\chi}, t) = \sum_j a_j(t) \boldsymbol{\phi}_j(\boldsymbol{\chi}) \quad (10)$$

The POD modes $\boldsymbol{\phi}_j(\boldsymbol{\chi})$ are orthogonal satisfying $\langle \boldsymbol{\phi}_i(\boldsymbol{\chi}), \boldsymbol{\phi}_j(\boldsymbol{\chi}) \rangle = \delta_{ij}$ and can be obtained by eigenvalue decomposition of the spatial or temporal correlation matrix of the flow quantities as proposed by Lumley (1967), Sirovich (1987) and Meyer et al. (2007). As discussed in Taira et al. (2017), the modes can also be obtained by Singular Value Decomposition (SVD).

In the present study, POD analysis of the velocity components and the pressure at 2D planes is carried out. The algorithm of the POD method is given as follows. The flow field data from the simulations is sampled and arranged in a matrix:

$$\mathbf{M} = \mathbf{V}_1^n = [\mathbf{v}_1, \mathbf{v}_2, \dots, \mathbf{v}_n] \quad (11)$$

where \mathbf{v}_i ($i = 1, 2, 3 \dots n$) are column vectors containing the velocity components at each grid node in a 2D plane at the time step of t_i ($i = 1, 2, 3 \dots n$) separated by the same time step Δt_{POD} . The procedure is similarly applied for the pressure:

$$\mathbf{M} = \mathbf{P}_1^n = [\mathbf{p}_1, \mathbf{p}_2, \dots, \mathbf{p}_n] \quad (12)$$

The POD modes are obtained by applying SVD on the snapshot's matrix \mathbf{M} :

$$\mathbf{M} = \mathbf{U} \boldsymbol{\Sigma} \mathbf{V}^T \quad (13)$$

where \mathbf{U} and \mathbf{V} are the left and the right singular vectors of \mathbf{M} , respectively. The column vectors of \mathbf{U} are the POD modes $\boldsymbol{\phi}_j$ and the column vectors of \mathbf{V} denote the temporal coefficients $a_j(t)$ of the corresponding modes. They are both orthogonal matrices satisfying:

$$\mathbf{V}^T \mathbf{V} = \mathbf{I} \quad (14)$$

$$\mathbf{U}^T \mathbf{U} = \mathbf{I} \quad (15)$$

The diagonal matrix $\mathbf{\Sigma} = \mathbf{diag}(\lambda_1, \lambda_2, \lambda_3 \dots \lambda_n)$ contains the singular values of the matrix \mathbf{M} and each diagonal value represents the energy carried by each POD mode. They are ordered as:

$$\lambda_1 > \lambda_2 > \lambda_3 > \dots > \lambda_n > 0 \quad (16)$$

In the present study, an economy-size SVD is performed by using the corresponding internal function in MATLAB, which means that for the rectangular matrix $\mathbf{M}_{m \times n}$ with $m > n$, only the first n columns of the left singular vectors are calculated and $\mathbf{\Sigma}$ is a $n \times n$ matrix.

4.2.1 Proper orthogonal decomposition analysis along the streamwise direction

In this section, POD analysis is made on a XY-plane in the middle of the spanwise direction at $z = 3H$. The total number of spatial points of each snapshot is $m = 129728$ (Figure 9). According to Yang et al. (2017), the results obtained from POD analysis should be independent on the number of snapshots and the time step Δt_{POD} between the sampling flow fields snapshots. Therefore, a convergence study has to be done in order to determine the appropriate number of snapshots and the time step (Δt_{POD}).

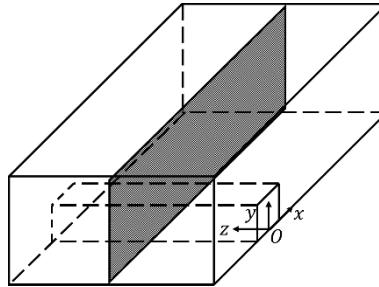


Figure 9: Representation of the snapshots assembling along the streamwise direction

Due to the orthogonality of the POD modes, Muld et al. (2012a) proposed a method for the convergence study based on the orthogonality of the POD modes. If the scalar product between the leading POD modes defined as $\varepsilon_{ortho} = \langle \phi_{j,1}, \phi_{j,2} \rangle$ (1,2 denote different snapshots samples with different snapshots numbers and j denotes the number of the modes) obtained using different numbers of snapshots equals 1, the POD modes have been fully converged. A similar test can also be conducted based on different time steps Δt_{POD} between snapshots. Figures 10 and 11 show the mean value of ε_{ortho} of the ten most energetic velocities and pressure modes of all geometries. The value of ε_{ortho} is obtained by comparing the POD modes acquired from

different numbers of snapshots with the POD modes obtained based on the number of 800 snapshots, which is used as the reference set of modes. This procedure is the same as done in Muld et al. (2012a, b). A similar convergence test is done by calculating ε_{ortho} comparing the POD modes based on different number of snapshots S_{nPOD} and time step Δt_{POD} . The results given in Figures 10 (a) and 11 (a) are based on a reference snapshot of $S_{nPOD} = 800$ with equal sampling time. The results shown in Figures 10 (b) and 11 (b) are based on a reference time step of $\Delta t_{POD} = 0.5H/U_\infty$ and sampling time of $800H/U_\infty$. It can be seen that an acceptable convergence can be achieved when the number of snapshots is higher than 600 and Δt_{POD} is lower than $1H/U_\infty$. A similar behaviour of the value ε_{ortho} is also reported in Muld et al. (2012a, b). Thus, the POD analyses of the present study are carried out using 1600 snapshots with $\Delta t_{POD} = 0.5H/U_\infty$.

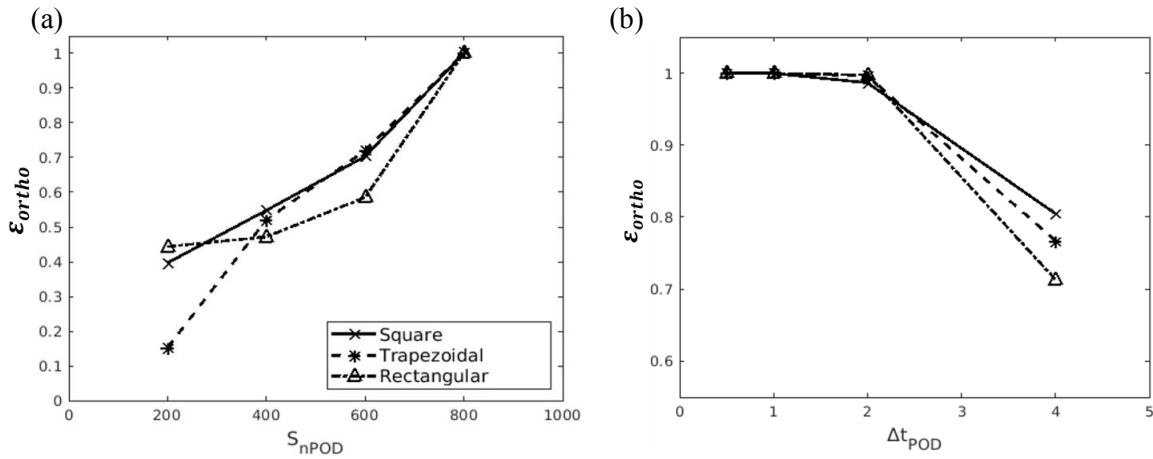


Figure 10: The mean value of ε_{ortho} of the ten most energetic modes between different sets of snapshots of the velocity modes based on: (a) number of snapshots; (b) Δt_{POD} of the velocity modes

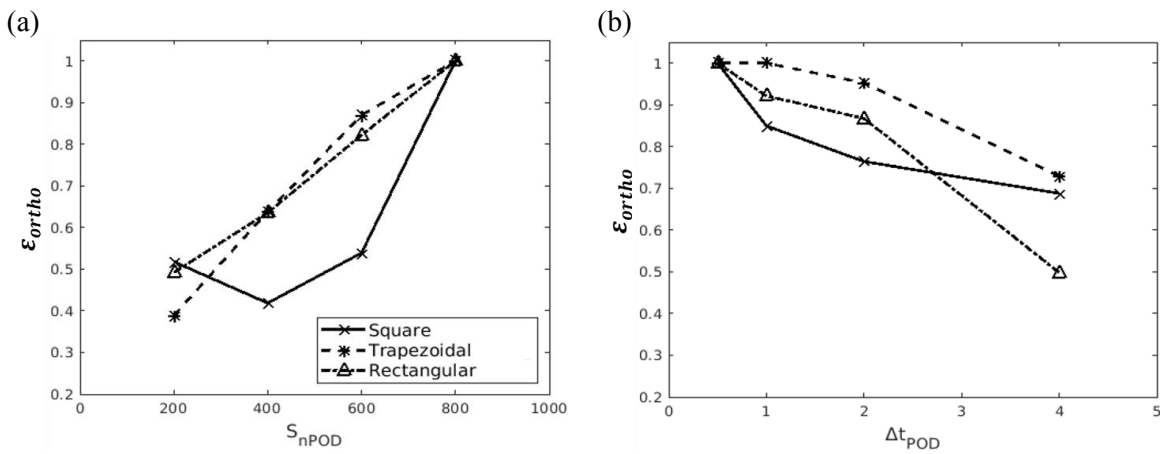
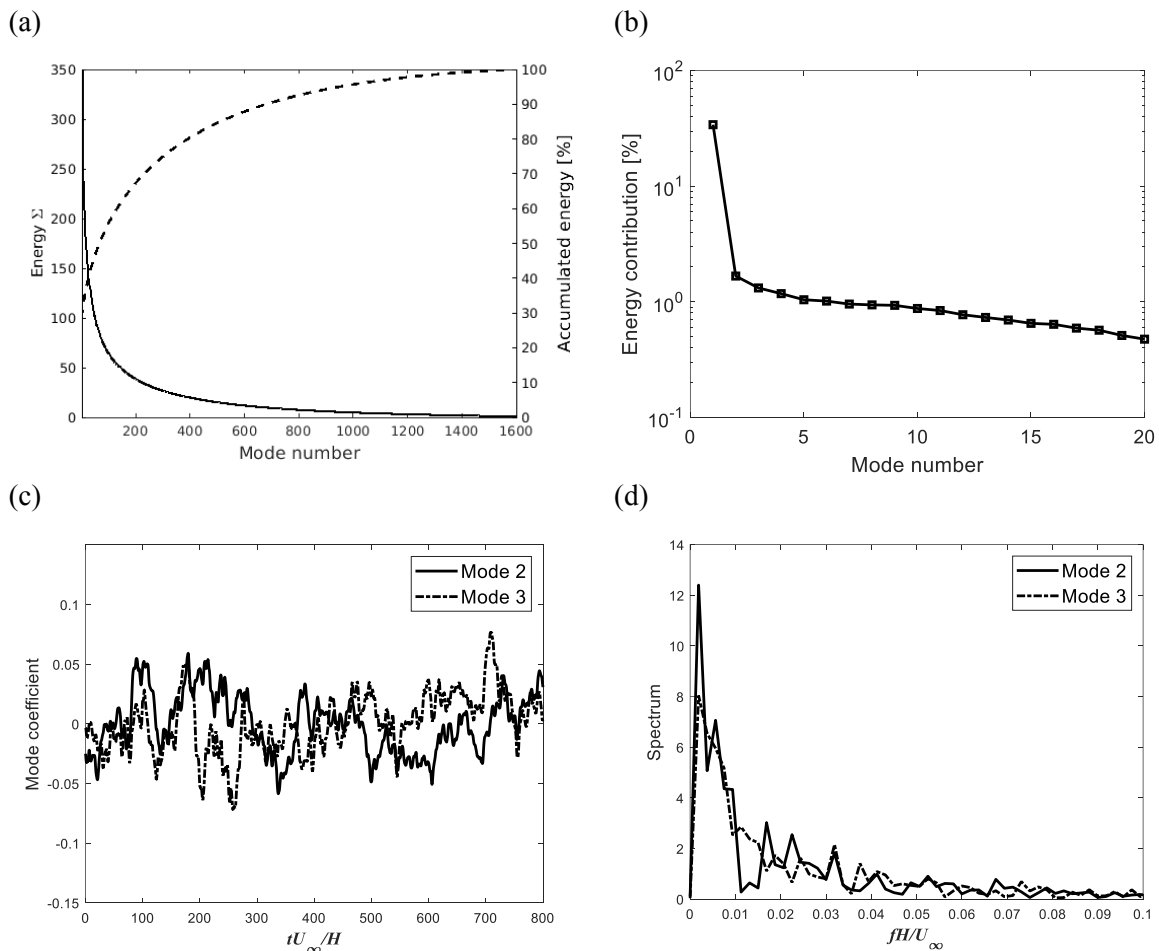


Figure 11: The mean value of ε_{ortho} of the ten most energetic modes between different sets of snapshots of the pressure modes based on: (a) number of snapshots; (b) Δt_{POD} of the velocity modes

4.2.1.1 The square rib

The energy distribution of all the velocity POD modes of the square rib is shown in Figure 12 (a). It shows an exponential decay of the energy from the lower modes to the higher modes. The energy contribution of the first 20 POD modes is presented in Figure 12 (b). The first POD mode corresponds to the mean flow containing almost 30% of the total energy of the velocity field in the 2D plane, while the following modes contribute less than 1% to the total energy. Figure 12 (c), (e) show the temporal coefficients of Modes 2, 3 and Modes 4, 5. For Modes 2 and 3, a wave-like periodic behaviour is observed and the frequency spectrum of their temporal coefficients given in Figure 12 (d) show similar peaks within the low frequency range. This indicates a large-scale traveling wave structure as reported in Semeraro et al. (2012) and Yang et al. (2017). The frequency spectra of mode temporal coefficients of Modes 4 and 5 are displayed in Figure 12 (f) and a wide spectra distribution is observed, indicating a chaotic behaviour of Modes 4 and 5.



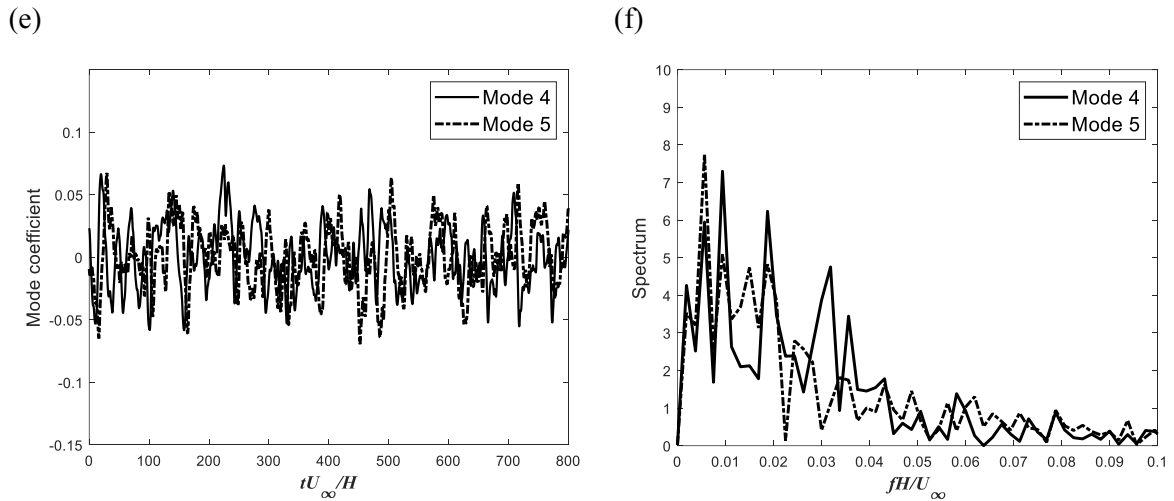


Figure 12: Modal decomposition of the velocities for the square rib: (a) energy of modes; (b) energy contribution of the 20 leading energetic modes; (c) temporal coefficients of Modes 2 and 3 and (d) frequency spectra of Modes 2 and 3; (e) temporal coefficients of Modes 4 and 5 and (f) frequency spectra of Modes 4 and 5

Contours of the POD velocity modes of the square rib are shown in Figure 13: (a) and (c) show the most energetic pair of the fluctuation modes (Modes 2 and 3), while (e) and (g) show the following pair (Modes 4 and 5) of the streamwise velocity. The pairs have similar level of energy as shown in Figure 12 (b) indicating the downstream convection of the modes. The first pair of POD modes shows a strong shear layer around the edge of the wake flow, while the second pair shows positive and negative velocity regions with a shorter streamwise length scale compared with the first pair. Figure 13 (b, d, f, h) display the cross-stream velocity contours of Modes 2, 3 and Modes 4, 5. The positive and negative pairs are clearly seen and shorter length scale regions are also observed in the higher modes of Modes 4, 5 compared with those of Modes 2, 3.

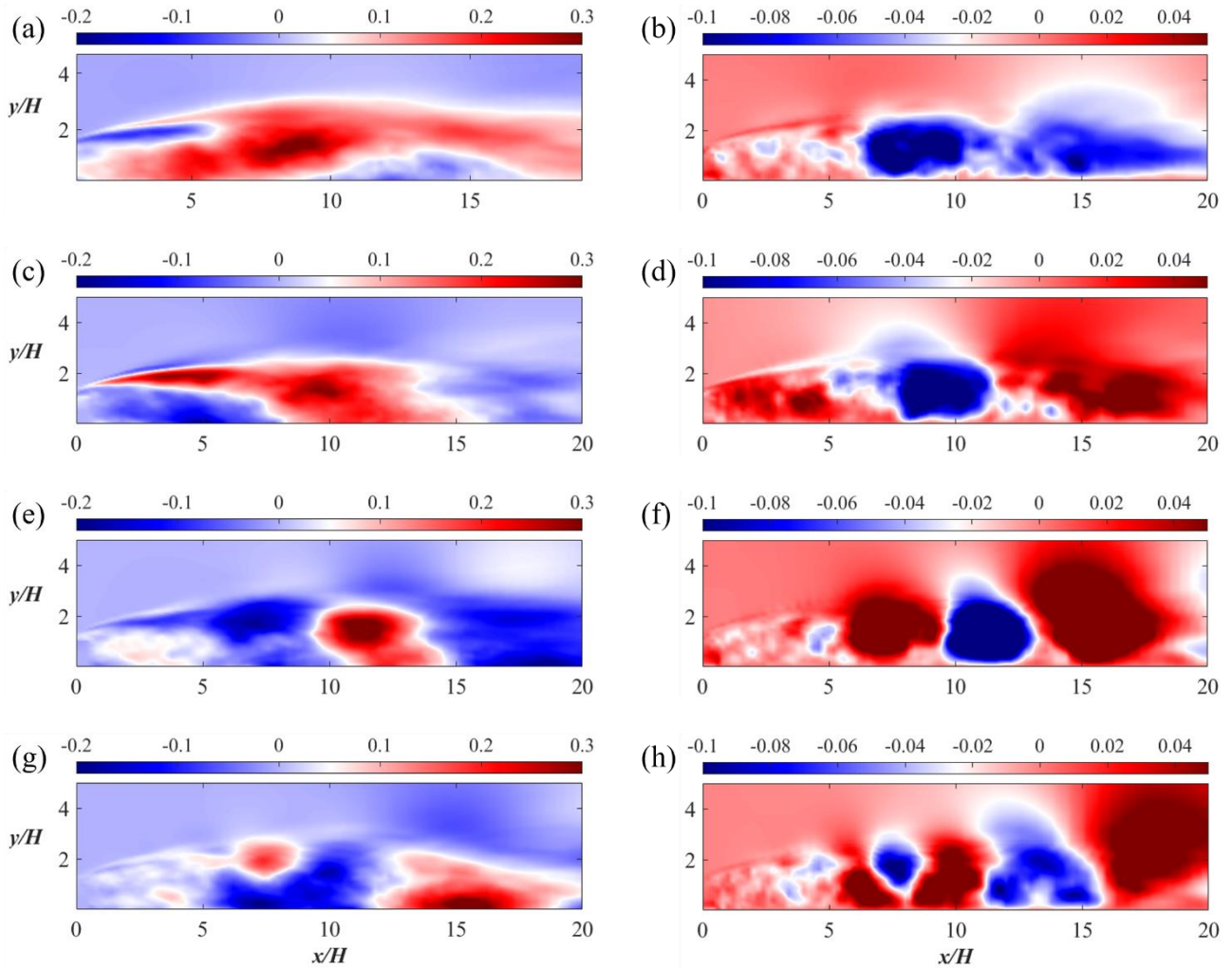


Figure 13: POD modes of the streamwise (a, c, e, g) and cross-stream (b, d, f, h) velocities for the square rib: (a, b) POD Mode 2; (c, d) POD Mode 3; (e, f) POD Mode 4 and (g, h) POD Mode 5

Figure 14 (a) shows the L_2 -norm distribution of all pressure POD modes for the square rib. The L_2 -norm decays exponentially from the first modes to the following modes faster than the energy contained in the velocity modes as shown in Figure 12 (a). The contribution of the most energetic modes is given in Figure 14 (b). The first POD mode corresponds to the mean pressure and contains almost 35% of the total energy while the following fluctuation POD modes are much less energetic, with less than 2% of the total energy of the pressure field. The time histories of the coefficients of Modes 2 and 3 are shown in Figure 14 (c) with the frequency spectra of the two modes in Figure 14 (d). Different spectra of the two modes are shown, which indicates that the two modes cannot form a mode pair. A broadband distribution of the spectra is also observed within the low frequency range.

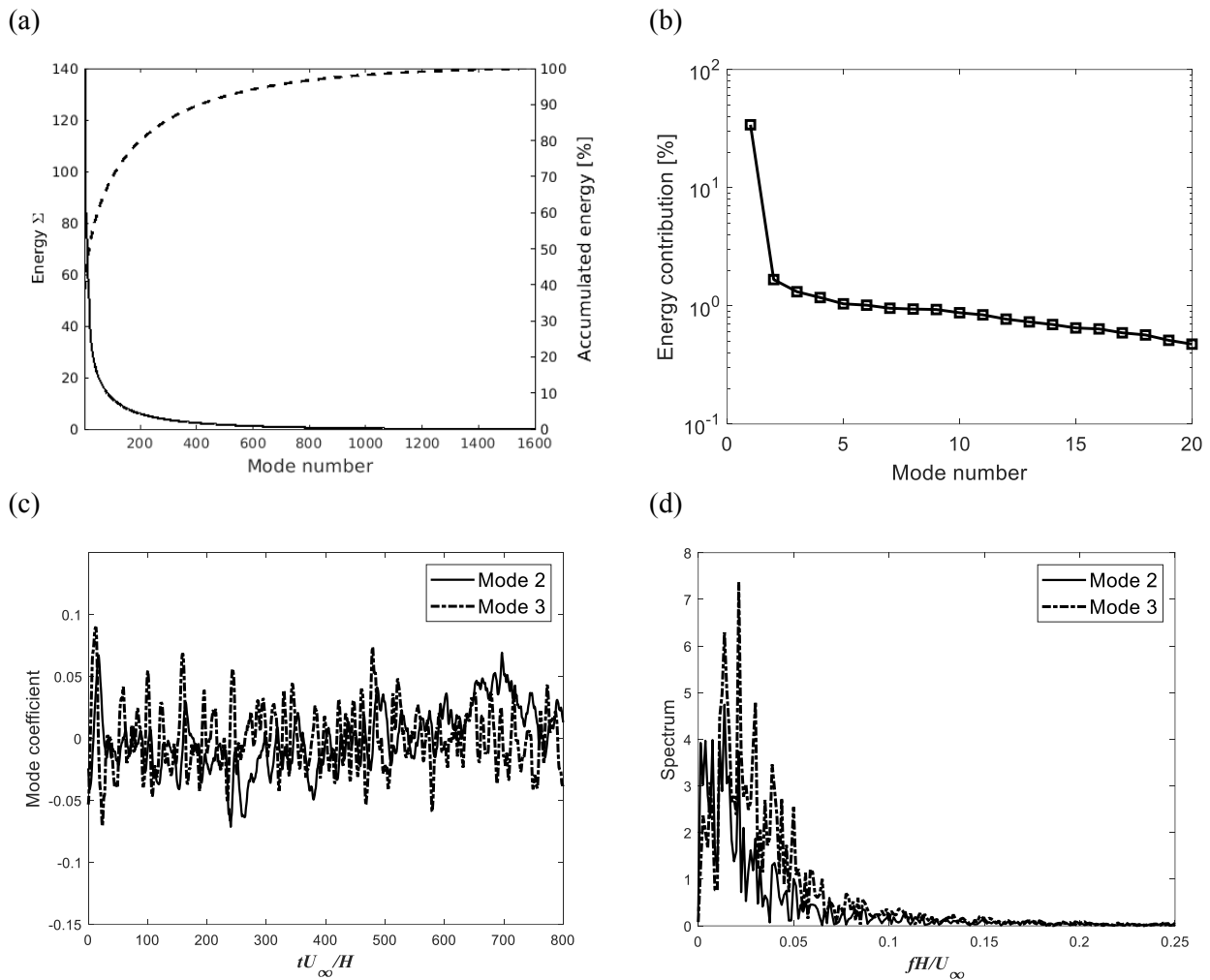


Figure 14: Modal decomposition of the pressure for the square rib: (a) energy of modes, (b) energy contribution of 20 most energetic modes (c) coefficients of Modes 2 and 3 and (d) frequency spectra of Modes 2 and 3

Figure 15 displays the pressure contours of Modes 2 to 9 for the square rib which are fluctuation modes and contain 9.5% of the total energy of the pressure field in the 2D plane. Figure 15 (a) shows a single large-scale pressure structure of Mode 2. Figures 15 (b, c) shows the energetic pair of Modes 3 and 4, which display wave-packet form of structures with similar length scale of the structures and indicate downstream convection of the structures. Furthermore, the POD modes shown in Figures 15 (d) to (g) also appear in pairs with a decreasing length scale of the turbulent structures that are mostly located on the shear layer behind the rib.

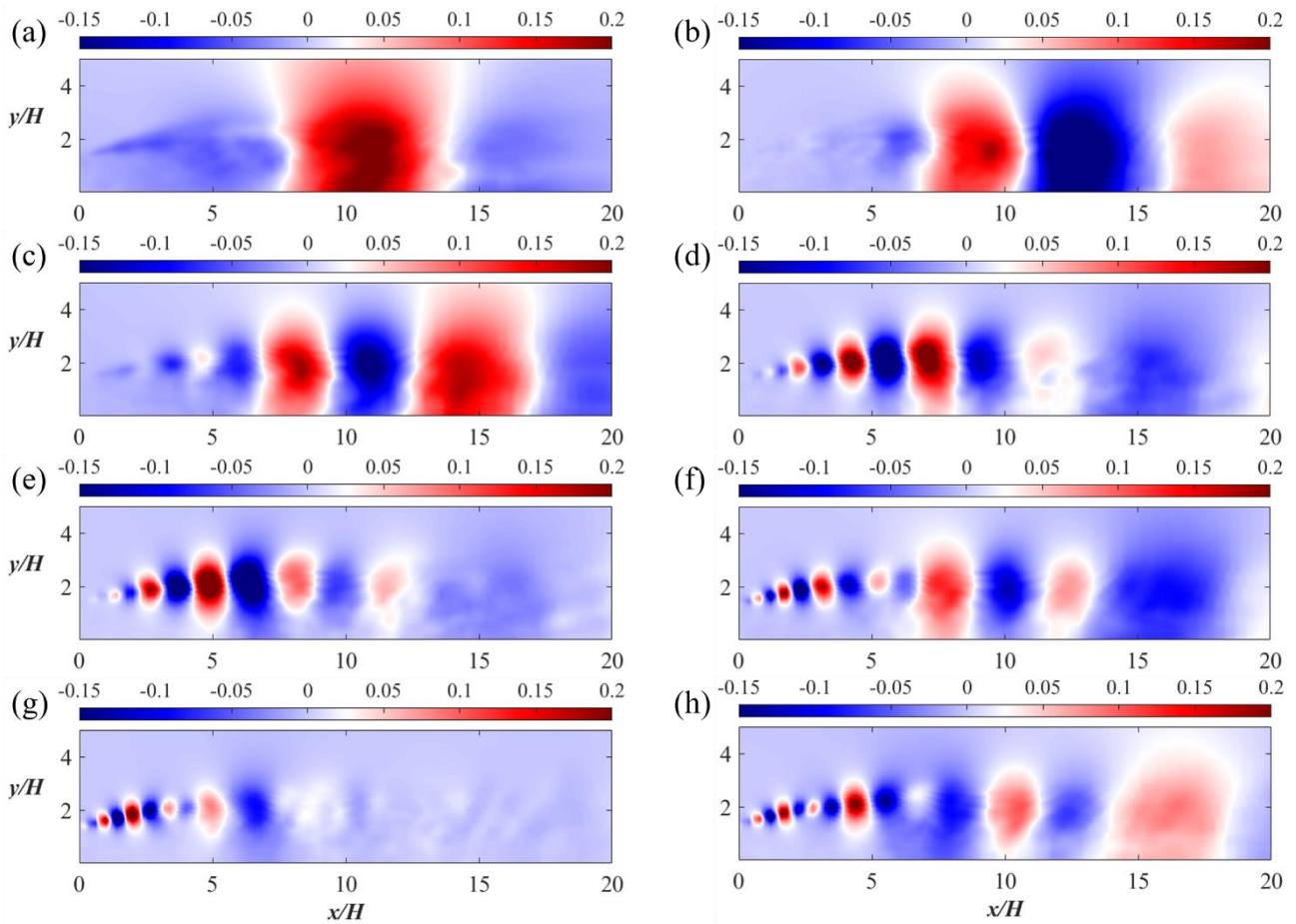


Figure 15: POD modes of the pressure for the square rib: (a) to (h) show POD Modes 2 to 9

4.2.1.2 The trapezoidal rib

Figure 16 (a) shows the energy distribution of the velocity POD modes for the trapezoidal rib case. An exponential decay of the energy from the first modes to the following higher modes is observed. Figure 16 (b) displays the energy contribution of the 20 most energetic modes. The first mode corresponds to the mean flow and contributes with 35% of the total kinetic energy, while each of the following fluctuation modes contains less than 1% of the total energy. It can be seen that the mean flow occupies more energy than that of the square rib which also indicates that velocity fluctuations of wake flow behind the trapezoidal rib are weaker than those behind the square rib. The temporal coefficients as well as their frequency spectra of Modes 2 and 3 are shown in Figures 16 (c) and (d). The peaks of the two Modes temporal coefficients are in the low frequency range and there is slight difference between the two modes. A chaotic behaviour is seen in the time histories of the coefficients of Modes 4 and 5 as shown in Figure 16 (e) and the spectra of the two modes shown in Figure 16 (f) display similar broadband distribution.

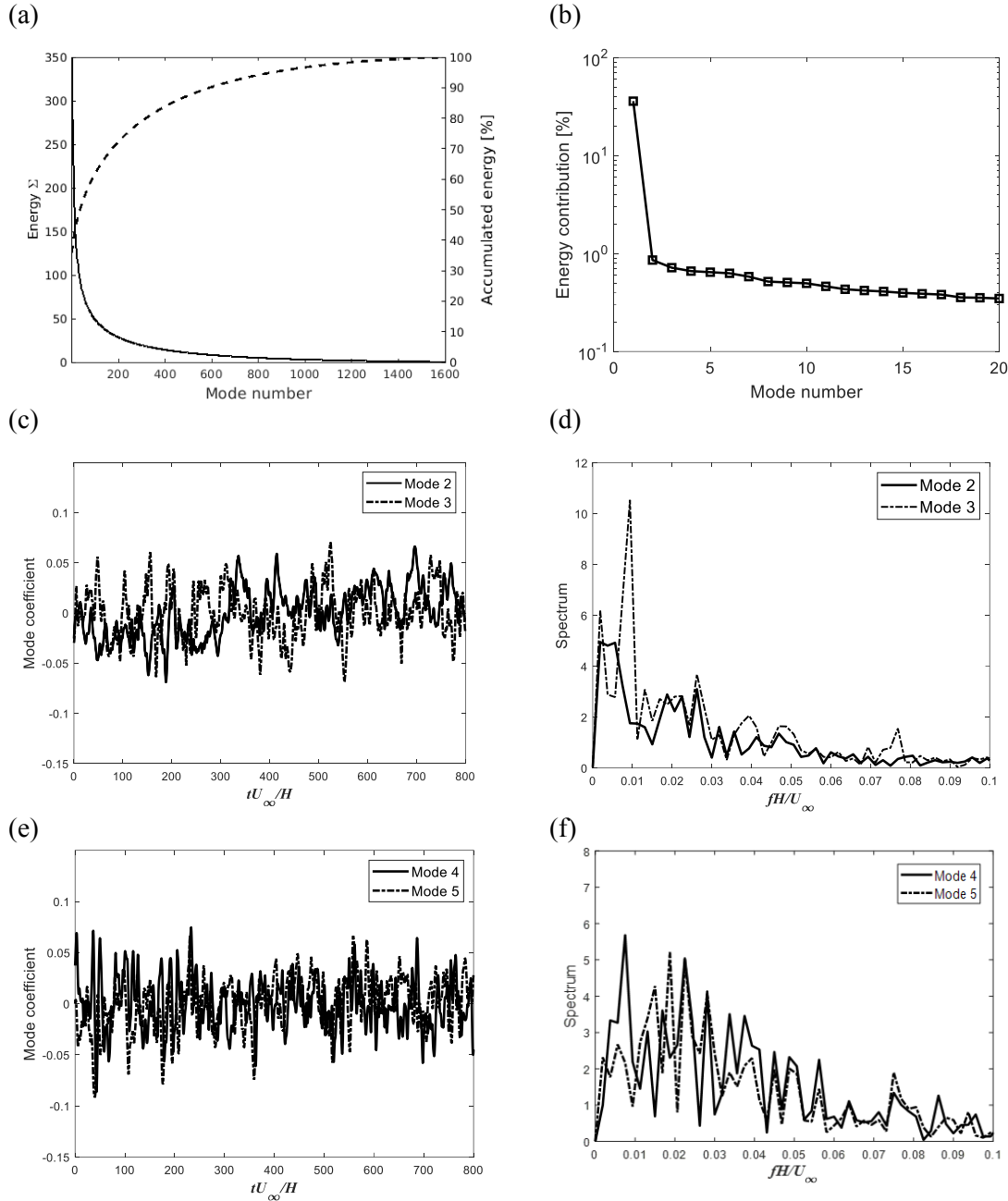


Figure 16: Modal decomposition of the velocities for the trapezoidal rib: (a) energy of modes; (b) energy contribution of most energetic modes; (c) coefficients of Modes 2 and 3, (d) frequency spectra of Modes 2 and 3; (e) temporal coefficients of Modes 4 and 5 and (f) frequency spectra of Modes 4 and 5

The first fluctuation modes are shown in Figures 17 (a) to (h). There is also difference of the mode shapes between Modes 2 and 3, indicating that the two modes cannot form a pair. The streamwise velocities of the first mode show strong flow structures along the shear layer of the wake region. The second mode displays large-scale positive and negative alternate structures. The shapes of Modes 4 and 5 are similar, which can form a pair of modes. This pair of modes shows shorter vortical structures compared with the first pair located with a distance of

8~10H from the back face of the rib. Together with the streamwise velocity modes, the large-scale spanwise rollers are indicated by these POD modes.

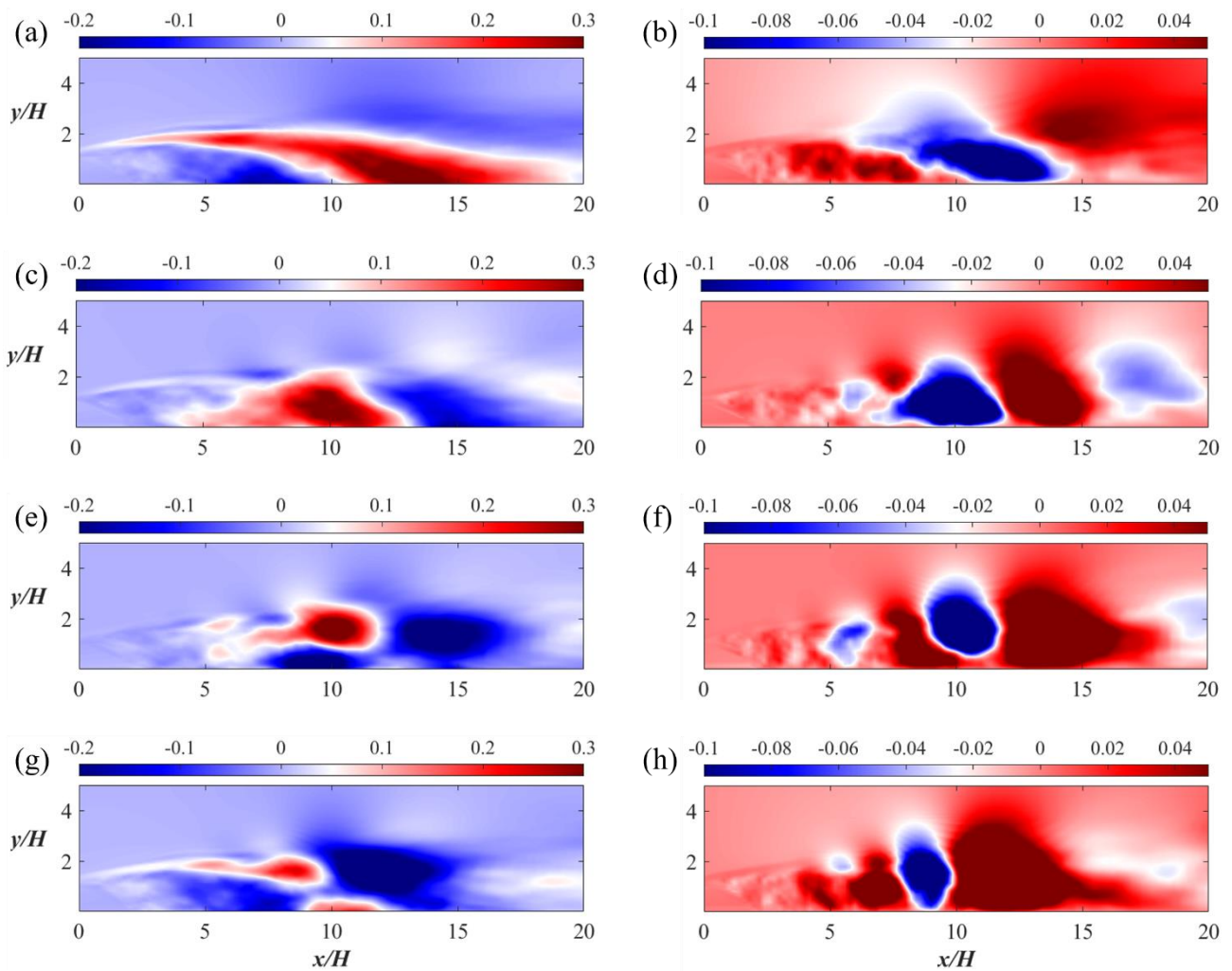


Figure 17: POD modes of the streamwise (a, c, e, g) and cross-stream (b, d, f, h) velocities for the trapezoidal rib: (a, b) POD Mode 2; (c, d) POD Mode 3; (e, f) POD Mode 4 and (g, h) POD Mode 5

The L_2 -norm distribution of the pressure modes for the trapezoidal rib is given in Figure 18 (a). A faster exponential decay of the L_2 -norm from the most energetic modes to the less energetic modes is observed compared with the velocity POD modes as shown in Figure 16 (a). The energy contribution of the first 20 modes is presented in Figure 18 (b). The first mode corresponds to the mean pressure, containing more than 35% of the total energy, while the higher modes contribute less than 2% of the total pressure energy. The temporal coefficient and the frequency spectrum of Mode 2 are shown in Figures 18 (c) and (d). Low frequencies of the mode are observed. POD Modes 3 and 4 appear in pair which is indicated by their similar broadband frequency distribution of the temporal coefficients.

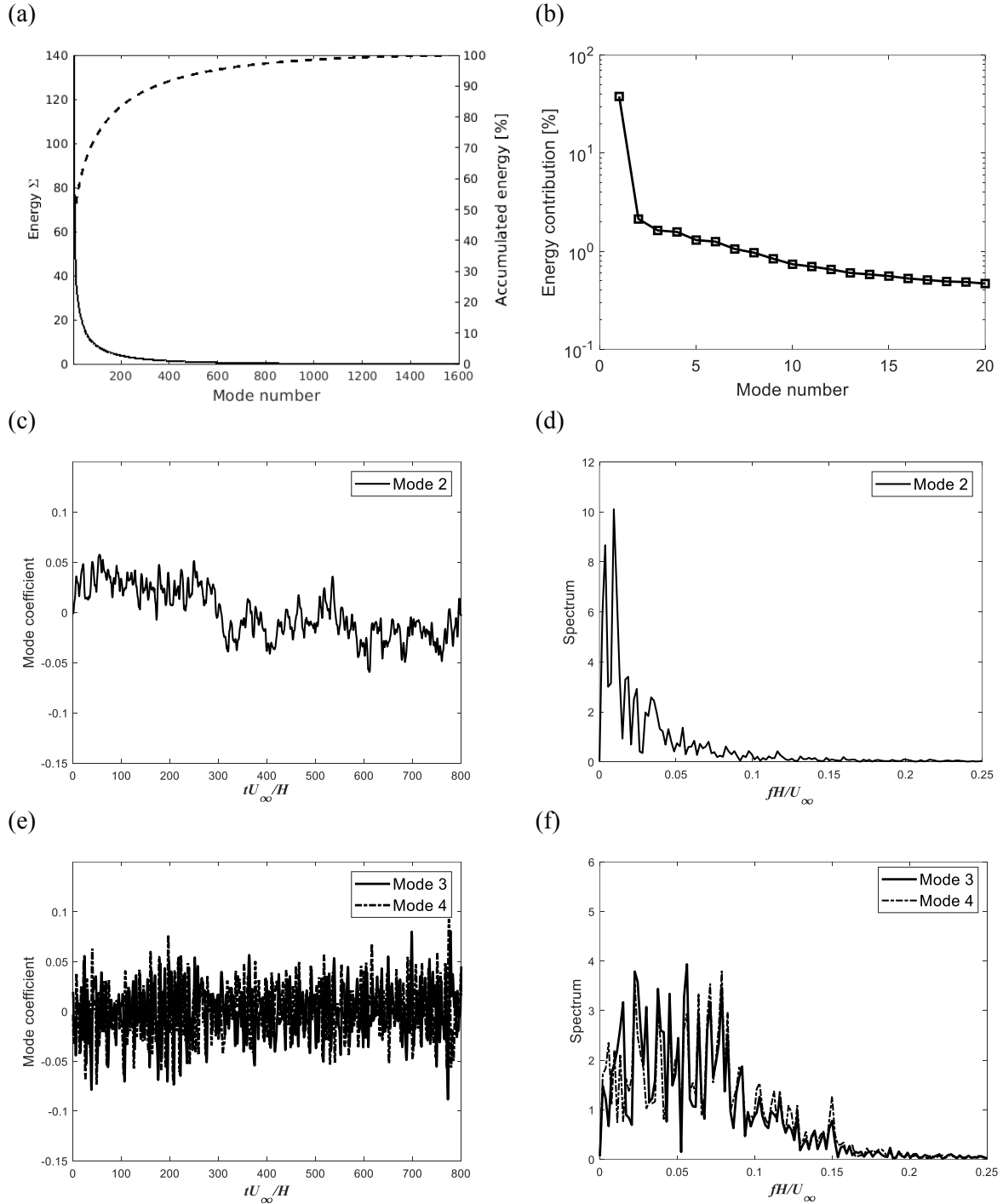


Figure 18: Modal decomposition of the pressure for the trapezoidal rib: (a) energy of modes; (b) energy contribution of the leading energetic modes; (c) coefficients of Mode 2; (d) frequency spectrum of Mode 2; (e) coefficients of Modes 3 and 4; (f) frequency spectra of Modes 3 and 4

Figure 19 shows the pressure POD Modes 2 to 10 for the trapezoidal rib. They contain 10% of the total pressure energy in the 2D plane. The single Mode 2 is presented in Figure 19 (a) and Figures 19 (b, c) show the most energetic pair of modes (Modes 3 and 4). The wave-packets are also shown, and their length scales are decreasing with higher modes. The high order POD modes are shown in Figures 19 (d) to (i) and they are mostly located around the shear layer of

the wake flow. Furthermore, the attachment of the fluctuations to the bottom wall is observed in these high order modes.

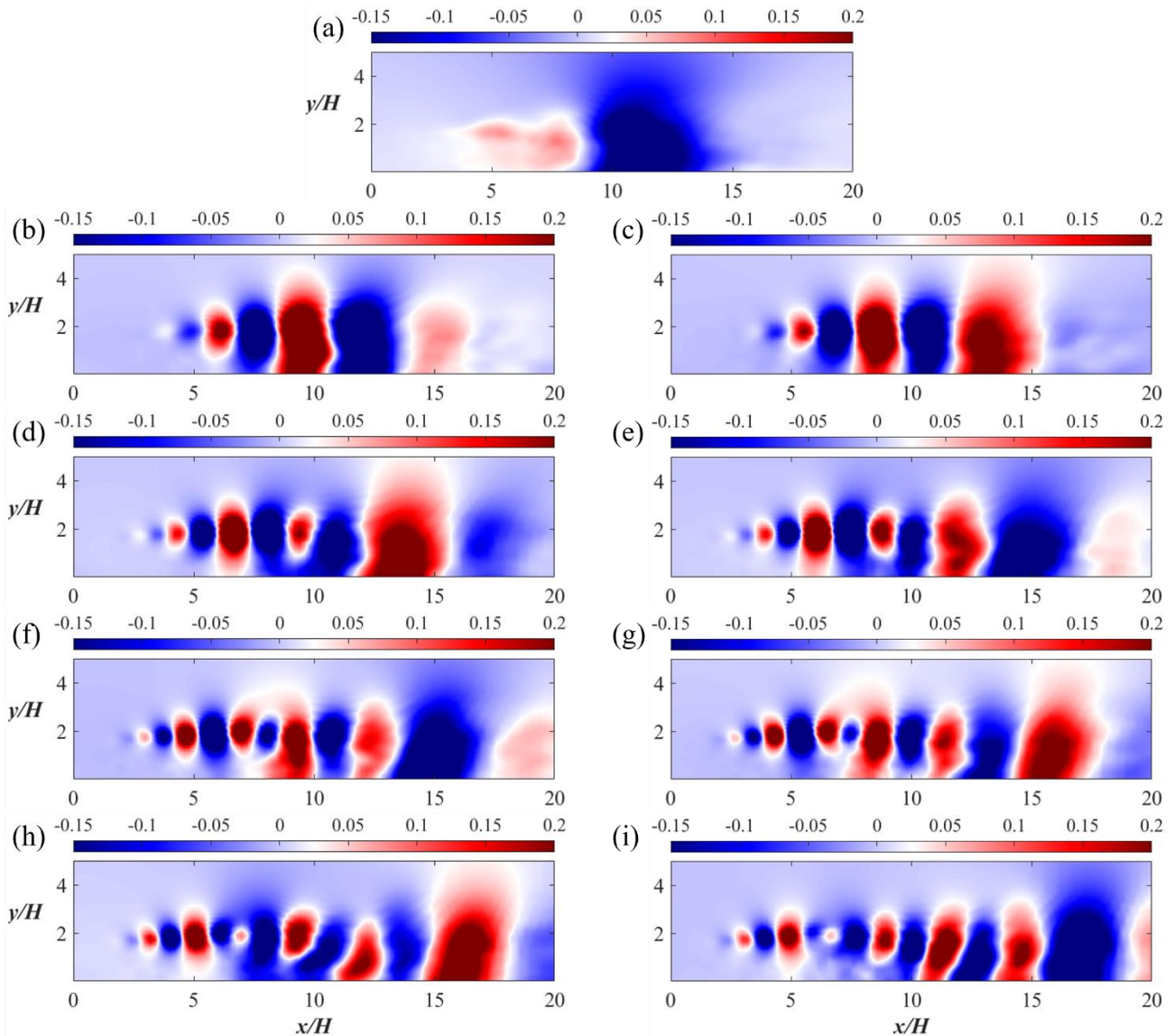


Figure 19: POD modes of the pressure for the trapezoidal rib: (a) to (i) show POD Modes 2 to 10

4.2.1.3 The rectangular rib

Figure 20 (a) shows the energy distribution of the velocity POD modes for the rectangular rib. It also has an exponential decay from lower order modes to higher order modes. Figure 20 (b) shows the energy containing in the first 20 modes. The mean flow represented by the first mode contributes with 35% of the total kinetic energy, while the fluctuation modes have less than 1% of the total energy. The temporal coefficients of Modes 2 and 3 are given in Figures 20 (c, d),

which show the low frequency of the two modes. However, compared with those of the square and trapezoidal ribs, wider frequency distributions are observed for the two modes, indicating a more chaotic behaviour. Figures 20 (e, f) displays the temporal information of the following pair of Modes 4 and 5. It is shown that the corresponding frequency spectra of this pair have wide distribution within the low frequency range.

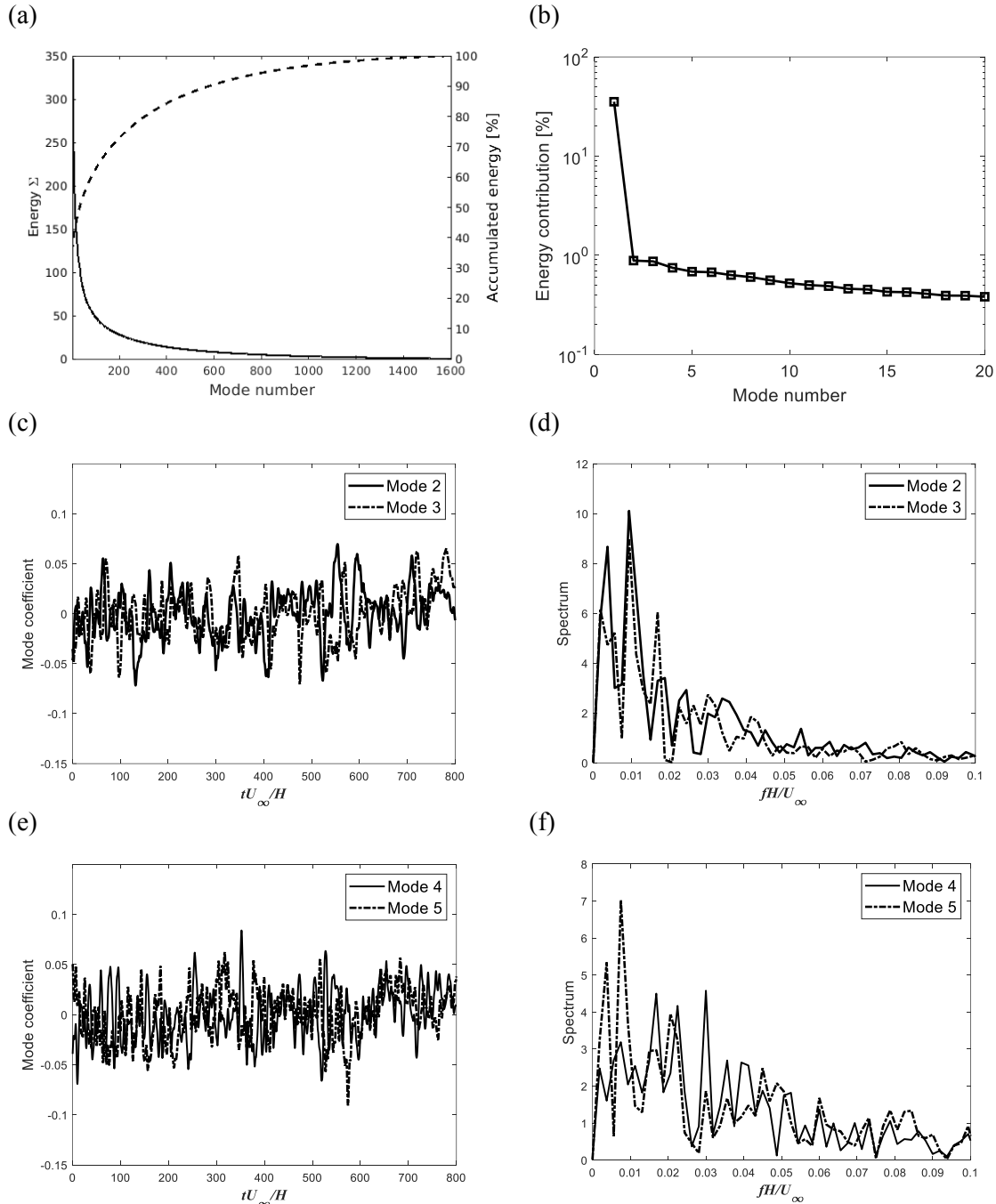


Figure 20: Modal decomposition of the velocities for the rectangular rib: (a) energy of modes; (b) energy contribution of most energetic modes; (c) coefficients of Modes 2 and 3, (d) frequency spectra of Modes 2 and 3; (e) coefficients of Modes 4 and 5, and (f) frequency spectra of Modes 4 and 5

The most energetic pair of modes of the velocities in the streamwise plane (Modes 2 and 3) is shown in Figures 21 (a) to (d) while the following pair (Modes 5 and 6) is given in Figures 21 (e) to (h). The large-scale structures of the first pair are located far from the rib around $x/H = 10 \sim 15$. The streamwise and the cross-stream velocities of the first pair shows similar large-scale rollers structures convected downstream. Their streamwise length-scales are larger than the first pair of modes of the square and trapezoidal ribs. The second pair displays shorter length scale compared with the first pair.

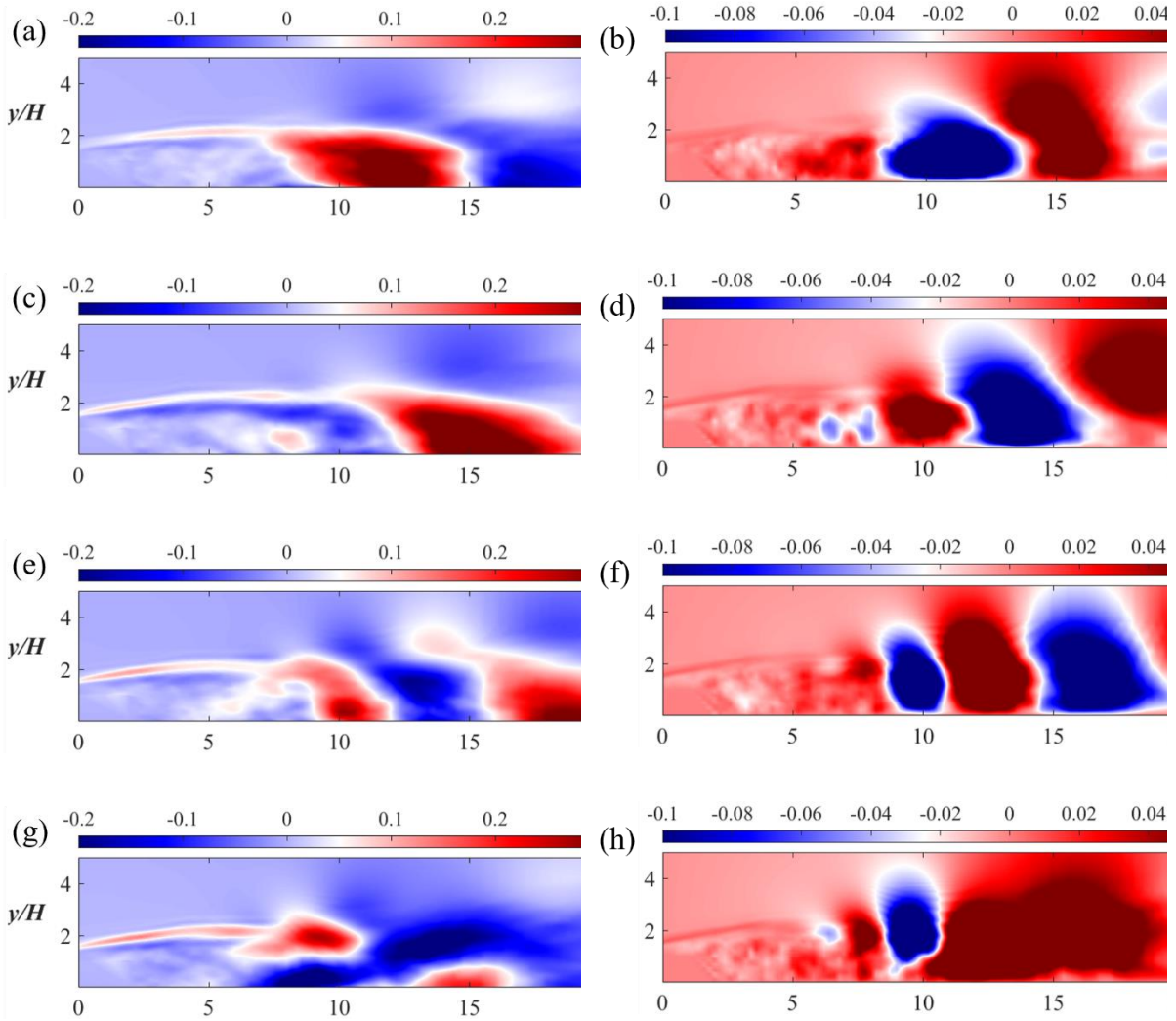


Figure 21: POD modes of the streamwise (a, c, e, g) and cross-stream (b, d, f, h) velocities for the rectangular rib: (a, b) POD Mode 2; (c, d) POD Mode 3; (e, f) POD Mode 4 and (g, h) POD Mode 5

The L_2 -norm distribution of all the pressure POD modes for the rectangular rib is shown in Figure 22 (a). It has a faster exponential decay of the energy compared to the energy distribution of the velocity POD modes. The L_2 -norm contribution of the most energetic modes is

presented in Figure 22 (b). The first mode corresponds to the mean pressure, contributing with 37% of the total energy, while each of the following modes contributes less than 2% of the total energy. Figure 22 (c) shows the temporal coefficients of the pair of Modes 2 and 3 which show a chaotic behaviour. The frequency spectra of the first pair of modes is displayed in Figure 22 (d) and they are more distributed in high frequency range compared to the other ribs.

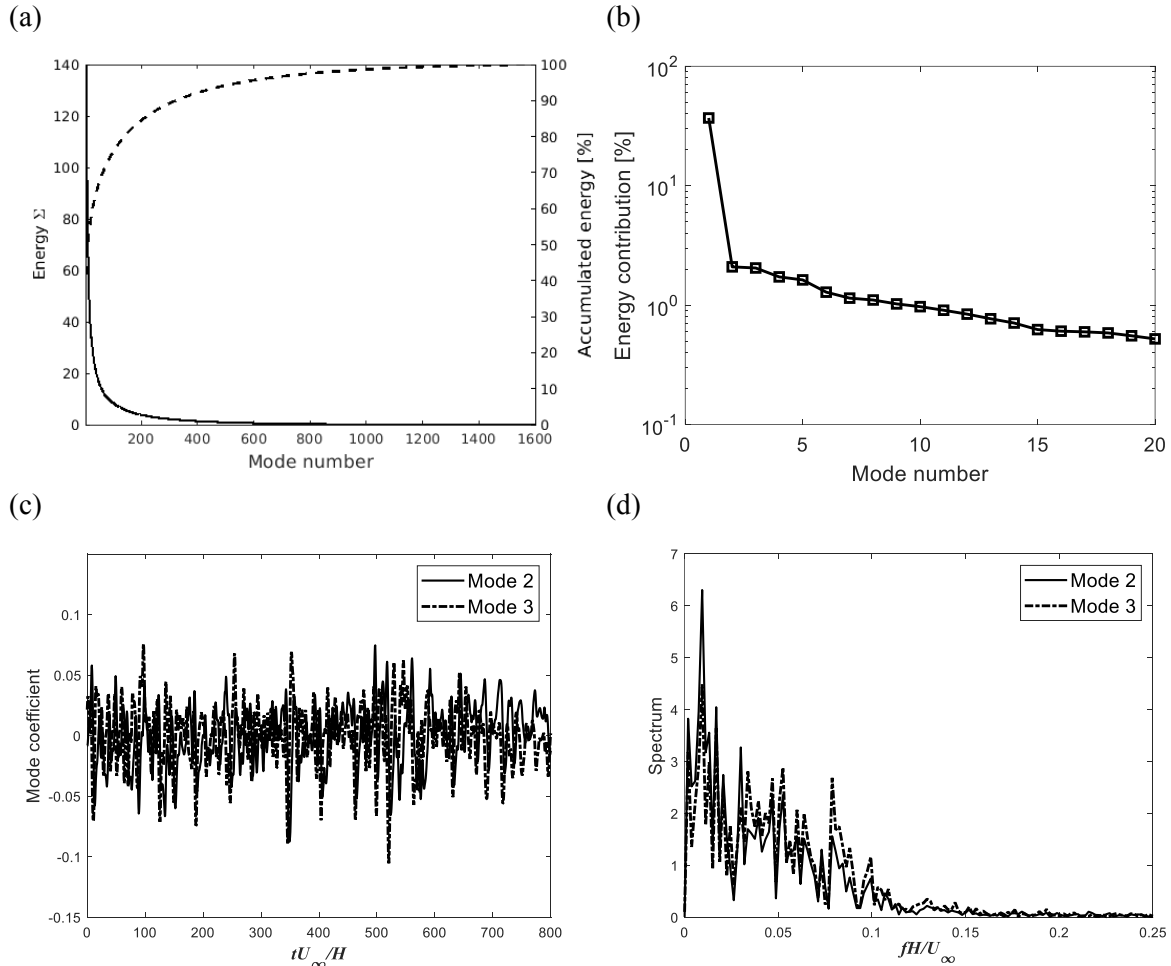


Figure 22: Modal decomposition of the pressure for the rectangular rib: (a) energy of modes; (b) energy contribution of most energetic modes; (c) coefficients of Modes 2 and 3 and (d) frequency spectra of Modes 2 and 3

The first four pairs of the fluctuation pressure POD modes for the rectangular rib are shown in Figure 23. In total, they have 13% of the pressure energy in the 2D plane. Figures 23 (a) and (b) show the first pair of modes (Modes 2 and 3) with a length scale close to the height of the large recirculation motion. The next two pairs of POD modes are shown in Figures 23 (c) to (f) (Modes 4 to 7). They have higher streamwise wavenumber and are located on the edge of the shear layer. Also, small-scale turbulent structures can be seen in Figures 23 (g) and (h), Modes 8 and 10, on the shear layer close to the rib.

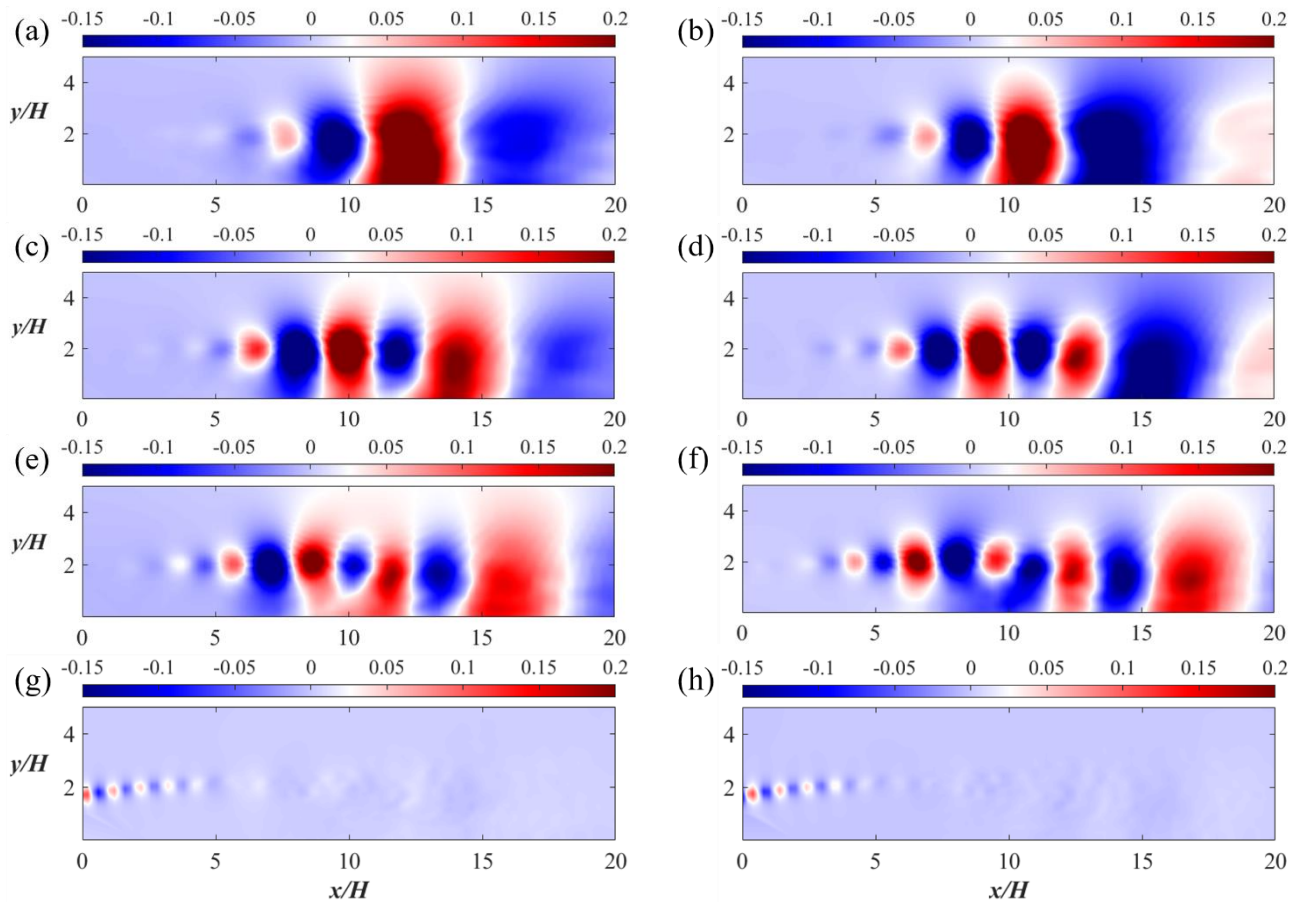


Figure 23: POD modes of the pressure for the rectangular rib: (a) to (h) show POD Modes 2 to 9

4.2.2 Proper orthogonal decomposition analysis along the spanwise direction

To further investigate the 3D characteristics of the coherent structures in the wake flows, POD analysis is also applied to the velocity components (v, w) on ZY -planes. Two planes are chosen with distances of $L_{x,POD} = 1H$ and $6H$ to the back face of the ribs, as shown in Figure 24.

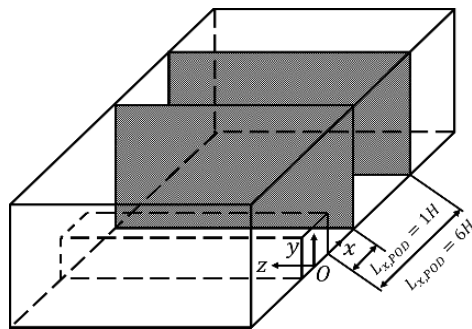


Figure 24: Representation of the snapshots assembling along the spanwise direction

The total number of spatial points of each snapshot ranges from 12342 to 15972 depending on the rib shapes and meshes on the selected plane. A convergence study of the most energetic modes is done in order to determine an acceptable number of snapshots and time step. Figure 25 shows the mean value of ε_{ortho} of the ten most energetic POD modes of all geometries between different numbers of snapshots and the time step. It can be seen that an acceptable convergence can be achieved when Δt_{POD} is 0.5 and a total of 1600 snapshots are used to conduct the analysis for each bottom-mounted rib.

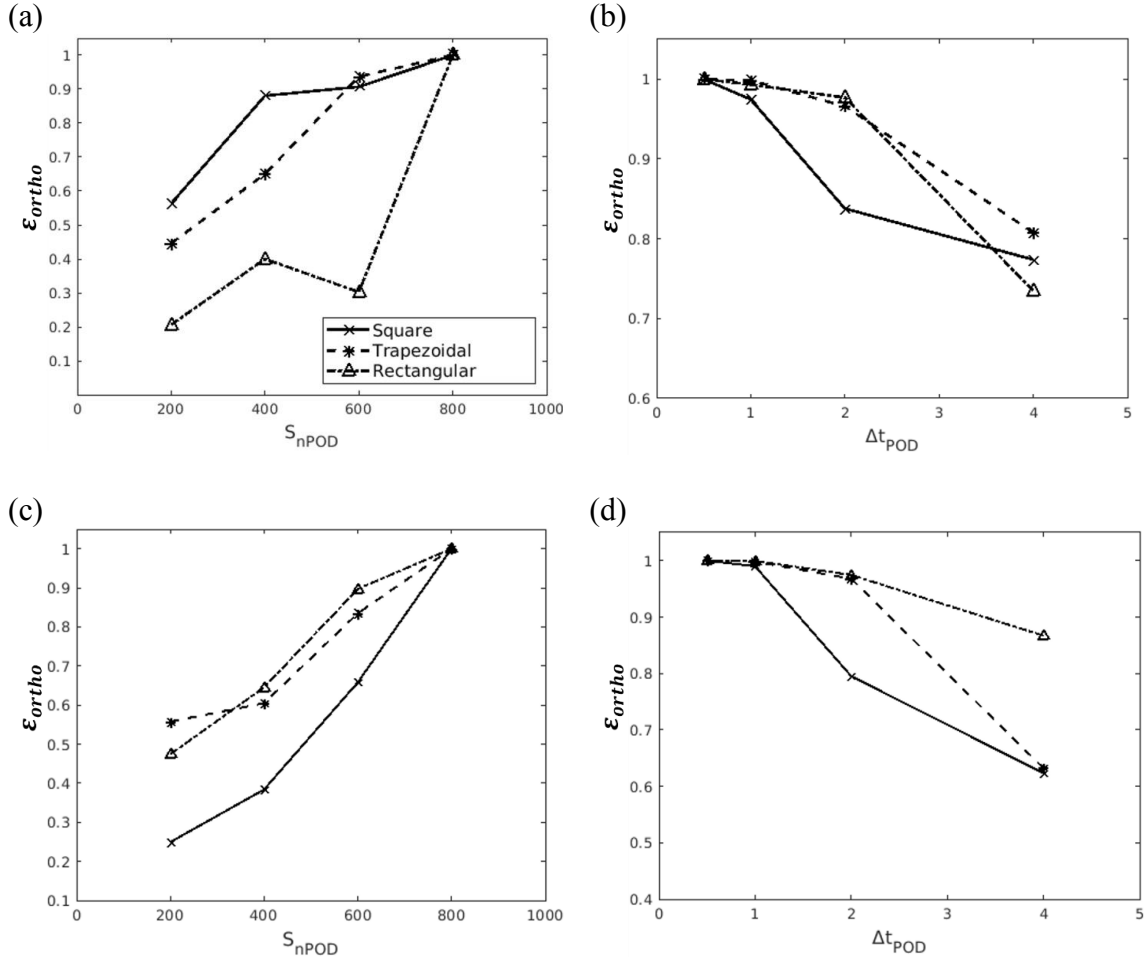


Figure 25: The mean value of ε_{ortho} of the ten most energetic modes between different sets of snapshots of the velocity modes based on: (a) number of snapshots; (b) Δt_{POD} of the velocity modes at $L_{x,POD} = 1H$ behind the ribs; (c) number of snapshots; (d) Δt_{POD} of the velocity modes at $L_{x,POD} = 6H$ behind the ribs

4.2.2.1 The square rib

The energy distribution of all the velocity POD modes with $L_{x,POD} = 1H$ is shown in Figure 26 (a), while the energy contribution of the 20 leading modes is presented in detail in Figure 26 (b). The first mode also corresponds to the mean flow, contributing with more than 9% of the total energy, while the following modes contribute with less than 2% of the kinetic energy of the flow in the 2D plane.

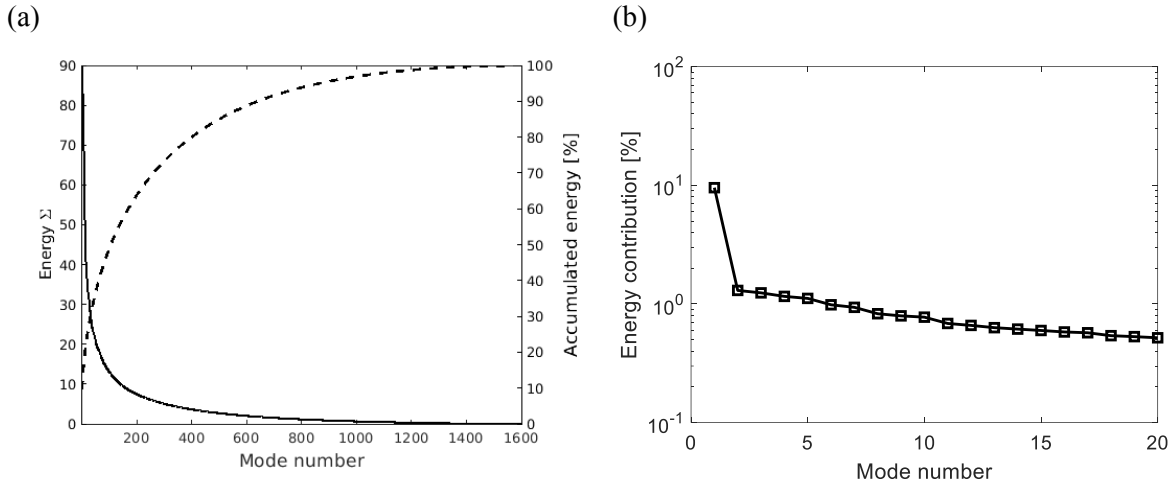


Figure 26: Modal decomposition of the velocities at $L_{x,POD} = 1H$: (a) energy of modes and (b) energy contribution of most energetic modes

Contours of the POD velocity modes with $L_{x,POD} = 1H$ are shown in Figure 27: (a) and (c) show the first pair of the fluctuation modes (Modes 2 and 3), while (e) and (g) show the second pair (Modes 4 and 5) of the cross-stream velocity. The two modes of each pair have similar level of energy as shown in Figure 26 (b) indicating the downstream convection of the flow modes. Both pairs show a strong shear layer above the rib height which is located on the edge of the wake flow. Figures 27 (b, d, f, h) display the spanwise velocity contours of Modes 2, 3 and Modes 4, 5, showing more complex turbulent structures which indicates a chaotic flow in the spanwise direction inside the near wake region.

The energy distribution of the velocity POD modes at $L_{x,POD} = 6H$ behind the square rib is shown in Figure 28 (a). An exponential decay of the energy distribution with the increasing mode number is observed and the energy contribution of the most energetic modes is presented in Figure 28 (b). It can be seen that only fluctuation modes appear since the mean values for v, w are small at this streamwise location.

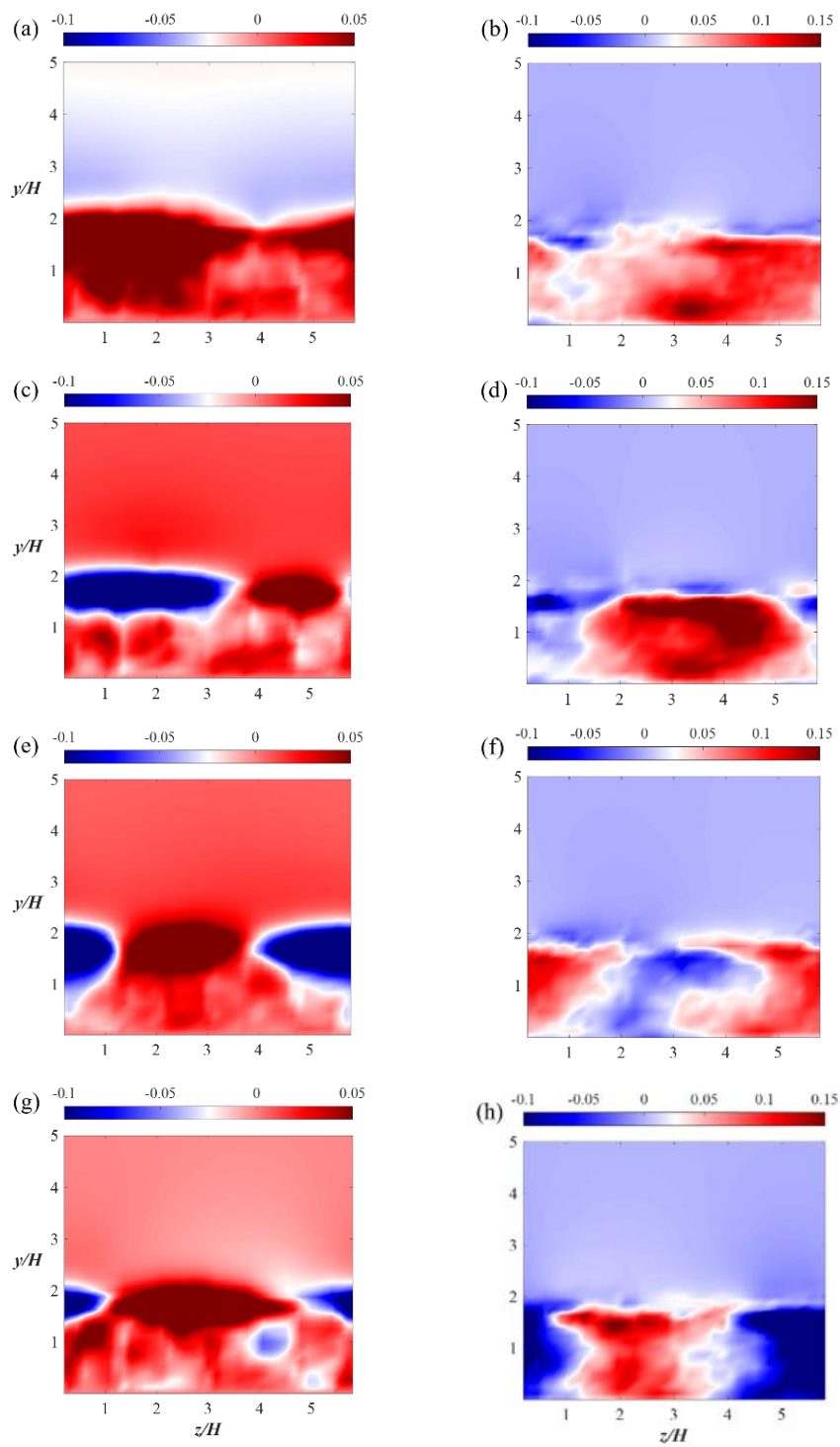


Figure 27: POD modes of the velocities at $L_{x,POD} = 1H$ after the square rib: (a, b) POD Mode 2; (c, d) POD Mode 3; (e, f) POD Mode 4; and (g, h) POD Mode 5 with the cross-stream velocities (a, c, e, g) and the spanwise velocities (b, d, f, h)

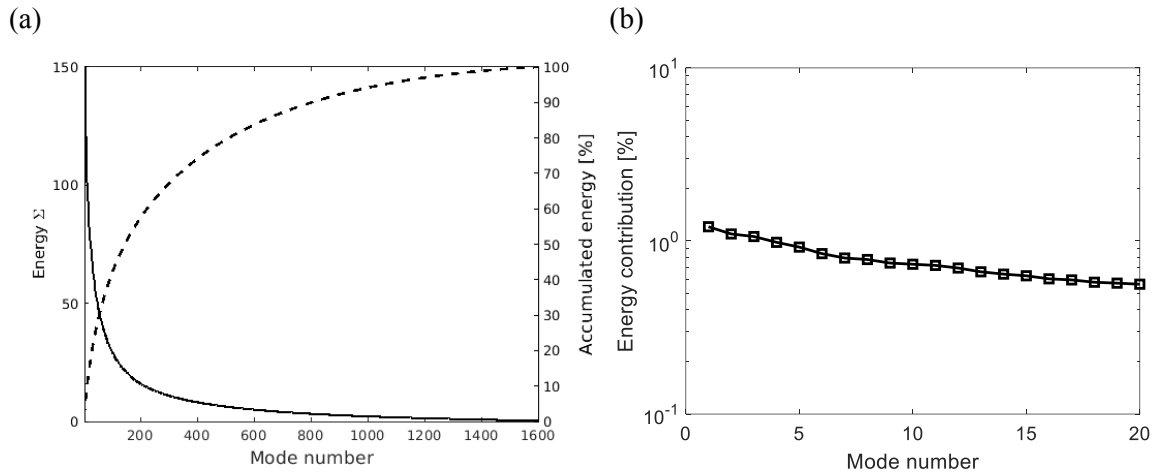


Figure 28: Modal decomposition of the velocities at $L_{x,POD} = 6H$: (a) energy of modes and (b) energy contribution of most energetic modes

Contours of the POD velocity modes with $L_{x,POD} = 6H$ downstream the square rib are shown in Figure 29 and all of them can be considered fluctuation modes. For the first pair of Modes 1 and 2, the structures occupy the whole area of the wake region. Large-scale positive and negative regions of the cross-stream velocity indicates strong downwards and upwards flows. Together with the spanwise velocity as shown in Figures 29 (b) and (d), Modes 1 and 2 represents large-scale streamwise vortices. Modes 3 and 4 of the second pair have smaller length-scale comparing with Modes 1 and 2. The modes shapes also represent streamwise vortices with a smaller spanwise length.

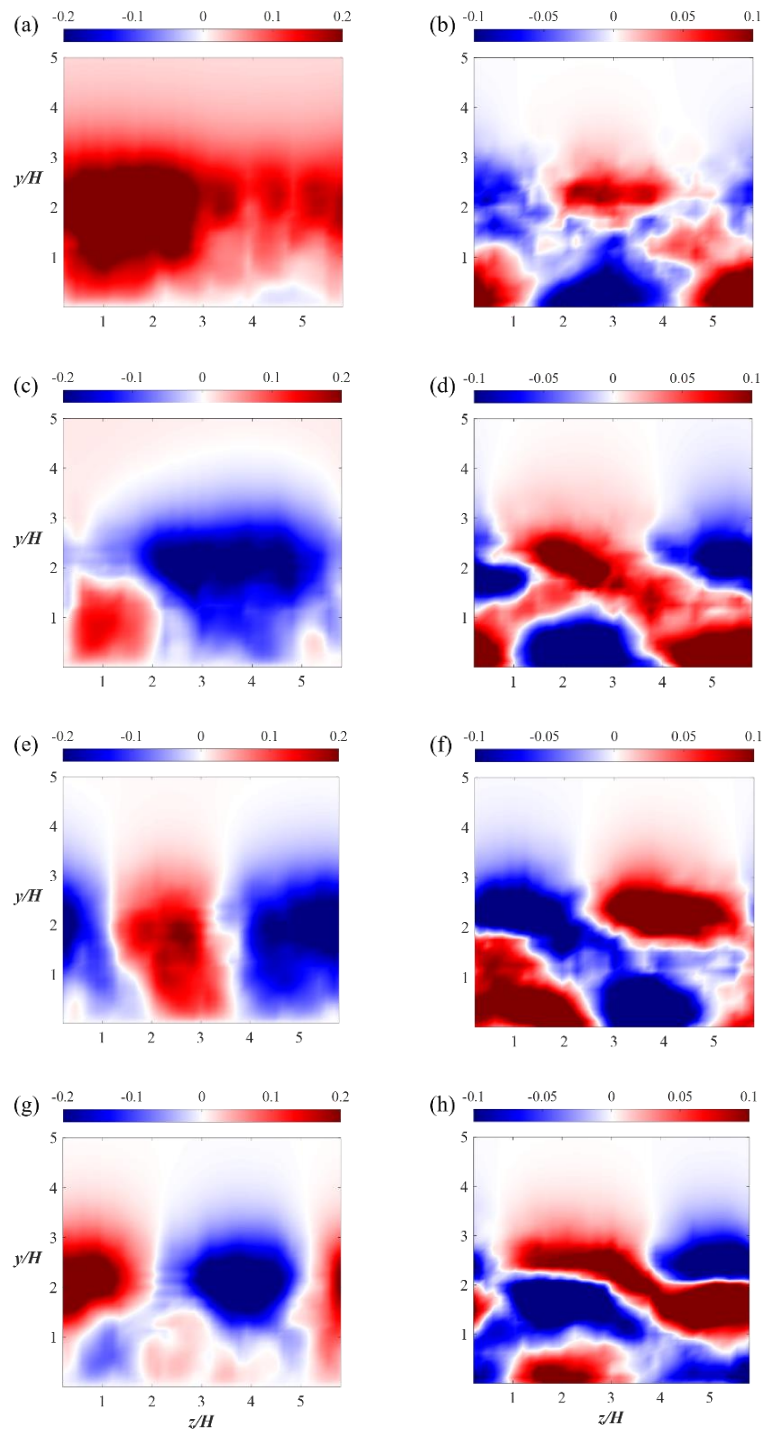


Figure 29: POD modes of the velocities at $L_{x,POD} = 6H$ after the square rib: (a, b) POD Mode 1; (c, d) POD Mode 2; (e, f) POD Mode 3; and (g, h) POD Mode 4 with the cross-stream velocities (a, c, e, g) and the spanwise velocities (b, d, f, h)

4.2.2.2 The trapezoidal rib

The energy distribution of the velocity modes at $L_{x,POD} = 1H$ downstream the trapezoidal rib is given in Figure 30 (a) and it is possible to observe an exponential decay of energy from lower modes to higher modes. The energy contribution of the first 20 modes is presented in Figure 30 (b). The first mode, corresponding to the mean flow, contains 8% of the total energy, while each of the higher order POD modes contribute with less than 2% of the energy.

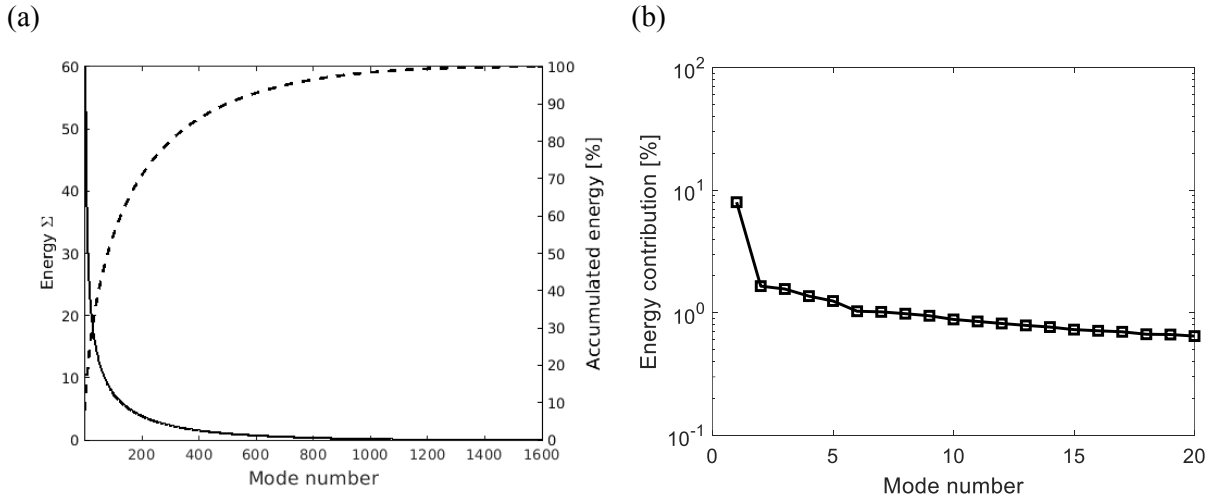


Figure 30: Modal decomposition of the velocities at $L_{x,POD} = 1H$ after the trapezoidal rib: (a) energy of modes and (b) energy contribution of most energetic modes

Contours of the POD velocity modes at $L_{x,POD} = 1H$ behind the trapezoidal rib are shown in Figure 31. Figures 31 (a) to (d) show two most energetic single fluctuation modes (Modes 2 and 3), while (e) to (h) show the pair of Modes 4 and 5. The complex and chaotic flow behaviours are shown in these modes.

Figure 32 (a) shows the energy distribution of all the velocity POD modes at $L_{x,POD} = 6H$ behind the trapezoidal rib with a lower exponential decay compared with that at $L_{x,POD} = 1H$. However, different from that of the square rib, the energy fraction of the first mode given in Figure 32 (b) is around 2% of the total energy of the velocity components in the 2D plane and it still can represent the mean flow. Figures 33 (a) to (h) gives the first two pairs of the cross-stream and spanwise velocities of POD modes (Modes 2, 3 and Modes 4, 5) at $L_{x,POD} = 6H$ downstream the trapezoidal rib with structures distributed throughout the center part of the wake region. The first pair clearly shows large-scale streamwise vortical structures with low spanwise wavenumber while the second pair also displays strong streamwise vortical structures with relatively higher spanwise wavenumber.

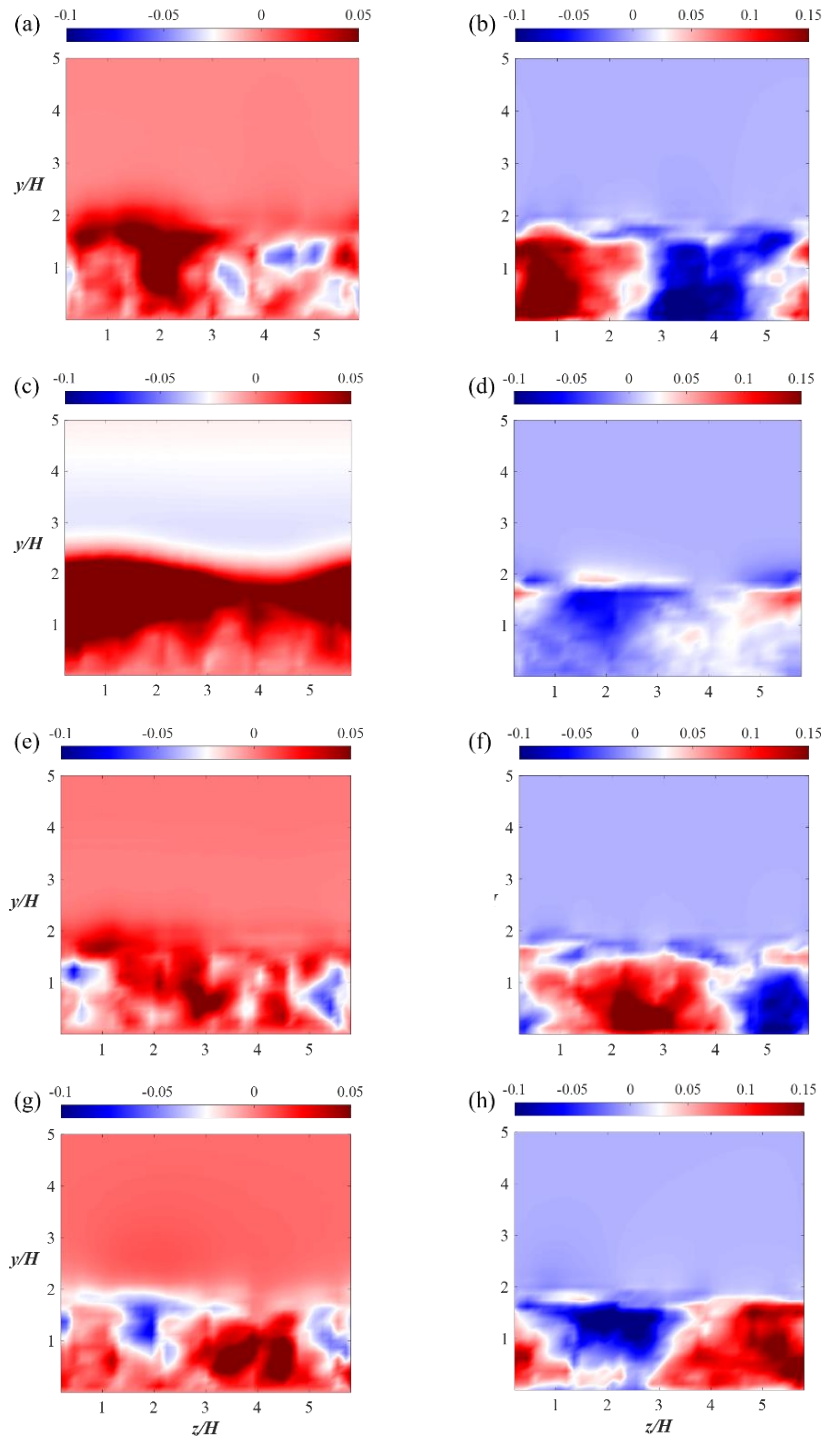


Figure 31: POD modes of the velocities at $L_{x,POD} = 1H$ after the trapezoidal rib: (a, b) POD Mode 2; (c, d) POD Mode 3; (e, f) POD Mode 4; and (g, h) POD Mode 5 with the cross-stream velocities (a, c, e, g) and the spanwise velocities (b, d, f, h)

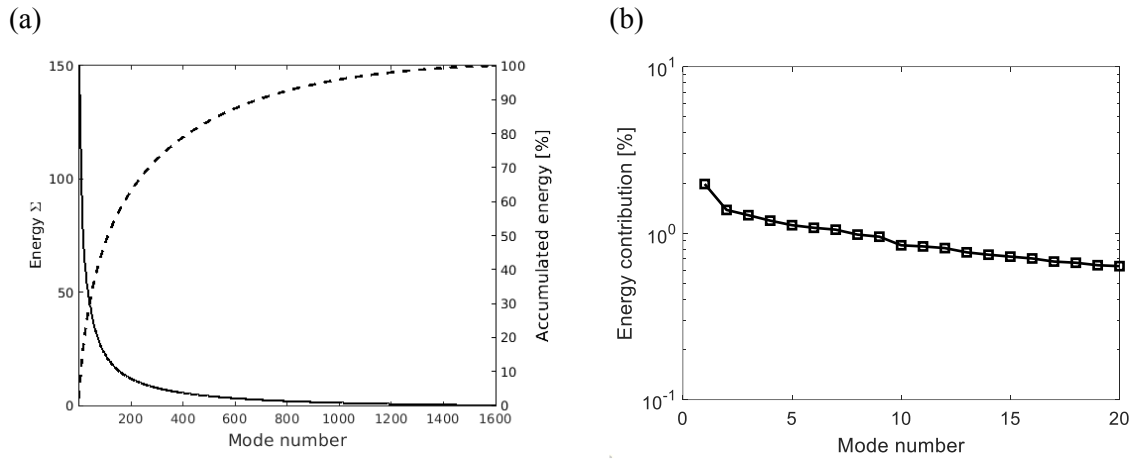
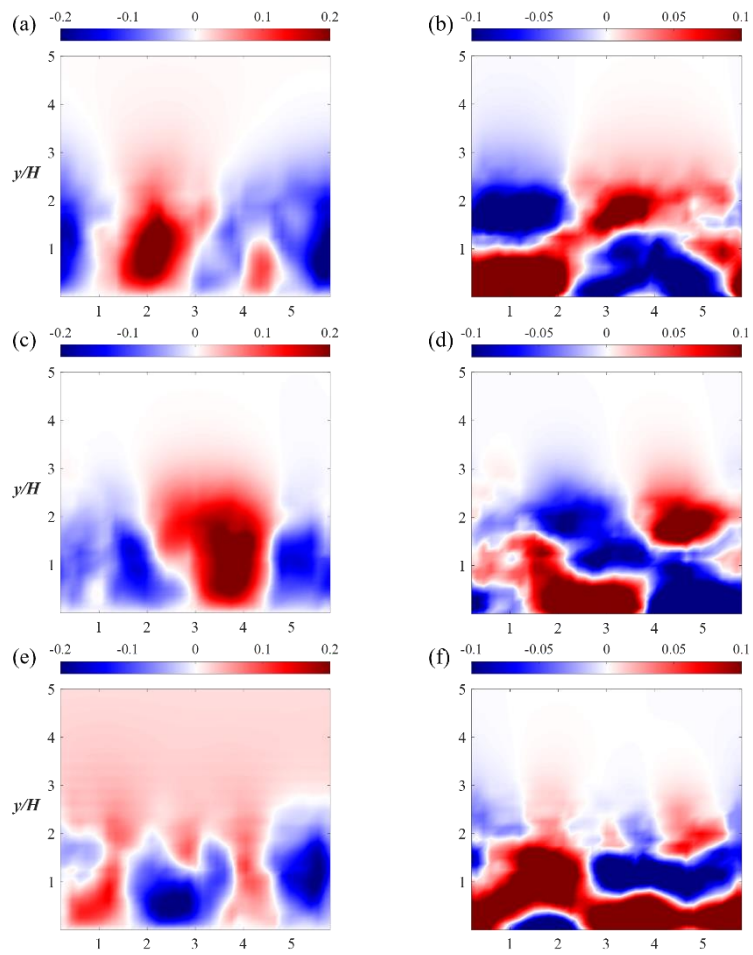


Figure 32: Modal decomposition of the velocities at $L_{x,POD} = 6H$ after the trapezoidal rib: (a) energy of modes and (b) energy contribution of most energetic modes



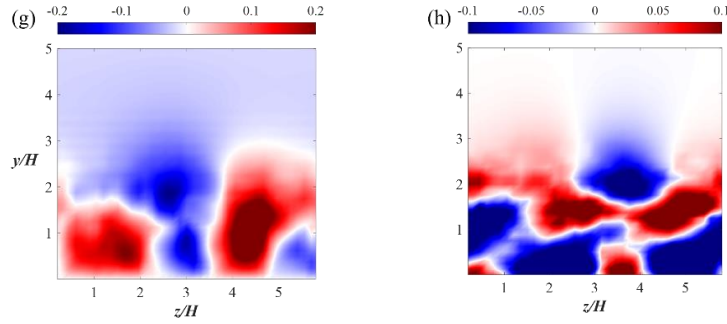


Figure 33: POD modes of the velocities at $L_{x,POD} = 6H$ after the trapezoidal rib: (a, b) POD Mode 2; (c, d) POD Mode 3; (e, f) POD Mode 4; and (g, h) POD Mode 5 with the cross-stream velocities (a, c, e, g) and the spanwise velocities (b, d, f, h)

4.2.2.3 The rectangular rib

Figure 34 (a) gives the energy distribution of all velocity POD modes at $L_{x,POD} = 1H$ after the back face of the rectangular rib with an exponential decay. The energy contribution of the first 20 modes is given in detail in Figure 34 (b) with the first mode dominating the flow with 9% of the total energy in the 2D plane, while each of the following fluctuation modes contain less than 2% of the energy contribution. POD velocity modes at $L_{x,POD} = 1H$ after the rectangular rib are displayed in Figure 35 and give complex flow structures: (a) to (d) show the fluctuation Modes 2 and 3 with strong structures around the shear layer at $y/H \approx 2$ with a few vortical structures inside the near wake region. This pair of modes does not seem to have significant large-scale turbulent structures inside the wake region. Modes 4 and 5 are displayed in Figures 35 (e) to (h) showing a large-scale cross-stream length vortical structure centered at the rib height.

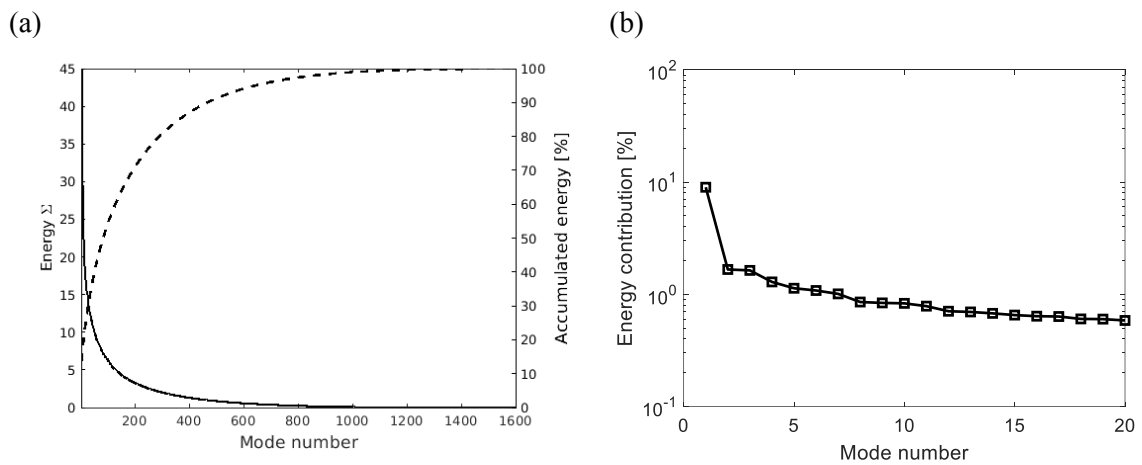


Figure 34: Modal decomposition of the velocities at $L_{x,POD} = 1H$ after the rectangular rib: (a) energy of modes and (b) energy contribution of most energetic modes

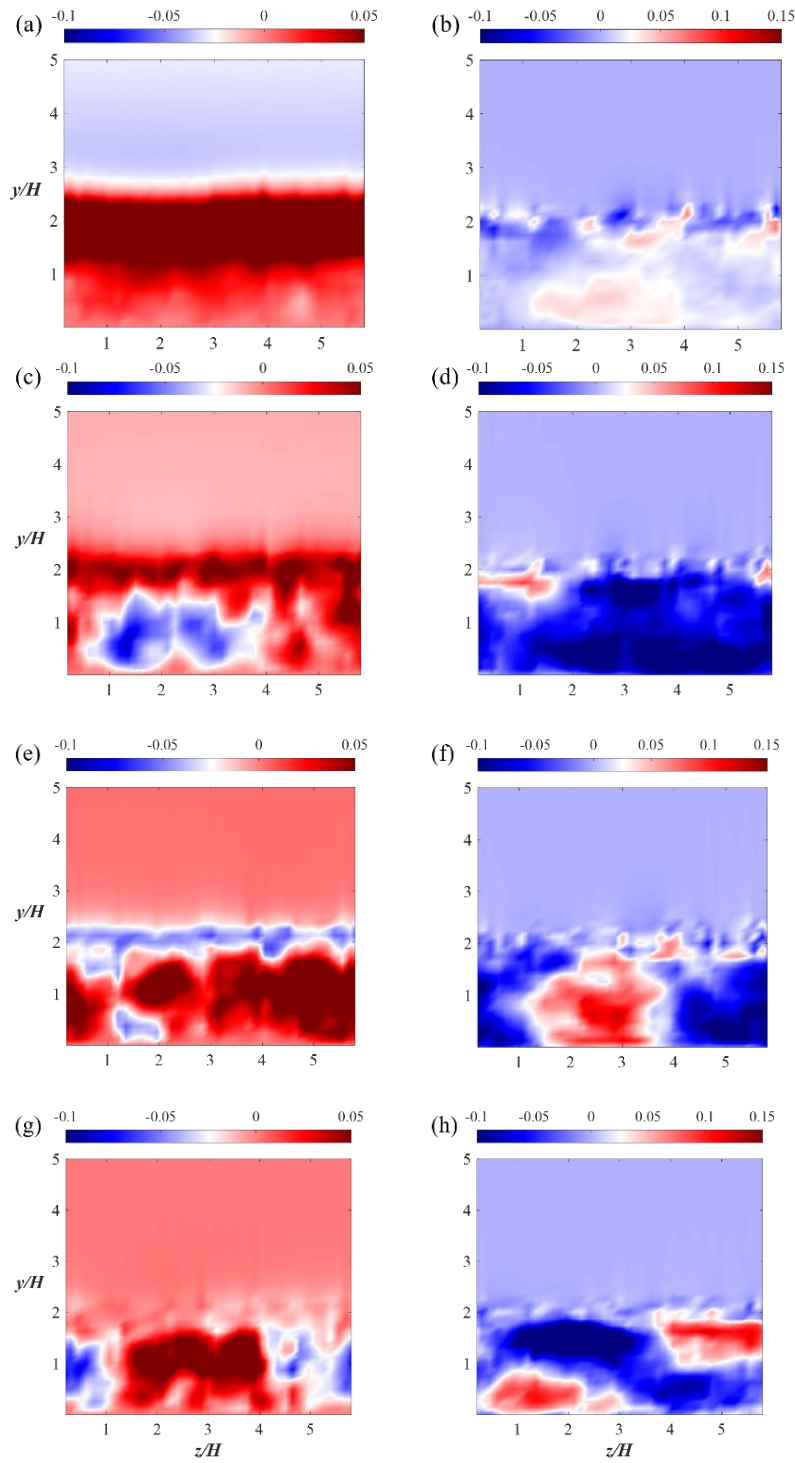


Figure 35: POD modes of the velocities at $L_{x,POD} = 1H$ behind the rectangular rib: (a, b) POD Mode 2; (c, d) POD Mode 3; (e, f) POD Mode 4; and (g, h) POD Mode 5 with the cross-stream velocities (a, c, e, g) and the spanwise velocities (b, d, f, h)

The energy distribution of all velocity POD modes at $L_{x,POD} = 6H$ after the back face of the rectangular rib is given in Figure 36 (a). The energy contribution of the first 20 modes is shown in Figure 36 (b) with the most energetic mode contributing with only 2.5% of the kinetic energy, however it can be considered a representation of the mean flow. The following modes contain less than 2% of energy contribution individually. Contours of the POD velocity modes at $L_{x,POD} = 6H$ downstream the rectangular rib are shown in Figure 37: (a, b) show the single fluctuation Mode 2. The cross-stream velocity of Mode 2 represents spanwise uniform downward flow in the wake and the spanwise velocity of this mode represents the flow towards the two spanwise directions. The pair of Modes 3 and 4 is shown in Figures 37 (c, d) and (e, f) representing streamwise vorticities. Figures 37 (g, h) display Mode 5 which represents an ejection motion in the wake flow.

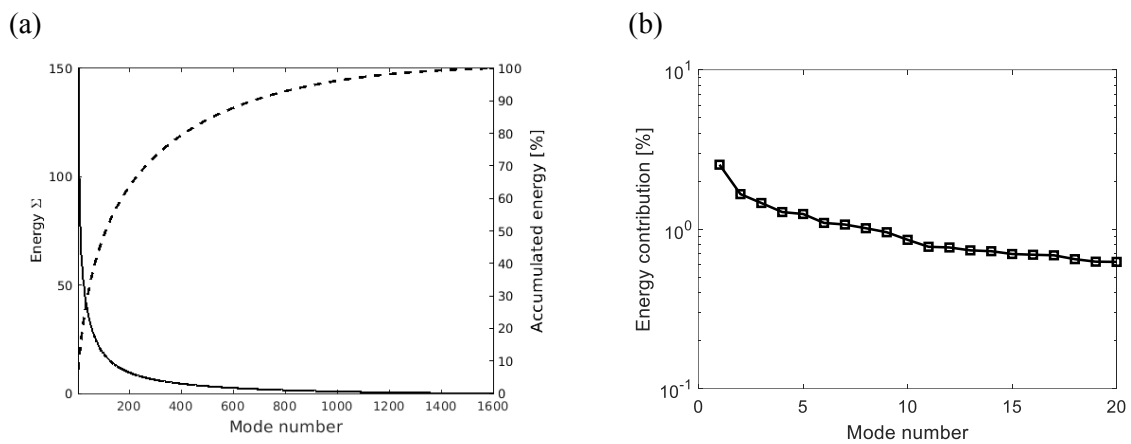


Figure 36: Modal decomposition of the velocities at $L_{x,POD} = 6H$ after the rectangular rib: (a) energy of modes and (b) energy contribution of most energetic modes

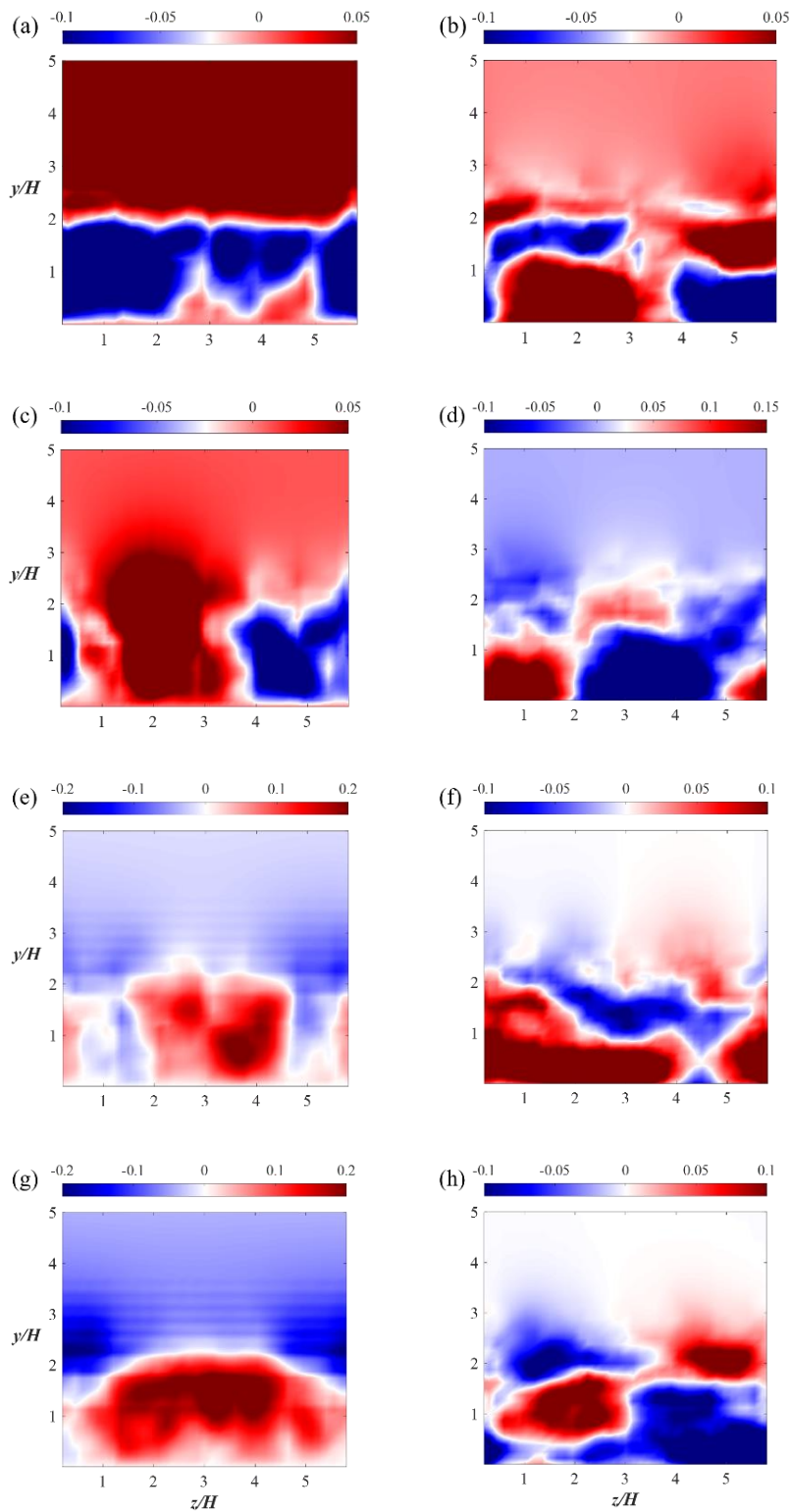


Figure 37: Modal decomposition of the velocities at $L_{x,POD} = 6H$ after the rectangular rib: (a, b) POD Mode 2; (c, d) POD Mode 3; (e, f) POD Mode 4; and (g, h) POD Mode 5 with the cross-stream velocities (a, c, e, g) and the spanwise velocities (b, d, f, h)

5. Conclusion

In the present study, Spalart-Allmaras Delayed Detached-eddy simulations of flows over three different bottom-mounted ribs subjected to a boundary layer with a thickness of $\delta/H = 0.73$ at $Re = 1.0 \times 10^6$ are carried out. Convergence studies based on the time- and spanwise-averaged hydrodynamic quantities $\overline{C_D}$ and $\overline{C_L}$ are performed to determine the grid and time step resolutions. The time- and spanwise-averaged streamwise velocities behind the square rib were compared with the experimental data reported by Liu et al. (2008) and a generally good agreement is achieved. Results of the hydrodynamic quantities and the turbulent wake flow were analysed. Proper orthogonal decomposition of the velocities and the pressure at one 2D XY-plane and two ZY-planes is used to extract the most energetic modes and careful convergence studies have been carried out to determine the necessary number of snapshots and the time step between the snapshots. The main conclusions can be outlined as follows:

1. The complexity of the vortical structures is reduced for the rectangular and the trapezoidal ribs compared with the square rib, resulting in reduced pressure differences of the rectangular and trapezoidal ribs and thus lower drag coefficients compared with the square rib.
2. A positive correlation between the time-histories of C_D and C_L for the three structures is observed. The streamlines of the time- and spanwise-averaged flows for the three ribs display large recirculation motions behind the ribs. The square rib produces the longest recirculation motion among the three ribs. There are two small recirculation motions in front and in the corner of the back face of the square and rectangular ribs while for the trapezoidal rib, the flow streamlines are attached to the rib surface with no other small recirculation motion.
3. The energy contained in the POD modes show an exponential decay from the first modes to the higher modes. For the flow velocity components and pressure at the 2D XY-plane, the first mode corresponds to the mean flow and contains more than 30% of the total energy for all the different ribs. Most of the POD modes of the velocities and pressure fluctuation appear in pairs, indicating the downstream convection of the flow structures. The first pair of the fluctuation POD modes shows strong shear layer stemming from the ribs. High order fluctuation modes on the XY-plane display a wave-packet form of structures with alternate positive and negative value regions and their length scales decrease with the increasing order. The structures of the high order pressure modes are mainly located around the shear layer of the wake flow.

4. The POD modes of the cross-stream and spanwise velocities at the two ZY-planes are analysed. With a distance of $1H$ to the ribs back face, the POD modes are mainly located around the shear layer. For the square rib with a distance of $6H$ to the rib back face, due to the small mean value of the cross-stream velocity and the zero mean spanwise velocity, there is no POD mode for the mean flow. Also, the POD modes of the velocities represent streamwise vorticities with different length-scales. For the trapezoidal and rectangular ribs, the first mode corresponds to the mean flow and the fluctuation modes also display streamwise vortices. These streamwise vortical structures indicate the strong motions in the spanwise direction.

References

- Amor, C., Pérez, J. M., Schlatter, P., Vinuesa, R. & Le Clainche, S. (2019). Soft computing techniques to analyze the turbulent wake of a wall-mounted square cylinder. In *International Workshop on Soft Computing Models in Industrial and Environmental Applications* (pp. 577-586). Springer, Cham.
- Arie, M., Kiya, M., Tamura, H. & Kanayama, Y. (1975). Flow over rectangular cylinders immersed in a turbulent boundary layer (part 1, Correlation between Pressure Drag and Boundary-Layer Characteristics). *BullJSME*. 18, 1260-1268.
- Castro, I. P. & Robins, A. G. (1977). The flow around a surface-mounted cube in uniform and turbulent streams. *Journal of fluid Mechanics*, 79(2), 307-335.
- Frederich, O., Wassen, E. & Thiele, F. (2008). Prediction of the flow around a short wall-mounted finite cylinder using LES and DES1. *JNAIAM*, 3(3-4), 231-247.
- Haupt, S. E., Zajackowski, F. J. & Peltier, L. J. (2011). Detached eddy simulation of atmospheric flow about a surface mounted cube at high Reynolds number. *Journal of fluids engineering*, 133(3).
- Hoxey, R. P., Richards, P. J. & Short, J. L. (2002). A 6 m cube in an atmospheric boundary layer flow-Part 1. Full-scale and wind-tunnel results. *Wind and structures*, 5(2_3_4), 165-176.
- Hwang, R. R., Chow, Y. C. & Chiang, T. P. (1999). Numerical Predictions of Turbulent Flow over a Surface-Mounted Ribs. *Journal of Engineering Mechanics* 125(5), 497-503.
- Hunt, J. C., Wray, A. A. & Moin, P. (1988). Eddies, streams, and convergence zones in turbulent flows.
- Lehnasch, G., Jouanguy, J., Laval, J. P. & Delville, J. (2011). POD Based Reduced-Order Model for Prescribing Turbulent Near Wall Unsteady Boundary Condition. In *Progress in Wall Turbulence: Understanding and Modeling* (pp. 301-308). Springer, Dordrecht.
- Leite, H. F., Avelar, A. C., Abreu, L. D., Schuch, D. & Cavalieri, A. (2018). Proper Orthogonal Decomposition and Spectral Analysis of a Wall-Mounted Square Cylinder Wake. *Journal of Aerospace Technology and Management*, 10.
- Liu, Y. Z., Ke, F. & Sung, H. J. (2008). Unsteady separated and reattaching turbulent flow over a two-dimensional square rib. *Journal of Fluids and Structures*, 24(3), 366-381.

Lumley, J. L. (1967). The structure of inhomogeneous turbulent flows. *Atmospheric turbulence and radio wave propagation*.

Martinuzzi, R. & Tropea, C. (1993). The flow around surface-mounted, prismatic obstacles placed in a fully developed channel flow (data bank contribution).

Meyer, K. E., Pedersen, J. M. & Özcan, O. (2007). A turbulent jet in crossflow analysed with proper orthogonal decomposition. *Journal of Fluid Mechanics*, 583, 199-227.

Muld, T. W., Efraimsson, G. & Henningson, D. S. (2012a). Mode decomposition on surface-mounted cube. *Flow, turbulence and combustion*, 88(3), 279-310.

Muld, T. W., Efraimsson, G. & Henningson, D. S. (2012b). Flow structures around a high-speed train extracted using proper orthogonal decomposition and dynamic mode decomposition. *Computers & Fluids*, 57, 87-97.

Ong, M. C., Utnes, T., Holmedal, L. E., Myrhaug, D. & Pettersen, B. (2010). Numerical simulation of flow around a circular cylinder close to a flat seabed at high Reynolds numbers using a $k-\epsilon$ model. *Coastal Engineering*, 57(10), 931-947.

Orellano, A. & Wengle, H. (2000). Numerical simulation (DNS and LES) of manipulated turbulent boundary layer flow over a surface-mounted fence. *European Journal of Mechanics-B/Fluids*, 19(5), 765-788.

Podvin, B. (2009). A proper-orthogonal-decomposition-based model for the wall layer of a turbulent channel flow. *Physics of Fluids*, 21(1), 015111.

Prsic, M. A., Ong, M. C., Pettersen, B. & Myrhaug, D. (2019). Large Eddy simulations of flow around tandem circular cylinders in the vicinity of a plane wall. *Journal of Marine Science and Technology*, 24(2), 338-358.

Schmidt, S. & Thiele, F. (2002). Comparison of numerical methods applied to the flow over wall-mounted cubes. *International journal of heat and fluid flow*, 23(3), 330-339.

Sirovich, L. (1987). Turbulence and the dynamics of coherent structures. I. Coherent structures. *Quarterly of applied mathematics*, 45(3), 561-571.

Spalart, P. R., Deck, S., Shur, M. L., Squires, K. D., Strelets, M. K. & Travin, A. (2006). A new version of detached-eddy simulation, resistant to ambiguous grid densities. *Theoretical and computational fluid dynamics*, 20(3), 181.

Taira, K., Brunton, S. L., Dawson, S. T., Rowley, C. W., Colonius, T., McKeon, B. J., ... & Ukeiley, L. S. (2017). Modal analysis of fluid flows: An overview. *Aiaa Journal*, 4013-4041.

Tauqeer, M. A., Li, Z. & Ong, M. C. (2017). Numerical simulation of flow around different wall-mounted structures. *Ships and Offshore Structures*, 12(8), 1109-1116.

Tian, X., Ong, M. C., Yang, J. & Myrhaug, D. (2014). Large-eddy simulation of the flow normal to a flat plate including corner effects at a high Reynolds number. *Journal of Fluids and Structures*, 49, 149-169.

Utnes, T. & Ren, G. (1995). Numerical prediction of turbulent flow around a three-dimensional surface-mounted obstacle. *Applied mathematical modelling*, 19(1), 7-12.

Wu, W., Meneveau, C. & Mittal, R. (2020). Spatio-temporal dynamics of turbulent separation bubbles. *Journal of Fluid Mechanics*, 883.

Yang, J., Liu, M., Wu, G., Gu, H. & Yao, M. (2017). On the unsteady wake dynamics behind a circular disk using fully 3D proper orthogonal decomposition. *Fluid Dynamics Research*, 49(1), 015510.

Chapter 6

6. Concluding Remarks

6.1 Conclusions

In the present thesis, flows over different bottom-mounted structures are investigated using different numerical simulations. In the first study, which is presented in Chapter 4, 2D steady RANS with $k - \omega$ SST turbulence model is used to simulate the flow over a single and two tandem cylinders with different configurations. In all simulations, a good grid convergence has been achieved using a mesh number of less than 75000 cells and the validation study has shown that the results are in agreement with the previous published studies. For the cases with a single cylinder and different B/D s, the values of C_D , C_L and L_w decrease with the increasing B/D . When another cylinder with the same diameter is added downstream the original single cylinder, there are significant differences in the results. The absolute values of the hydrodynamic quantities for both cylinders tend to decrease with the increase of L/D until minimum absolute values are reached with a critical L/D . When L/D is larger than the critical value, the values of C_D and C_L for the two cylinders tend to develop to those of the single cylinder cases. The critical value of L/D reduces with the decreasing B/D and it is found to be very close to the value of L_w for the single cylinder case. Such results are useful for the on-bottom stability design of subsea tandem structures.

In the second study, which is presented in Chapter 5, 3D SADES is employed to investigate the flows over square, triangular and rectangular wall-mounted ribs. The convergence studies shown that a grid size of around two million cells achieves good convergence between cases. Also, validation of the results for the square rib is achieved against previous published experimental data. Hydrodynamic coefficients, such as C_D and C_L , time- and spanwise averaged streamlines, and instantaneous 3D flow structures are shown for each rib. Due to its streamlined geometry, C_D and C_L of the trapezoidal rib are lower compared with those of the square and rectangular ribs. Moreover, the flow in the wake region was analysed using the POD technique. A clear 3D behaviour of the flow is also observed by the streamwise and spanwise planes in which POD is applied. Strong turbulent fluctuations are found to be located around the shear layer of the flow. The POD modes in the XY-planes show wave-packet structures that convected downstream and the POD modes in the ZY-planes mainly show streamwise vortical structures.

6.2 Recommendations for Future Work

Based on the investigations presented in this thesis, it is possible to address a few future research studies that would have great contribution to the topic. They are summarized as follows:

- Investigation of the flow over two tandem bottom-mounted cylinders with different diameters at Reynolds number of 1.31×10^4 subjected to boundary layer flow with different thicknesses.
- Investigation of the flow over two tandem bottom-mounted cylinders at different Reynolds numbers, e.g. Reynolds number of $O(10^6)$.
- 3D SADDLES study of the flow over single and two tandem bottom-mounted ribs with geometries different from the ones investigated in Chapter 5, such as triangular ribs or trapezoidal ribs with different incline angles of the slopes, at high Reynolds number of $O(10^6)$ and POD analysis of the flow structures in the wake region.
- 3D LES study of the flow over two bottom-mounted cylinders with different spacing between them at high Reynolds number of $O(10^6)$ and POD analysis of the flow structures in the wake region.